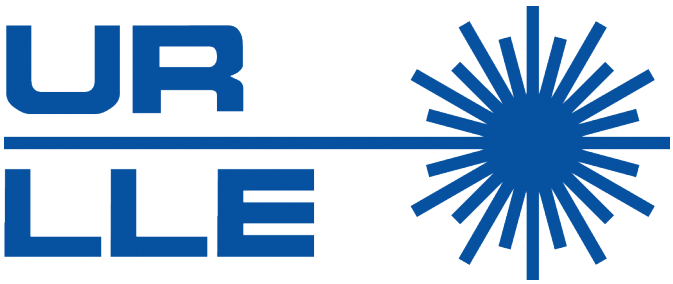

2021 SUMMER RESEARCH PROGRAM FOR HIGH SCHOOL JUNIORS

AT THE

UNIVERSITY OF ROCHESTER'S

LABORATORY FOR LASER ENERGETICS

STUDENT RESEARCH REPORTS

PROGRAM DIRECTOR

Dr. R. Stephen Craxton

January 2024 **Lab Report 499**

Laboratory for Laser Energetics
University of Rochester

2021 SUMMER RESEARCH PROGRAM FOR HIGH SCHOOL JUNIORS

AT THE

UNIVERSITY OF ROCHESTER'S

LABORATORY FOR LASER ENERGETICS

STUDENT RESEARCH REPORTS

PROGRAM DIRECTOR

Dr. R. Stephen Craxton

LABORATORY FOR LASER ENERGETICS

University of Rochester

250 East River Road

Rochester NY 14623-1299

During the summer of 2021, eight students from Rochester-area high schools participated in the Laboratory for Laser Energetics' Summer High School Research Program. This was the 32nd year of the program, which started in 1989. The 2020 program was unfortunately canceled because of the COVID-19 pandemic. In 2021, LLE held a fully virtual program for students who had applied and been interviewed for the 2020 program. The program started earlier than usual (in the middle of June rather than after July 4) and finished earlier (in the middle of August) to meet the schedules of the graduating seniors. The program comprised nine weeks rather than the usual eight.

The goal of LLE's program is to excite a group of high school students about careers in the areas of science and technology by exposing them to research in a state-of-the-art environment. Too often, students are exposed to "research" only through classroom laboratories, which have prescribed procedures and predictable results. In LLE's summer program, the students experience many of the trials, tribulations, and rewards of scientific research. By participating in research in a real environment, the students often become more excited about careers in science and technology. In addition, LLE gains from the contributions of the many highly talented students who are attracted to the program.

The students spent most of their time working on their individual research projects with members of LLE's scientific staff. The projects were related to current research activities at LLE and covered a broad range of areas of interest including experimental diagnostic development, computer modeling of implosion physics, experimental design, plasma-physics simulations, physical chemistry, future laser system design, and scientific data management. The students, their high schools, their LLE supervisors, and their project titles are listed in Table I. Their written reports are collected in this volume. By working through several iterations of their project reports, incorporating feedback from their supervisors and the Program Director, the students experience most of the steps involved in preparing a scientific paper for publication.

The students attended weekly seminars on technical topics associated with LLE's research. Topics this year included laser physics, fusion, nonlinear optics, nuclear physics, pulsed power, fiber optics, and LLE's cryogenic target program. The students also learned how to give scientific presentations, were given guidance on writing scientific reports, and were introduced to LLE's computational resources.

The program culminated on 11 August with the virtual "High School Student Summer Research Symposium," at which the students presented the results of their research to an audience including parents, teachers, and LLE staff. Each student spoke for approximately 15 minutes including two minutes for questions.

A total of 399 high school students have participated in the program from its inception through 2021. The students in 2021 were selected from nearly 70 applicants to the canceled 2020 program. Each applicant submitted an essay describing his or her interests in science and technology, a copy of his or her transcript, and a letter of recommendation from a science or math teacher.

LLE plans to continue this program in future years. The program is strictly for students from Rochester-area high schools who have just completed their junior year. Application information is mailed to schools and placed on the LLE web site in January with an application deadline near the middle of March. For more information about the program, please contact Dr. R. Stephen Craxton at LLE.

Acknowledgment

This material is based upon work supported by the Department of Energy National Nuclear Security Administration under Award Number DE-NA0003856, the University of Rochester, and the New York State Energy Research and Development Authority.

otherwise does not necessarily constitute or imply its endorsement, recommendation, or favoring by the U.S. Government or any agency thereof. The views and opinions of authors expressed herein do not necessarily state or reflect those of the U.S. Government or any agency thereof.

Table I: High School Students and Projects—Virtual Program, Summer 2021.

Name	High School	Supervisor	Project Title
Semma Alfatlawi	Victor	C. J. Forrest	Inferring a Neutron Yield from Nuclear Activation Techniques
Felix Huang	Webster Schroeder	H. G. Rinderknecht	Uniformity of X-Ray Prepulses for Imprint Mitigation in Directly Driven Implosions
Audrey Kohlman	Churchville-Chili	R. S. Craxton	Polar-Direct-Drive Designs for the Laser Megajoule
Meghan Marangola	Brighton	R. S. Craxton	Optimization of Direct-Drive Designs for a Proposed Dual Direct-/Indirect-Drive Laser
Tyler Petrillo	Webster Schroeder	R. S. Craxton	Development of a Polar-Direct-Drive Design for Large-Diameter Beryllium and Plastic Targets on the National Ignition Facility
Leo Sciortino	School of the Arts	R. W. Kidder	Data Services to Improve Access to Scientific Image Data
Aditya Srinivasan	Pittsford Sutherland	A. B. Sefkow and M. Lavell	Exploration of Conduction and Stopping-Power Models for Hybrid Fluid-Kinetic Simulations
Andrew Wu	Pittsford Mendon	K. L. Marshall	Computational Modeling of the Polarizability of Liquid Crystals

Inferring a Neutron Yield from Nuclear Activation Techniques

S. Alfatlawi

Victor Senior High School

Advisor: C.J. Forrest

Laboratory for Laser Energetics, University of Rochester, 250 East River Road Rochester, New York 14623-1299, USA

May 2023

I. Abstract

Nuclear measurements are essential for studying inertial-confinement-fusion experiments when plasmas reach the conditions necessary for generating fusion reactions. One approach to inferring a nuclear yield is to measure the time integrated yield from the neutron-producing deuterium-deuterium (DD) fusion reaction with neutron-induced activation of indium isotopes. In this method, a neutron yield can be calculated based on the gamma ray spectrum that results from the deexcitation of indium-115. 336 keV gamma rays, from the reaction channel ^{115}In (n,n')^{115}In, were counted using a high-purity germanium (HPGe) detector. A second DD fusion reaction with an equal branching ratio produces a proton yield, which was used to determine a cross-calibration factor (*f*) for the HPGe detector. The proton yield measurements were generated from a joint campaign between LLE and MIT on March 3rd, 2020. The gamma ray counts were post-processed in MATLAB along with proton yields to generate an *f* value. This value was used to generate net indium yield values as the emitted gamma ray count is proportional to the nuclear yield. These yields were then verified in the Omega Nuclear database. A distinct lower limit was set on the nuclear yield for each neutron time-of-flight detector to ensure accurate calculations and detector measurement uncertainty was determined to be less than one percent for the HPGe diagnostic.

II. Introduction

Fusion reactions create the most fundamental form of energy of the universe. Thermonuclear fusion occurs when nuclei from atoms with low atomic weight, such as hydrogen, bond to form a nucleus that has a higher atomic weight, such as helium. This process leads to the release of energy in the form of high-energy particles that are emitted when the total mass before the reaction exceeds the resulting mass of the system ($E = Mc^2$). Every star,

including our sun, utilizes the process of thermonuclear fusion to form energy. Stars and the Sun can naturally generate fusion reactions due to their significantly large masses, which allow them to gravitationally compress the gas in their cores. As this compression occurs, their cores reach extremely high temperatures (the temperature of the center of the sun is 14 million degrees Celsius) and densities, which causes nuclear fusion to ensue.[1]

The OMEGA laser at the Laboratory for Laser Energetics (LLE) is used to compress the fuel within a target so that it achieves very intense temperatures and densities creating the foundation for research in high energy conditions, similar to those that occur in the sun. The fusion reactions are triggered by temperatures reaching several tens of millions of degrees Celsius, which are significantly greater than those reached by the sun.

Scientists believe that fusion energy will be that of the future due to its vast amount of positive factors. Nuclear fusion is a practically inexhaustible source of energy, it is operated in a contained environment, and it does not release radioactive material into the atmosphere. Additionally, fusion does not contribute to greenhouse gas emissions due to its ability to function without a gas or oil source.[1]

There are two approaches to setting up a fusion reaction: magnetic confinement fusion (MCF) and inertial confinement fusion (ICF). Nuclear fusion utilizes a plasma, which is produced when hydrogen gas is heated to extremely high temperatures and the positively charged nuclei are separated from the negatively charged electrons. Electric charges have the ability to interact with magnetic fields, allowing them to guide the direction of the plasma. The magnetic fields in MCF prevent the plasma from contacting the walls of the reactor, which would dissipate a fraction of the system's energy. The most effective MCF model takes on a toroidal shape. The system's helical magnetic field lines control and confine the plasma.[2]

The OMEGA laser conducts direct drive fusion reactions as shown in figure 1. A target is

accelerated by utilizing incident laser beams that directly irradiate the target. Newton's third law states that every action has an equal and opposite reaction. Therefore, a rocket effect occurs as the laser beams heat then ablate the outside of the target, which causes the target's plastic shell to blast outward, generating an outer layer of plasma. This forces the inner portion of the target to implode. The example shown in figure 1 illustrates a target containing deuterium and tritium fuel that is imploded. The outer portion of the target is ablated, creating a central hotspot in the fuel core and plasma. This differs from indirect drive implosions, which irradiate a target through x-rays generated by incident laser beams that irradiate the inside of a symmetric cylindrical case (known as a hohlraum) containing the target. Both produce an environment created by the outer plasma which heats the fuel to densities and temperatures that allow for thermonuclear fusion reactions to occur. If enough of the alpha particle energy produced by the fusion reaction is deposited in the fuel to heat more fuel to fusion temperatures, thermonuclear burning takes place.

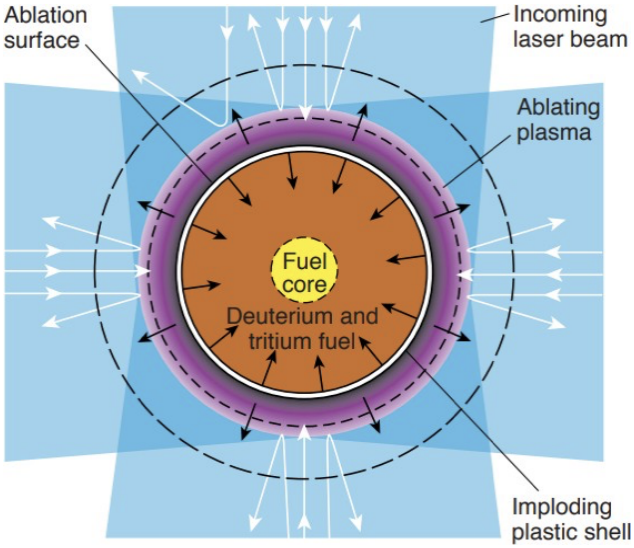

Figure 1: *Demonstration of the direct drive fusion process. Ablating material accelerates the fuel, and the resulting force compresses the reaction inwards. This process creates the temperatures and densities necessary for fusion reactions to take place.*[1]

Once thermonuclear burning ensues, the plasma core will continue to burn and produce energy until the core's pressure and temperature are not able to sustain further fusion. Newton's First Law of Motion states that an object will remain either at a constant velocity or at rest until acted upon by an external force. This is how the inertia of the fuel causes it to remain compressed in the core of the target. This fuel burns and produces energy until the system reaches a pressure high enough to degrade the implosion, causing the shell to rapidly expand. Fusion reactions appear instantaneous, as the compressed state in which they occur lasts for less than one billionth of a second, which is the only time that useful energy is generated during the reaction.[1]

Isotopes of hydrogen, deuterium and tritium, are universally used to conduct fusion reactions due to their high cross sections. A list of known cross sections for such reactions are listed in table 1 (taken from Ref. 3).

Table 1: *Deuterium-Tritium Reaction Channels*

Reaction			σ_{max} (barn)	E_{max} (keV)
D + T	→	^{4}He (3.5 MeV) + n (14.1 MeV)	5.0	64
D + D	→	T (1.01 MeV) + p (3.03 MeV)	0.096	1250
	→	^{3}He (0.82 MeV) + n (2.45 MeV)	0.11	1750
D + ^{3}He	→	^{4}He (3.6 MeV) + p (14.7 MeV)	0.9	250
T + T	→	^{4}He (0-3.5 MeV) + 2n (0 - 9.4 MeV)	0.16	1000
	→	^{5}He (1.7 MeV) + n (8.7 MeV)		
	→	^{5}He* (∼4.4 MeV) + n (∼6.0 MeV)		
^{3}He + ^{3}He	→	^{4}He + 2p (12.9 MeV)	0.12	8500
T + ^{3}He	→	^{4}He + n + p (12.9 MeV)	0.06	1075
	→	^{4}He (4.8 MeV) + D (9.5 MeV)		

∗ implies excited state.

σ_{max} is the maximum cross-section σ for a reaction where σ represents the area around one interacting particle that the other reacting particle must hit in units of barn (10^{-24} cm^2), which is

correlated to the probability that the reaction will occur. E_{max} is the maximum energy in units of kiloelectron-volts in the center of mass frame at which the cross section σ is maximum (with a value of σ_{max}). As demonstrated by the large cross-section, DT reactions have the highest cross section and occur more frequently than DD fusion reactions. The specific DD cross section that will be further explored in this project results in the formation of a helium-3 atom and the emission of a neutron.

The goal of this research was to calibrate a DD-n Indium-115 yield detector. In order to measure the number of neutrons emitted in the DD reaction, a neutron activation approach was taken. Indium activation is the process of activating a sample of Indium-115 through its interaction with high-energy neutrons generated from a fusion reaction, producing an unstable nuclear state.[3] The decay reaction of the activated indium sample produces gamma rays that can be counted by detectors to determine the neutron yield. This is important because inferring primary yields using the activation approach is an effective method for cross-calibrating other detectors for accurate yield measurements.

Neutron yields are calculated by first using the gross counts measured from gamma ray spectra. Net counts are then found by subtracting the background from the gross counts. This was made possible on March 3rd, 2020, when LLE and MIT ran a joint campaign to produce a calibrated Indium-115 detector for DD neutrons. This paper focuses on the outcomes of this collaboration.

III. Experimental

Indium-115 was chosen to measure DD neutrons due to its well known half life decay and emission of 336 keV gamma rays. As shown in figure 2, Indium-115 has a half-life of 4.49 hours (269 minutes). This half life is advantageous because it allows for indium samples to be

transported from the chamber to a high purity germanium (HPGe) detector where 336 keV gamma rays are counted.[4] In comparison, other elements, such as Copper-63 with a half-life of 9.74 minutes, decay much faster and cause accurate yield measurements to become harder to achieve.

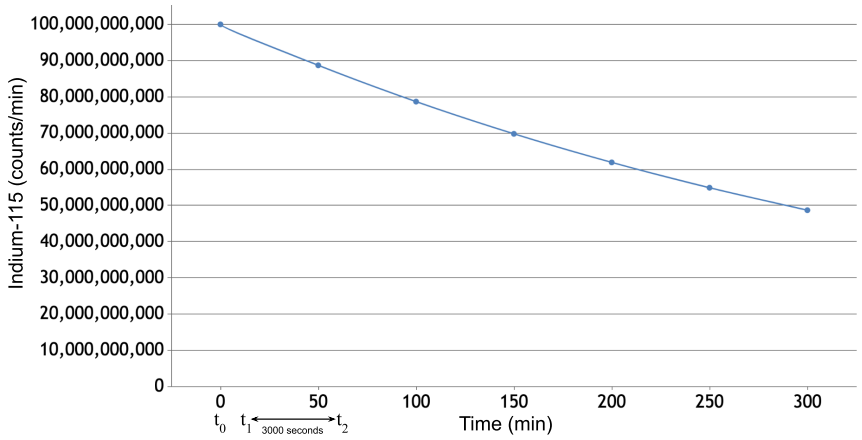

Figure 2: *Indium-115 decay curve that demonstrates gamma ray counts as a function of time and illustrates the sample's half life. t_0, t_1, and t_2 are labeled on the x-axis to show the time taken to transfer the indium sample to the counting chamber (t_1) and the counting time (t_2).*

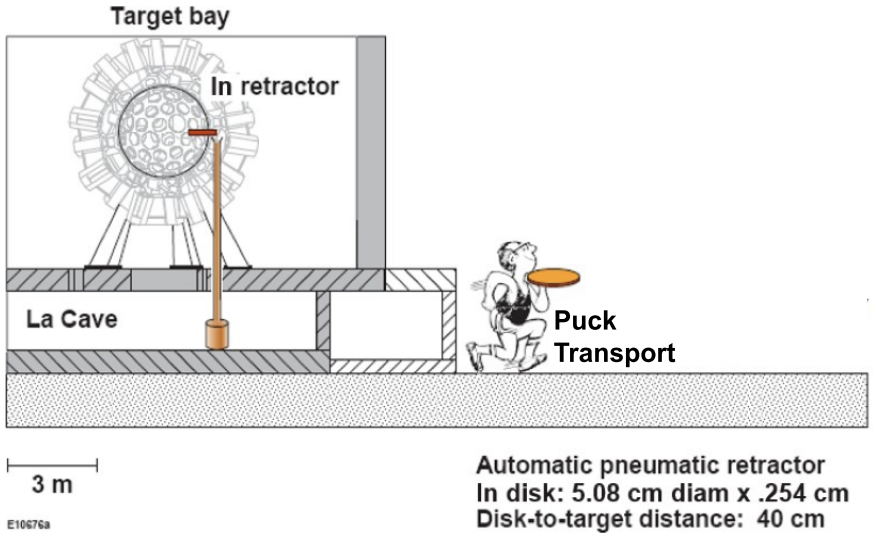

Figure 3: *A visualization of the transportation process for indium activation that illustrates the target chamber. It is required for a person to physically move the indium puck from the chamber to the counting facility, where an HPGe detector can count the gamma rays emitted from the indium.*[5]

The In-activation system depicted in figure 3 contains a target that is irradiated by laser beams positioned symmetrically around it. The target is a plastic shell filled with deuterium and tritium at cryogenic temperatures. In this experiment, an indium sample and germanium detector were selected to measure the neutron yield through gamma ray counts. The Indium-115 sample, which was a 0.254 cm thick by 2.54 cm radius cylinder puck, was placed at a mean distance of 40 cm from the neutron source. An indium retractor was used to remove the activated indium puck from the target bay after the fusion reaction occurred. The indium samples were then transferred to a counting facility where counting occurred using HPGe detectors for 3000 seconds. The intensity of the 336 keV gamma ray decay could be concluded from the counts achieved.

By using known distances between the target chamber center and detector, neutron time-of-flight (nTOF) detectors were also used to measure the energy spectrum of neutrons emitted from the target. nTOF detectors at distances of 12 meters, 5.4 meters, and 3 meters were used in order to measure neutron yields from the reaction. Each detector has different ranges of sensitivity that produce valid yield measurements until saturation is reached. This results in an inability to accurately measure the contribution to the yield from low-energy neutrons (those below the lower bound set on the nTOF detectors), which hinders the detector's ability to formulate absolute yields for all D-D and D-T reactions. As shown in table 2, the 3 meter detector has the lowest saturation point at about 1E+10 neutrons onto the detector, so it is not viable for indium activation shots. The 5 meter and 12 meter detectors are more accurate nTOF detectors for indium activation due to their higher saturation points of 3.616E+10 and 3.215E+10, respectively.

Table 2: *Saturation points of nTOF detectors for measuring DD neutrons*

nTOF Detector	**Saturation Point**
3m nTOF	Saturated at 1E+10; below a majority of indium activation shot yields
5m nTOF	3.616E+10
12m nTOF	3.215E+10

There are several challenges to overcome when conducting these ICF experiments that had to be considered when calculating the yield from the measurements. These challenges may reduce neutron yields and lead to inaccurate calculations when yields are, in reality, higher than what is measured. Significant challenges include non-uniformity in the fuel target and variations in the laser beam energy deposition on the target. Non-uniform laser beams that are incident on the target create Rayleigh-Taylor instabilities. As the implosion progresses, this instability grows due to a surrounding lower density plasma pushing against the higher density fuel. When the imploding fuel shell decelerates as it approaches the target center, the deceleration Rayleigh-Taylor instability occurs. This causes perturbations–as shown in figure 4–that reduce the resulting target's neutron yield.[6]

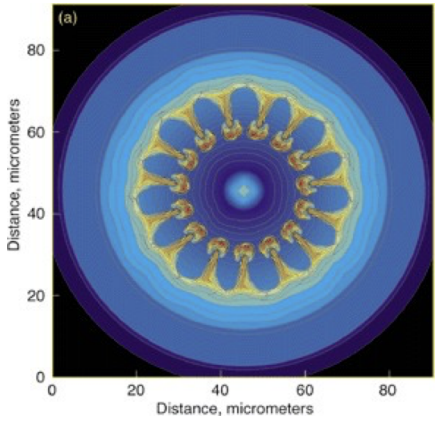

Figure 4: *Visual representation of the density contours and vorticity that arise from penetration of inner fuels as the outer shell pushes lighter fluid.[6] This creates deceleration instabilities that can reduce the efficiency of nuclear measurements.*

Oftentimes, predictions of experimental results overestimate an ICF system's performance by neglecting how non-uniformities in the target degrade the yield. Roughness of the inner surface also leads to target perturbations. LLE has achieved a greater laser uniformity through the use of smoothing by spectral dispersion.[7] Measuring the neutrons from fusion reactions will aid in understanding these instabilities and how to mitigate them.

IV. Data Analysis

This MIT and LLE joint campaign generated data from 12 shots that were used to produce a calibrated Indium-115 detector for DD neutrons by comparing DD-p and DD-n detectors, which measure proton and neutron yields, respectively, for each shot, and calculating an average calibration value. The neutron and proton branching ratio for DD fusion reactions are equal, so equivalent yield values generated by MIT's DD-p detector and LLE's DD-n detector are expected.

A consistency check was performed to verify how Gamma Vision,[8] an application used for HPGe spectrum analysis, calculated the net counts and uncertainty of gamma rays for each shot. The Gamma Vision formulas listed below were processed in MATLAB and net counts as well as error bars were calculated for all the indium activated nuclear fusion shots taken at the lab. Figure 5 displays a visual of the variables calculated and used in the formulas.

The first formula used was $B = \left(\sum_{i=l}^{l+(n-1)} Ci + \sum_{i=h-(n-1)}^{h} Ci \right) \frac{h-l+1}{2n}$ which calculates the background by calculating the average counts of the channels surrounding the region of interest (ROI) where l is the low limit channel, h is the high limit channel, and Ci is the counts of channel

i. The second formula used was $An = \sum_{i=l+n}^{h-n} Ci - B$ which calculates the net counts of the peak An by subtracting the calculated background from the adjusted gross area where the adjusted gross area, Aag, is the sum of all the channels in the ROI that are not used in the background from l+n to h-n. The third formula used was $\sigma_{An} = \sqrt{Aag + B(\frac{h-l-(2n-1)}{2n})(\frac{h-l-(2n-1)}{h-l+1})}$ which calculates the uncertainty in the net counts of the peak.[8]

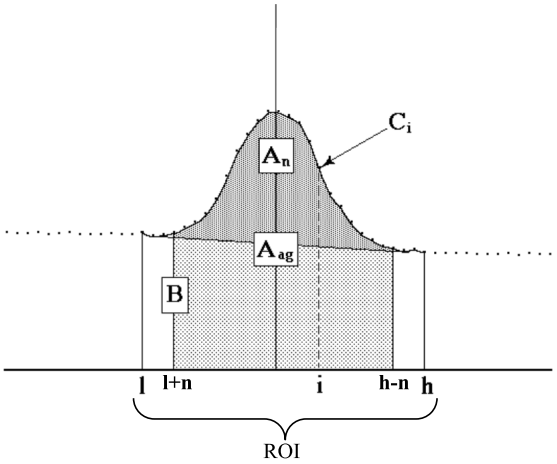

Figure 5: *Net counts were calculated by subtracting the background from gross counts. The diagram shows the specific components used to calculate and separate the background from the net counts. n is the number of background points selected to calculate the background. n−1 points on each side of the peak form the endpoints of the straight-line background. The x axis represents the energy spectrum and the y axis represents gamma ray counts* [8]

Figure 6 shows plots of the 12 meter neutron time-of-flight detector's (12 nTOF) yield and MIT's DD-p yield against the yield from a photomultiplier tube detector (PMTD), which is an excellent device for determining DD implosion yields due to its high precision and accurate ion-temperature measurements.[9] This plot demonstrates that the PMTD and nTOF detectors strongly agree, validating their respective yields, which illuminates two clear outlying points. A

linear relationship was visible between the PMTD and the 12 meter nTOF detector, and the two outlying points were clear when plotted against the PMTD (circled in red in figure 6), further providing evidence for an inaccurate DD-p MIT yield measurement from two of the shots.

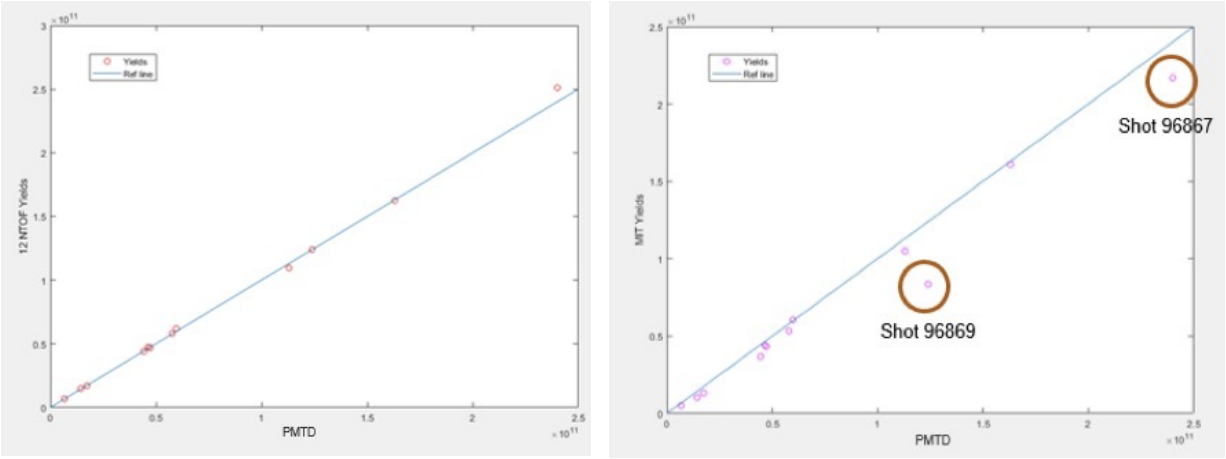

(a) PMTD yields vs. 12m nTOF yields (b) PMTD yields vs. MIT yields

Figure 6: *The PMTD yields plotted against (a) the 12 nTOF yields and (b) the MIT DD-p yields. The blue lines are y = x, which demonstrates the agreement between the yields plotted on the axes as they fall very close to the blue lines. Thus, these plots clearly show the two outlying MIT yields as they deviate from linearity.*

After removing the two outlying points, the cross calibration factor (*f*) used to accurately measure DD fusion neutrons was calculated using the formula shown below

$$f = \frac{{l'_s}^2 (An)}{N {l_s}^2 (e^{-\lambda t_1} - e^{-\lambda t_2}) M_{in}}$$

where l_s is the mean distance from the neutron source to the indium sample (l'_s refers to the

parameters from pulsed neutron yields), An represents the net counts of the peak, N is the neutron yield, λ is the inverse mean lifetime of Indium-115, t_1 is the delay time between neutron irradiation and counting, t_2 is the counting time, and M_{in} is the mass of the Indium-115 sample.[10] The 10 remaining MIT dd-p yields, discarding the two outliers, were used as N and a corresponding f value was calculated for each shot. These values were then averaged together to generate an average f value of $3.78\text{x}10^{-8}$. The average f value was used in the formula in place of f, and the formula was rearranged to calculate a cross calibrated neutron yield value for the 140 DD-n LLE shots.

To further verify a higher accuracy after the two outlying points were removed, the DD-n yield value for each shot was generated using a calibration factor calculated from all 12 DD-p MIT shots and then with the two outlying points removed. The two sets of neutron yields calculated using the differing calibration factors were then plotted against the 12 nTOF detector. With all shots used for calibration, a 0.739% standard error was observed. After the outlying points were removed, a slightly lower standard error of 0.736% was observed, which supports the removal of the inaccurate shots in the cross calibration calculation.

This calibration factor *f* was then used to cross calibrate indium detector gamma ray spectra. The background was removed from the gamma ray counts and the net counts from 140 nuclear shots were calculated and plotted in figure 7. The formulas used in this process were coded in Matlab to create a neutron yield calculator.

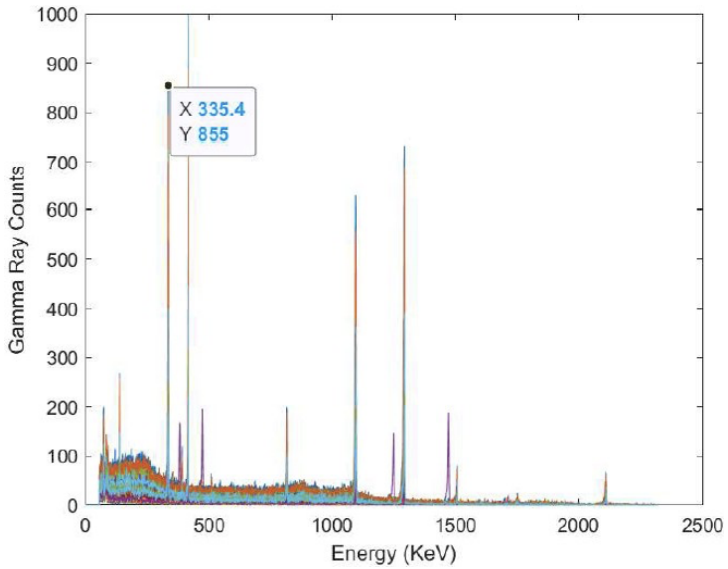

Figure 7: *Gamma ray counts generated from 140 overlaid nuclear shots taken with the OMEGA laser. The peak studied in this experiment was the 336 keV peak. The gamma rays generated from each shot were calibrated using a MATLAB neutron yield calculator to calculate nuclear yields that were verified in the Omega Nuclear database. This graph demonstrates other count peaks that were not further investigated but have potential to be studied in the future.*

VI. SUMMARY AND SUGGESTIONS FOR FUTURE WORK

A DD-n Indium-115 Yield detector was calibrated during a joint campaign between LLE and the MIT Plasma Science and Fusion Center. 140 nuclear shots were run through a MATLAB calculator to produce neutron yield measurements that were added to the Omega Nuclear Database. Two suspect DD-p MIT points were removed from calculations of the calibration factor *f*. By removing the two outlying points, the standard error between the DD-n yields plotted

against the 12 meter nTOF yields decreased, verifying a more accurate calibration factor without the two MIT points. A lower bound was set for each nTOF detector to guarantee accurate nuclear yield measurements by examining deviations in linearity against the current indium yields in the Omega Nuclear Database.

As seen in figure 7, there are other reaction channel peaks that could be further researched such as the 417 or 1097 keV peaks. Data gathered from these reaction channels could further confirm the current DD-n indium yield values. Additionally, it is currently assumed that the D-D reaction leads to two product branches that are evenly split, where 50% of the time, protons are released and the other 50%, neutrons are released. By using the DD-p MIT yields and the DD-n LLE yields, this theory could either be confirmed or contradicted.

One may also consider the effects of altering the experimental setup, for example, the size of the puck that is irradiated by the laser. The puck size in this experiment was chosen due to readily available 0.254 cm thick by 2.54 cm radius cylindrical pucks. However, there is potential for experimentation with larger pucks. A larger puck would allow for lower yields and higher counts to be measured. With the puck size used in this experiment, yield measurements were limited by a lower bound of approximately 3E+10. Conversely, the puck size must not exceed the detector's ability to count every gamma ray emitted by the sample, setting an upper bound for the maximum size of the sample. By creating a MATLAB code to calculate the optimal size for the puck that does not exceed the upper limit, future work can produce more accurate yields as the lower bound would decrease, capturing gamma ray counts that may be missed with the current indium sample size.

VII. Acknowledgements

I would like to thank my advisor, Dr. Chad Forrest, for his continuous guidance, patience, and mentorship throughout the program. The time and effort he spent in aiding my understanding of the foundations of nuclear fusion are greatly appreciated. I would also like to thank Dr. Craxton for running the summer research program and Kim Truebger for ensuring the program ran smoothly. This unique project has offered me valuable experiences and has inspired my future endeavors in research. Lastly, I would like to thank the seven other interns and the LLE community for providing me with companions and constructive feedback when needed.

VIII. Sources

1. L. H. Gresh, R. L. McCrory, and J. M. Soures, “ Inertial Confinement Fusion: An Introduction”, https://www.lle.rochester.edu/index.php/2008/09/12/inertial-confinement-fusion-an-introduction/ (2008)
2. “Nuclear Fusion Power”, World Nuclear Association, https://www.world-nuclear.org/information-library/current-and-future-generation/nuclear fusion-power.aspx (updated 2021)
3. C. J. Forrest, “Measurements of the fuel distribution in cryogenic D-T direct-drive implosions”, UR Research (2015), http://hdl.handle.net/1802/30236
4. W. Bang, H. J. Quevedo, G. Dyer, J. Rougk, I. Kim, M. McCormick, A. C. Bernstein, and T. Ditmire , "Calibration of the neutron detectors for the cluster fusion experiment on the

Texas Petawatt Laser", Review of Scientific Instruments 83, 063504 (2012), https://doi.org/10.1063/1.4729121

5. Frenje, J A (Feb 2020). Nuclear diagnostics for Inertial Confinement Fusion (ICF) plasmas. Plasma Physics and Controlled Fusion, 62(2), 44. doi:101088/1361-6587/ab5137
6. H. Sakagami and K. Nishihara, Physics of Fluids B2, 2715 (1990)
7. S. Skupsky, R. W. Short, T. Kessler, R. S. Craxton, S. Letzring, and J. M. Soures, "Improved laser—beam uniformity using the angular dispersion of frequency—modulated light", Journal of Applied Physics 66, 3456-3462 (1989) https://doi.org/10.1063/1.344101
8. “Gamma Vision V8 Users Manual.” UserManual.Wiki, Advanced Measurement Technology, Inc.,usermanual.wiki/Document/GammaVision20V820Users20Manual.1982380323/view. Accessed 17 July 2022.
9. V. Yu. Glebov, C. Stoeckl, C. J. Forrest, J. P. Knauer, O. M. Mannion, M. H. Romanofsky, T. C. Sangster, and S. P. Regan, "A novel photomultiplier tube neutron time-of-flight detector", Review of Scientific Instruments 92, 013509 (2021) https://doi.org/10.1063/5.0029005
10. General Electric Company (GEND), St. Petersburg, Florida 33733, "Absolute calibration of a total yield indium activation detector for DD and DT neutrons", Review of Scientific Instruments 63, 4889-4891 (1992) https://doi.org/10.1063/1.1143541

Polar Direct Drive Designs for the Laser Megajoule

Audrey Kohlman

Churchville-Chili Senior High School

Churchville, New York

Advisor: Dr. R. Stephen Craxton

Laboratory for Laser Energetics

University of Rochester

Rochester, New York

May 2023

1. Abstract

The Laser Megajoule (LMJ) is an under-construction French laser facility that is configured for indirect drive implosions. This configuration includes two rings of quads in each hemisphere; these rings are positioned at either 33.2° or 49.0° from the vertical axis. There are four beams in a quad and ten quads within each ring, giving a total of 160 beams. Following a proposal to perform direct drive implosions on the LMJ, simulations using the program *Sage* were run assuming a 1000 μm radius target; beams were repointed in the theta (longitudinal) and phi (latitudinal) directions and quads were defocused. When user experiments begin in 2024, only half of the beams will be available. Repointing in the phi direction was essential for compensating for the missing beams when simulating the initial experiments. These simulations achieved implosions with low velocity nonuniformities of approximately 2% rms. Simulations of the LMJ at full capacity resulted in even lower nonuniformities of below 1% rms. This demonstration of the feasibility of direct drive on the LMJ is expected to be applicable to a variety of experiments.

2. Introduction

Nuclear fusion is a reaction in which atomic nuclei merge together to create different, and typically heavier, nuclei. The energy released by this reaction could one day provide a clean source of energy to the world; therefore, different methods of attaining it have been explored. One such method is inertial confinement fusion (ICF), in which a target comprised of a solid exterior and gaseous interior is required to be the object of laser compression. This target is filled with fuel composed of deuterium-tritium (DT), which is typically a cryogenic layer of solid DT inside the exterior shell together with some DT gas in the interior. The target is compressed so intensely that it reaches temperatures and pressures comparable to those found in the center of stars. The DT fuses together when the target reaches peak compression. Furthermore, fusion takes place during the short period before the target disassembles [1].

There are two means of performing laser-driven ICF: direct drive and indirect drive. Direct drive [Fig. 1a] involves uniformly aiming beams from all directions at the center of the target. Indirect drive [Fig. 1b] involves placing a target within a cylindrical container made of a substance with a high atomic number; this container is known as a hohlraum. Beams are shot through openings on the ends of the hohlraum. After absorbing the beams, the hohlraum irradiates the target with x rays, allowing for a more uniform implosion of the target than what direct drive typically permits. However, direct drive provides a much higher absorption percentage into the target than indirect drive.

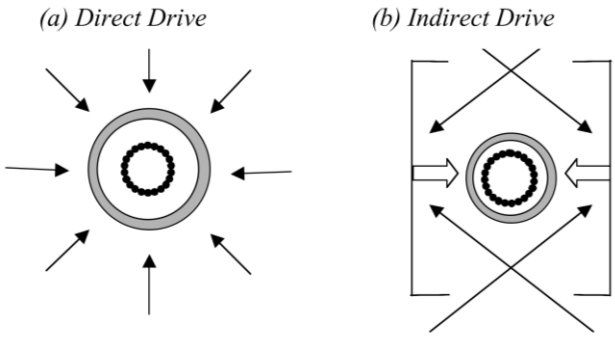

Figure 1. Two methods of laser fusion. (a) In direct drive, the laser beams (represented by arrows) encompass the target and directly strike it. (b) In indirect drive, the beams come in through opposite ends of a cylindrical container known as a hohlraum, striking its walls which irradiate the target with x-rays. (From Ref. 2)

Specifically, the U.S. National Ignition Facility (NIF), a 192 beam laser facility, is configured for indirect drive. The beam ports on the NIF are arranged into four rings in each of the upper and lower hemispheres of the target chamber [Fig. 2a]. Rings are composed of quads, which are groups of 4 beam ports. These rings are at 23.5°, 30.0°, 44.5°, and 50.0° from the vertical, respectively. The indirect drive configuration necessitates that these rings are at a large angle from the equator so they may enter the openings of the hohlraum. In contrast, the rings would be more evenly dispersed throughout a chamber configured for direct drive. Using an indirect drive beam configuration for a direct drive implosion would cause high levels of nonuniformity [Fig. 2b]. The poles of the target receive too much energy from the beams and flatten: almost like a pancake. However, this effect can be countered if some of the beams are repointed towards the equator of the target [Fig. 2c]. Previous designs prove the viability of direct drive designs on the NIF.

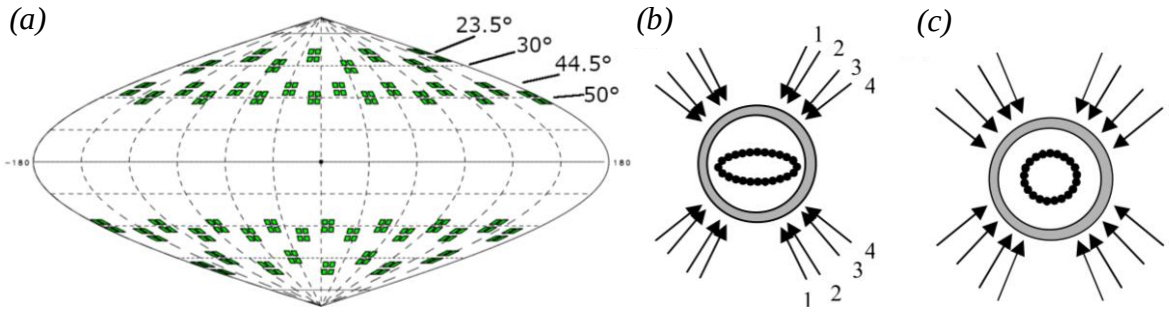

Figure 2. (a) The target chamber of the NIF with its indirect drive configuration. Each small green square represents a laser beam. (From Ref. 3) (b) The resulting implosion of the target with the indirect drive configuration of the NIF. The outer grey circle represents the target before beams are fired while the inner black circle represents the target after the beams have struck it. (c) The resulting implosion of the target when the NIF's beam configuration is adjusted for direct drive. The arrows representing the laser beams spread out towards the equator when these adjustments are made. This increases the amount of energy directed towards the equator and decreases the amount at the poles. The resulting implosion is uniform. (From Ref. 2)

Similarly, the Laser MegaJoule (LMJ) is another laser facility with an initially indirect drive beam configuration that has the potential to permit direct drive experiments. The LMJ has 160 beams that are arranged into two rings in each hemisphere [Fig. 3]; the rings are at angles of 33.2° (Upper Ring) and 49.0° (Lower Ring) from the vertical in the top hemisphere; these angles are reflected onto the bottom hemisphere. Like the NIF, the LMJ's rings are distanced far from the equator in order to facilitate indirect drive experimentation. However, the LMJ has four less rings than the NIF, making it more challenging to develop an apt beam configuration for direct drive. To further exacerbate the issue, only half of the beams will be available for experimentation in 2024. In order to implement direct drive, beams need to be repointed and defocused in a way that allows for the most uniform implosion. Each beam's aimpoint can be moved in the φ (longitude) and θ (latitude) directions [Fig. 3].

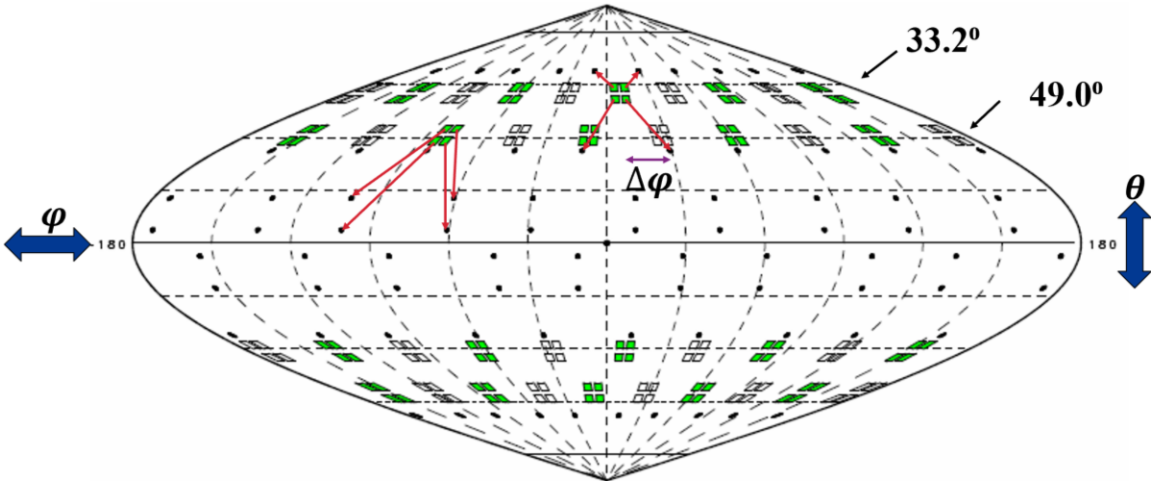

Figure 3. The target chamber for the LMJ in 2024, with beam pointings optimized for direct drive. The LMJ has 40 quads arranged into 4 rings. Green quads are active, while uncolored quads are not. The black dots indicate where the beams will strike the target, or aimpoints. The red arrows show which beam port connects to which aimpoint. The purple arrow represents the change in φ, the left end being the position of the quad center, and the right end being the aimpoint. [Run 1056]

Norreys et al. proposed an experiment to perform direct drive on the LMJ using a 1000 μm radius target, with a carbon-deuterium (CD) shell, followed by a layer of CD foam, which encapsulates the deuterium gas within the target [Fig. 4a] [4]. Notably, deuterium gas is being used in this experiment instead of DT gas, even though DT produces more fusion reactions. This is because tritium is radioactive, making it difficult to handle. Moreover, using deuterium gas allows the implosion dynamics to be studied. The laser pulse is displayed in Figure 4b, with a total energy of 244 kJ. In the present work, the laser pulse shape and the target parameters (75 μm of foam at 0.253 g/cm^3 followed by a shell thickness of 17.5 μm at 1.04 g/cm^3 with an outer radius of 997.5 μm) were taken from Ref. 5, with the minor difference that CH was modeled rather than CD.

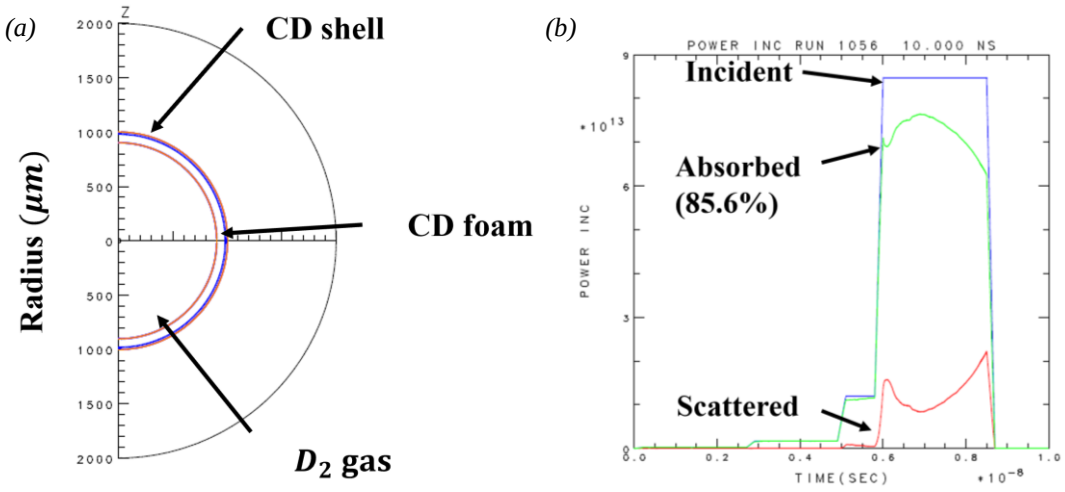

Figure 4. (a) Half of a cross-section of the proposed target. (b) A graph of the power (in W) against time of the optimized 2024 design. The blue line shows the actual power of the laser pulse. For the first two nanoseconds, the power is so low that it is barely visible. Then, there are two larger pulses, followed by a much larger pulse. This is done so that the target is gradually compressed, avoiding overheating. The green line shows the amount of power from the laser that was absorbed by the target, which was 85.6% integrated over the laser pulse. The red line is scattered power.

3. Optimization of Parameters

To achieve a uniform implosion, beams were moved in both the θ and φ directions [Fig. 3]. Moving the rings' θ angles towards the equator prevented the target from imploding in a "pancake" shape, as seen in Figure 2b. Furthermore, defocusing a beam widens the surface area of its impact, spreading out the energy from the beam [Fig. 5]. The best-focus beam shapes were taken from Ref. 6 and the defocused shapes were calculated following the method of Ref. 7. A variety of different parameter alterations were tested using the two-dimensional hydrodynamics simulation code, *Sage*[8]. Parameters were then altered based on the simulation results and the process was repeated. Earlier work [9] addressed the problem of optimizing direct drive on the LMJ, assuming that all 160 beams were available. However, since every other quad is absent from the framework in 2024, the work of Ref. 9 is inapplicable to the present problem. Another limitation of the earlier work is that it didn't attempt to optimize the azimuthal uniformity by adjusting the aimpoints in the φ-direction.

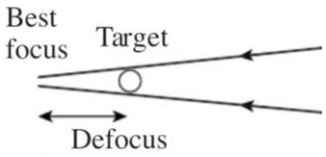

Figure 5. The mechanics of defocusing. By moving the best focus away from the target, the surface area of the beam's impact is widened. (From Ref. 2)

4. Optimized Design for the LMJ at Half-Capacity

Table 1 depicts the positioning of the beams and the defocus used in order to optimize the LMJ direct drive configuration.

Optimal Parameters (80 Beams)				
	Upper Ring 1	**Upper Ring 2**	**Lower Ring 1**	**Lower Ring 2**
$\boldsymbol{\theta_0}$	31.0°	35.5°	46.8°	51.3°
$\boldsymbol{\theta}$	24.7°	55.0°	73.0°	85.0°
$\Delta\boldsymbol{\varphi}$	$\pm$20.0°	$\pm$20.0°	$\pm$20.0°	$\pm$20.0°
Defocus	1.8 cm	1.8 cm	1.8 cm	1.8 cm

Table 1. A table showing the optimized design for the LMJ in 2024. Upper ring 1 refers to the ring of aimpoints that corresponds to the upper beams of ring 1; the rest of the column names follow this same naming pattern. All of the θ angles in the top hemisphere are reflected across the equator onto their corresponding angles in the bottom hemisphere. Beams in the same quad are moved by $\Delta\varphi$ values (measured relative to the center of the quad) that are equal in magnitude to one another. θ_0 indicates the initial positioning of each ring on the target chamber. [Run 1056]

The (θ, φ) coordinates of the quad centers were taken from Ref. 6. The individual beam coordinates (including the Ring 1 and Ring 2 θ_0 values) were calculated assuming nominal 40-cm-square beams with edges separated by 16.1 cm in the horizontal direction and 23.22 cm in the vertical direction, consistent with NIF values. Differences between these coordinates and actual LMJ coordinates are not expected to be significant as the parameters of the design given in Table 1 are all specified in terms of aimpoints. See Section 7.

To compensate for energy gaps created by the missing quads, it is important to change the φ angle of the aimpoints, moving them inwards towards the energy gap as shown in Figure 3. Furthermore, the θ angles of most aimpoints were moved closer to the equator than

the initial angles θ_0 of the beams. This was done to avoid depositing too much energy at the poles of the target, thereby creating a more uniform implosion. Differently, upper ring 1 was not shifted towards the equator. Due to the shifts away from the poles of the other rings' beams, it was necessary to compensate for this loss of energy at the poles by repointing upper ring 1 closer to the poles of the target. Additionally, the implosion became more uniform as the beam defocus approached 1.8 cm. However, defocusing the beam farther caused too much energy to be lost and decreased the uniformity of the implosion.

The progress of the target's implosion is easily visible 7 ns after the laser is fired. At this point, the target has moved in an average of 226 μm towards the target's center. As shown in Figure 6a, the target's implosion is very uniform, the average (*rms*) variation of distance being only 2.06 μm. The average shell velocity in the θ-direction is very uniform with the *rms* nonuniformity *v-rms-*θ = 0.91% [Fig 6b]. This was calculated by dividing the *rms* distance nonuniformity by the distance moved. Furthermore, Figure 6b provides a visual indication of the locations of the implosion's greatest nonuniformities. The maximum of the graph around 90° means that the target's radius was greater than average at the equator. This implies that less energy, on average, was received by the equator than by the rest of the target, compressing the target less. Oppositely, the radius diminishes at about 75° and 105°, which are the areas slightly removed from the equator. Future designs could work on decreasing this nonuniformity around the equator by shifting some beams slightly closer to the equator. There is also a noticeable spike in radius at one of the poles. However, this is most likely due to noise in *Sage* rather than from any true nonuniformity in the design.

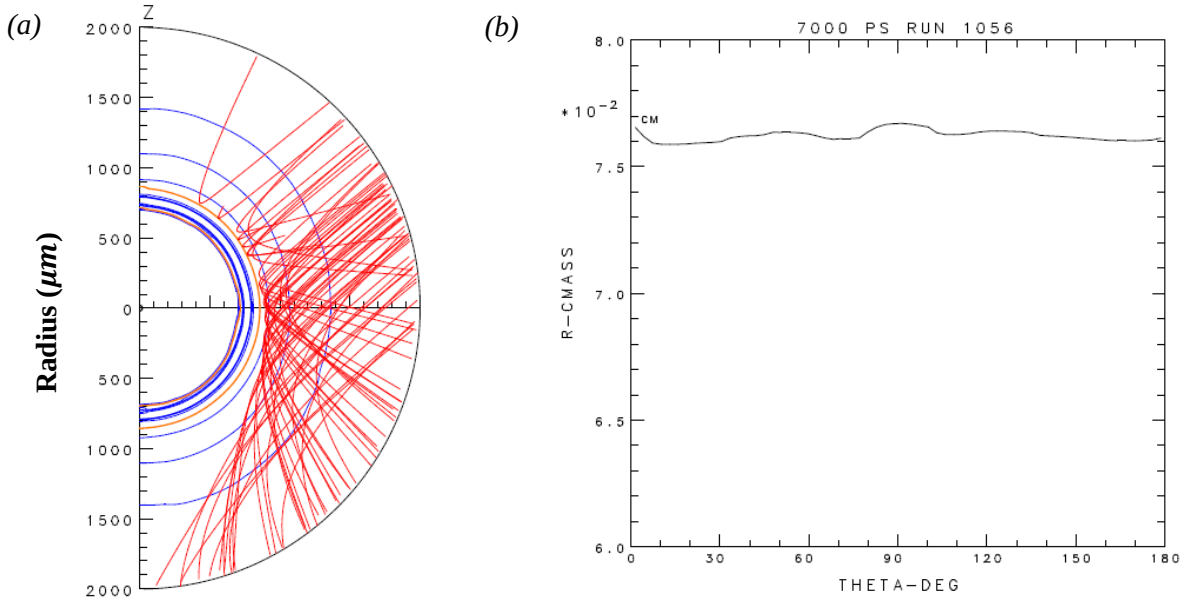

Figure 6. (a) A cross-section of the target 7 ns after the implosion began. When a ray is cut off, that implies that 99% of the ray's energy was absorbed by the target. The blue lines are electron density contours and the orange line represents the critical density, the highest density to which a laser ray can propagate. (b) The center-of-mass radius (in cm) as a function of θ at 7 ns.

When the azimuthal direction is included in obtaining the *v-rms*, good overall uniformity of 2.03% is achieved [Fig. 7]. The center-of-mass radius varies between -11.73 μm and 13.08 μm away from the average center-of-mass radius. Figure 7 provides information that aligns with the observations made from Figure 6b. The blue areas indicate where the center-of-mass radius is greater than average, in particular at the equator, while the red areas indicate a smaller radius. Furthermore, Figure 7 emphasizes the design's uniformity, as the radius differs from the average by less than one contour level at most areas on the target.

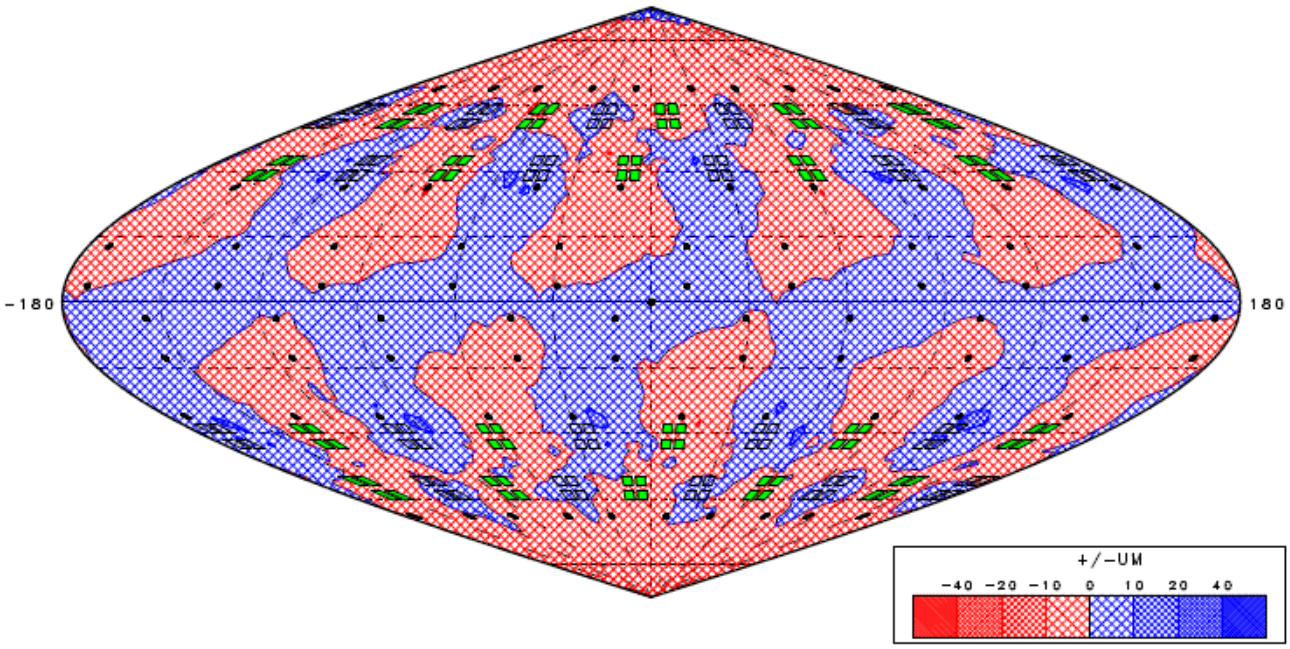

Figure 7. A contour plot of center-of-mass radius variations at 7 ns. [Run 1056]

From the overall *v-rms* of 2.03%, and the *v-rms-θ* of 0.91%, the *v-rms-φ* may be calculated using the following formula:

$$v\text{-}rms^2 = v\text{-}rms\text{-}\theta^2 + v\text{-}rms\text{-}\varphi^2 \qquad (1)$$

When the variables are replaced with their respective values, the following equation is evaluated:

$$2.03^2 = 0.91^2 + v\text{-}rms\text{-}\varphi^2 \qquad (2)$$

showing that the *rms* variation in the *φ*-direction is *v-rms-φ* = 1.81%. This is clearly larger than the *v-rms-θ*, meaning that the nonuniformities lie more heavily in the *φ*-direction.

All tested deviations from the parameters of Table 1 caused an increase in the overall *v-rms*. For example, decreasing the Lower Ring 2 *θ* by 0.2° resulted in the *v-rms* increasing to 2.59%. Similarly, the *v-rms-θ* increased to 1.90%. However, the *v-rms-φ* decreased to 1.75%, implying that moving the Lower Ring 2 aimpoints towards the poles would make the design more

longitudinally uniform, but less latitudinally uniform. This is the case for some, but not all other alterations of the parameters in Table 1. In some cases, beam shifts caused increases in both θ and φ *v-rms*. The results of calculating the various aspects of velocity uniformity were used in deciding which shifts or defocusing were needed to further optimize the design.

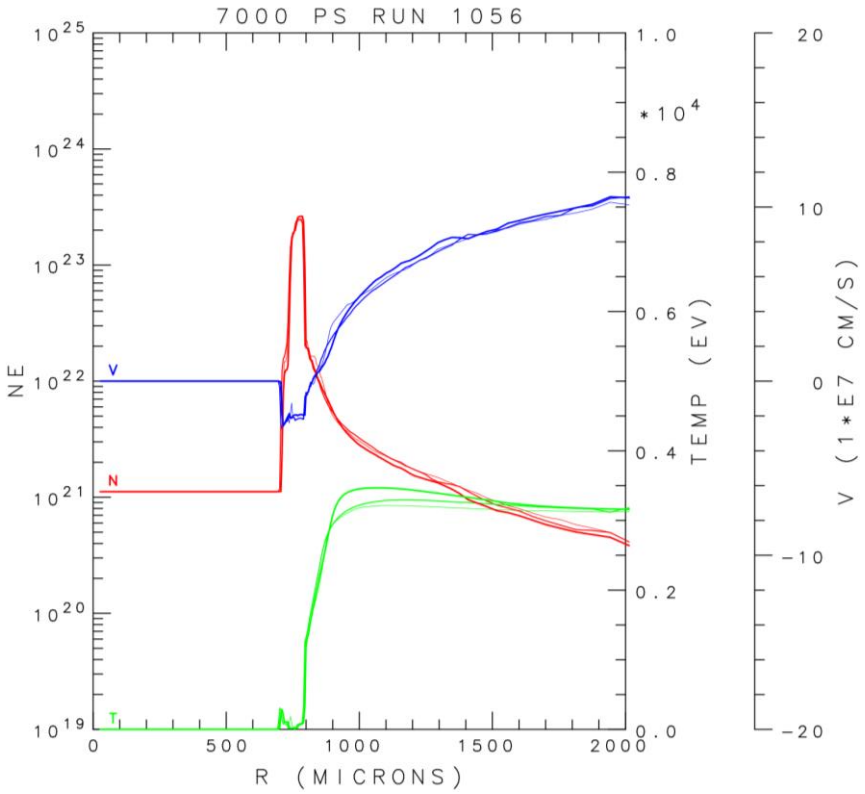

Figure 8. 1-D lineouts vs radius of electron temperature (eV, green), electron density (electrons/cc, red), and velocity in the radial direction (cm/s, blue). For each quantity, three lineouts are superposed at thetas of 1.45° (light), 45.00° (medium), and 88.55° (heavy). The almost exact overlays demonstrate the high uniformity.

Figure 8 provides further proof of this design's high levels of uniformity. It shows curves depicting the electron temperature, electron density, and radial velocity of the target during the implosion. The electron temperature is higher on the outside of the target but falls off to a lower value inside the target. As energy is conducted into the target, the outer layer of the shell is heated and ablates off the target. The second curve, electron density, shows low density at time

0, everywhere except for where the initial shell is. As plasma ablates and moves outwards, the opposing force moves the shell inwards. In the center, the density of the undisturbed gas remains a constant 10^{21}/cc. Furthermore, the third curve, velocity, is positive in almost all places, showing a movement outwards. The shell's negative velocity depicts its inward motion. Since the three different curves taken from 1.45°, 45.00°, and 88.55° in the θ-direction are shown to overlay each other almost exactly, it can be assumed that the electron temperature, electron density, and velocity of the target remain uniform during the implosion.

Moreover, the uniformity is even better than what one might initially think; the main goal is to match the density profiles (showing that the shell moves with the same speed), which this run does exceedingly well. Additionally, in order to perform polar direct drive, the temperature at $\theta = 90°$ must be slightly higher, as seen in the electron temperature profiles. This is because the energy deposited near the equator is deposited further from critical (the maximum density to which the laser can propagate), and therefore drives the shell less effectively. Overall, the results of Figure 8 confirm the high uniformity of this design.

5. Optimized Design for the LMJ at Full Capacity

When the LMJ is fully developed, it will need a different beam configuration in order to facilitate a uniform implosion. Those parameters are shown in Table 2.

Optimal Parameters (160 Beams)				
	Upper Ring 1	**Upper Ring 2**	**Lower Ring 1**	**Lower Ring 2**
$\boldsymbol{\theta_0}$	31.0°	35.5°	46.8°	51.3°
$\boldsymbol{\theta}$	24.5°	55.0°	73.0°	86.0°
$\Delta\boldsymbol{\varphi}$	±5.5°	±5.5°	±5.5°	±5.5°
Defocus	1.8 cm	1.8 cm	1.8 cm	1.8 cm

Table 2. A table showing the optimized design for the LMJ at full capacity. [Run 1093]

While there are some minor changes in the θ-direction in comparison with Table 1, the most significant alteration comes in the φ-direction. The Δφ decreases from ±20.0° to ±5.5° [Table 2]. This is due to the difference in configuration of the LMJ at half capacity, compared to the LMJ at full capacity. When the LMJ is at full capacity, there will be twice as many beams active, meaning that the energy gaps that plagued the half capacity facility will not be present. Therefore, there is less of a need to strongly alter each beam's Δφ.

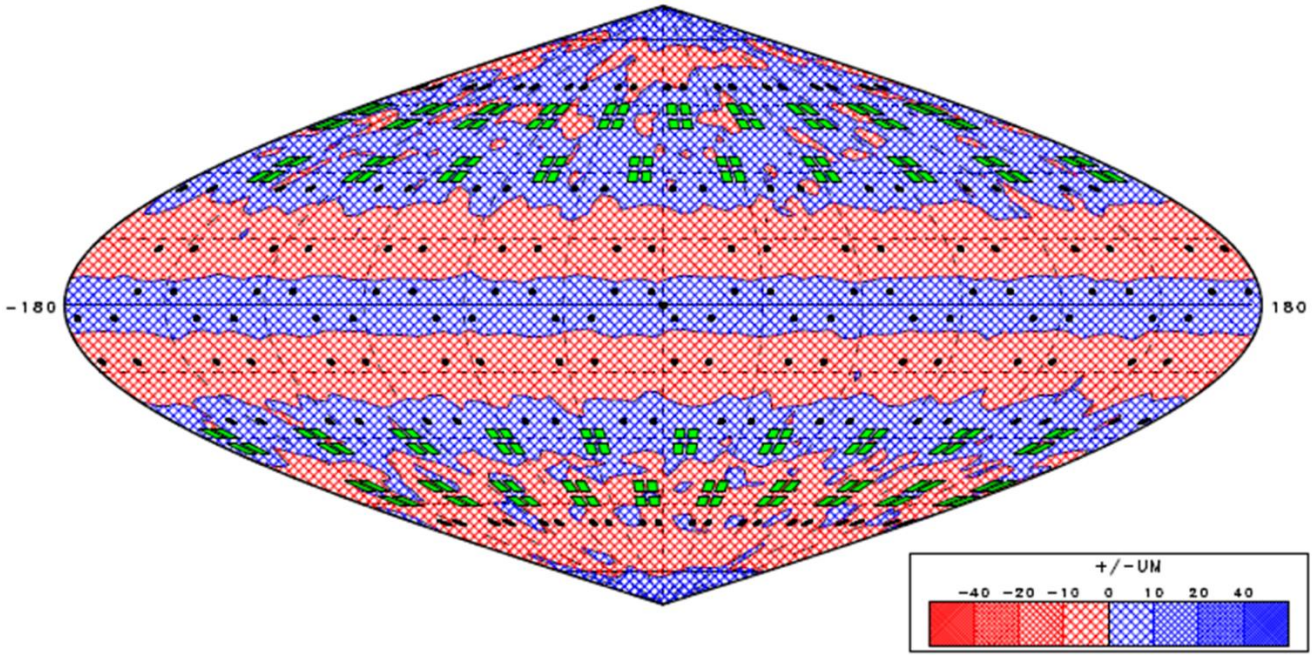

Figure 10. A contour plot of center-of-mass radius variations at 7 ns when the LMJ is at full capacity. [Run 1093]

Even better uniformity is achieved when all beams are active, with the energy of each beam halved so that the same total energy is delivered to the target. The overall *v-rms* is 0.98%, which is a significant decrease from 2.03% [Fig.10]. Furthermore, the *v-rms* in the θ-direction is 0.82% and the *v-rms* in the φ-direction is 0.53%. In contrast with the half capacity optimized configuration, the full capacity configuration is more uniform in the φ-direction than in the θ-direction. Moreover, the center-of-mass radius varies between -5.19 μm and 5.89 μm around the average radius, which is about half the range of the half capacity configuration. Likewise, in terms of absorption, the full capacity design was more efficient, absorbing 87.3% (rather than 85.6%) of the energy from the beams.

6. Conclusion

This work proposes beam configurations that will optimize the uniformity of a direct drive implosion on the LMJ, which is designed for indirect drive implosions. The 2-D hydrodynamics code *Sage* was used to simulate different configurations when optimizing each solution. Good uniformity was achieved by adjusting the aimpoints and defocuses of the beams. When the LMJ is at half capacity, it may reach uniformity levels of 2.03%, and when it is at full capacity, it can attain improved uniformity levels of 0.98%.

7. Note Added

Since the simulations reported here were carried out, the actual individual LMJ beam coordinates were made available [10]. The coordinates used for the work reported here, estimated as described in Section 4, turned out to be very close to the actual coordinates. The θ values were all within 0.1° and the φ values were all within 0.5°, so no modifications are necessary to the designs given here. Indeed, when the half-capacity design of Section 4 (Run 1056) was rerun with the actual coordinates, the uniformity changed by an insignificant amount (from 2.03% to 1.98%) as did the absorption (from 85.6% to 85.2%).

8. Acknowledgements

I would like to thank Dr. Craxton for his invaluable guidance and support on this project. He made this internship a wonderful opportunity for growth. Furthermore, I would like to

thank the entire LLE community for providing this opportunity to both myself and future students.

9. References

1. “Pursuing Fusion Ignition,” National Ignition Facility & Photon Science (2021).

2. A. M. Cok, “Development of Polar Direct Drive Designs for Initial NIF Targets,” Laboratory for Laser Energetics High School Summer Research Program (2006).

3. W. Wang, “Development of a Beam Configuration for the SG4 Laser to Support both Direct and Indirect Drive,” Laboratory for Laser Energetics High School Summer Research Program (2020).

4. P.A. Norreys et al., LMJ-PETAL Facility : Letter of Intent, “Measuring 1-D like behaviour of a 240 kJ low convergence ratio hydrodynamically equivalent ICF capsule,” (2020).

5. R.W. Paddock, private communication (May 2021).

6. LMJ-PETAL Users Guide, Version 2.0, CEA, France.

7. A. M. Cok et al., “Polar-drive designs for optimizing neutron yields on the National Ignition Facility,” Phys. Plasmas 15, 082705 (2008).

8. R. S. Craxton and R. L. McCrory, “Hydrodynamics of Thermal Self-Focusing in Laser Plasmas,” J. Appl. Physics. 56, 108 (1984).

9. L. M. Mitchell, “Exploration of the Feasibility of Polar Drive on the LMJ,” Laboratory for Laser Energetics High School Summer Research Program (2009).

10. B. Canaud, private communication (November 2022).

Optimization of Direct Drive Designs for a Proposed Dual Direct/Indirect Drive Laser

Meghan Marangola

Brighton High School

Rochester, NY

Advisor: Dr. R. Stephen Craxton

Laboratory for Laser Energetics

University of Rochester

Rochester, NY

May 2023

1 Abstract

This work investigates the possibility of amending the design of a proposed octahedral laser system to allow for direct drive. Lan et al. proposed this design, which is configured for indirect drive and uses a spherical hohlraum as opposed to a cylindrical hohlraum. The target chamber has 48 quads, each comprised of four laser beams; beams enter the hohlraum through six laser entrance holes. In the amended design, minor changes are made to beam port locations and the laser beam pointings are adjusted for direct drive. The 2-D hydrodynamics simulation code SAGE was used to optimize the pointings. Various beam spatial profiles and radii were investigated. Designs were found with nonuniformity values as low as 0.57% rms, which are comparable to simulations for a similar system (UFL-2M) under construction in Russia. Tuning scans provide a preliminary estimate of the required system pointing accuracy. These results show that the amended design promises high-quality spherical direct drive implosions.

2 Introduction

High uniformity values are essential for achieving ignition through inertial confinement fusion (ICF) of a spherical capsule. ICF is the process of heating up and compressing a capsule in an attempt to create nuclear fusion reactions. Capsules are spherically shaped and typically consist of plastic or glass shells filled with deuterium and tritium, two isotopes of hydrogen. A typical capsule diameter is a few millimeters. The two types of laser-driven ICF are known as direct drive and indirect drive. In direct drive, as shown in Fig. 1, the laser beams hit the capsule directly (Step 1), after which the shell ablates outward, causing the center of the capsule to compress inward (Step 2). Then, the fusion reactions are ignited in the center of the capsule (Step 3), after which alpha particles from the initial fusion reactions are deposited in the surrounding fuel, leading to a propagating burn (Step 4).

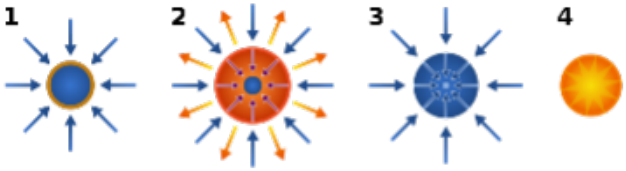

Figure 1: Diagram depicting the process of direct drive inertial confinement fusion. The blue circle is the capsule, with the blue arrows representing the laser irradiation. The fourth image represents the capsule reaching thermonuclear burn.

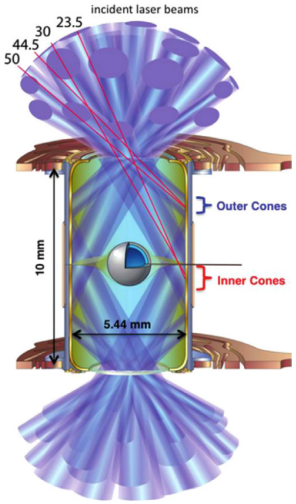

Figure 2: Diagram depicting lasers entering a cylindrical hohlraum, heating up its walls. X rays from the heated hohlraum then irradiate the capsule, shown by the gray sphere. The gold vertical cylinder is the hohlraum. The laser beams are shown in dark blue. Figure from [1].

Indirect drive fusion, as shown in Fig. 2, utilizes a hohlraum, which is usually made of gold. Lasers enter the hohlraum through laser entrance holes (LEH's) at the top and bottom of the hohlraum, and deposit energy onto its inner walls. The energy heats up the walls, which emit x rays that then irradiate the capsule inside.

Until now, indirect drive lasers have been designed for use with cylindrical hohlraums. Because the two LEH's for cylindrical hohlraums are separated by 180°, the optimal beam configuration on the target chamber is to concentrate the beams around two poles across from one another. However, in lasers designed to achieve uniform direct drive irradiation, laser ports are evenly spaced around the target chamber. No lasers have been designed for both direct drive and indirect drive with a cylindrical hohlraum because of the difference

in optimized configurations of laser beams around the target chamber. Laser systems like the National Ignition Facility (NIF) are designed for use with cylindrical hohlraums. Although some lasers can run both types of shot, albeit not with optimum efficacy, every multibeam laser that exists today was designed for either indirect or direct drive.

Lan et al. [2] have proposed a design that uses indirect drive through a spherical hohlraum with six LEH's, also referred to as an octahedral hohlraum because the LEH's lie on the vertices of an octahedron. This hohlraum design, pictured in figures 3 and 4, is a sphere with six LEH's that are positioned as if centered on the faces of a cube. The cubic geometry of the hohlraum is highlighted by the outline of the cube in Fig. 3, which makes it easier to visualize the superimposition of the cube onto the surface of the sphere.

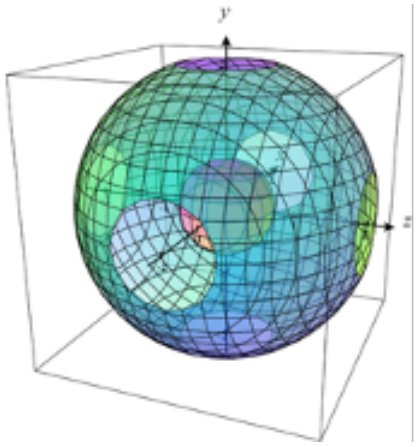

Figure 3: Diagram of an octahedral hohlraum, where the larger sphere with holes represents the hohlraum, the inner sphere represents the capsule, and the cube illustrates the cubic symmetry of the geometry.

The laser that Lan et al. proposed has 48 beams, eight of which would enter each laser entrance hole during a shot, as in Fig. 4. The geometry also works with 48 quads, which are groups of four beams that are more functional on a larger laser system like the NIF. The beams are arranged on six rings in the target chamber, which are 55° from the normal line to each LEH. While there are more LEH's than there would be for a cylindrical hohlraum, the design allows for smaller LEH's. The beam sizes in the LEH plane are constrained by the requirement that the total power per unit area should not exceed the threshold for laser-plasma instabilities. Thus, the area of the spherical hohlraum that is open is the same as that for the cylindrical hohlraum, and to lowest

order there are no significant differences in the total energy loss.

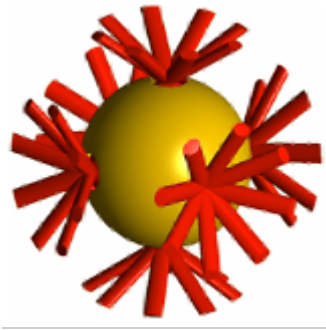

Figure 4: Diagram depicting laser beams (red) entering a gold octahedral hohlraum around an indirect drive capsule, from [3].

2.1 Lan and Amended Lan Configurations

The Lan beam configuration is shown in Fig. 5a. First note the geometry of the diagrams themselves; the spheres are shown in two dimensional images, where due to the stretched display the entirety of the sphere is visible. The black lines, when in three dimensions, form the cube shown in Fig. 3, and the blue line is circular in three dimensions. The Lan configuration has the beams in the target chamber centered on rings that are offset at 55° from the normal line to the center of the laser entrance hole, for all six LEH's. The beams are color coded by the laser entrance hole to which they correspond. The LEH's are aligned with the faces of the cube, as shown in Fig. 3. The geometry is ideal for indirect drive, as eight beams enter each LEH and disperse evenly about the hohlraum. The laser design proposed by Lan et al. has very good uniformity for indirect drive [2].

However, the beam distribution around the six LEH's, instead of at the poles as for cylindrical hohlraums, hints at the possibility of direct drive use. The cubic edges superimposed on the sphere highlight the concentration of the beams in this geometry near the edges of the cube, and especially near its corners. This is not optimal for direct drive, as the beams will deposit more energy on the corners of the cube than on its faces, and uneven energy deposition leads to higher nonuniformity.

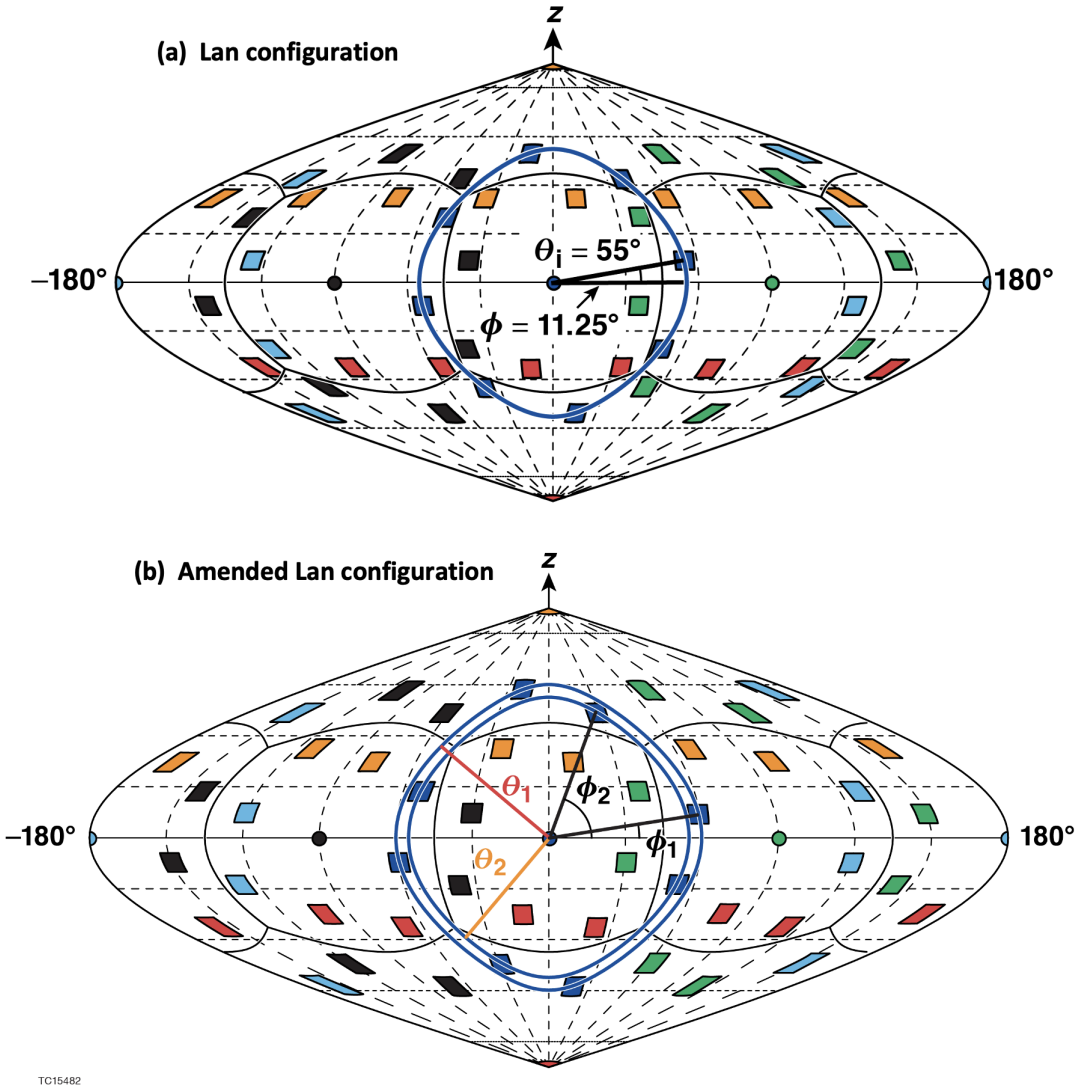

Figure 5: The Lan and amended Lan configurations. Figures (a) and (b) show the locations of the ports on the respective target chambers. The black curves indicate the projection of a cube onto the spherical surface.

Wang [4] worked on an amended configuration shown in Fig. 5b that promises improved direct drive capabilities. The slight differences in beam placement with the amended geometry of Fig. 5b create significant direct drive advantages. Instead of having all beams at a θ offset of 55°, four beams from each ring are shifted to a 60° offset, while the others are left with $\theta = 55°$. Shifting half of the beams creates two groups of 24 beams, with all beams within each group being equivalent. Symmetry requires that each beam can be rotated to four positions on each of the six faces.

In Fig. 5b, the original offset is shown as $\theta_2 = 55°$, while the amended offset for half the

beams is $\theta_1 = 60°$. In the other direction, beams with $\theta_1 = 60°$ have $\phi_1 = 11.25°$, while the $\theta_1 = 55°$ beams (every other beam) have $\phi_2 = 45° + 22.5°$. These geometry changes lessen the beam clustering around the corners of the cube and improve the energy deposition on the cube's centers. The amended configuration's indirect drive capabilities match those of the Lan configuration, as shown by Wang [4].

2.2 UFL-2M Configuration

A laser system is under construction in Russia, known as UFL-2M [5] and later as the "Russian laser facility" [6]. It will be referred to as UFL-2M here. This laser was designed for optimum direct drive uniformity and can also be used for indirect drive with an octahedral hohlraum. The target chamber is shown in Fig. 6 and the port configuration in Fig. 7. As for the Lan configuration, the geometry is cubic with 8 beams per cube face. In this configuration all beams are evenly spaced around a cone at 30° from the normal to the cube face [7]. For indirect drive, all beams enter the LEH on the adjacent face of the cube, with an angle of incidence of 62.5° to the LEH normal.

Figure 6: Image of the target chamber of the UFL-2M laser from [8]. The target chamber has a cubic geometry, with 8 beams on each face of the cube.

The configuration has striking symmetry, indicating its potential for direct drive use. A fundamental difference between this configuration and Lan's is that the latter has non-opposing beams, allowing beam dumps like those on the NIF, at which any energy that

does not hit the target, including unconverted energy from frequency conversion, would be deposited. In the UFL-2M configuration there are opposing beams where the beam dumps would be. Thus, additional measures are needed for this configuration to prevent energy not absorbed by the target from entering the opposing port and damaging optics.

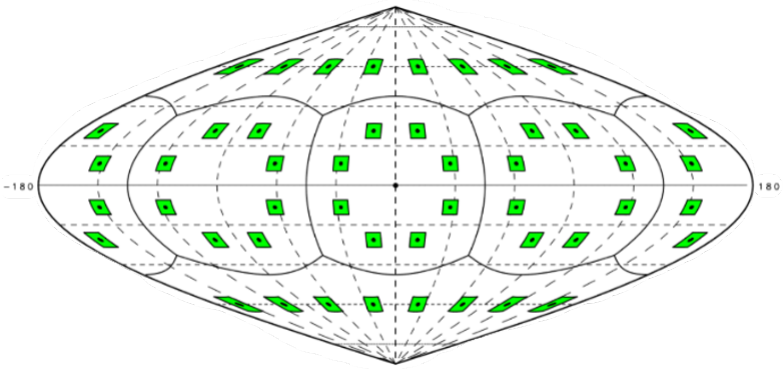

Figure 7: Figure showing the beam ports of UFL-2M overlaid on a sphere.

Section 3 describes the different parameters of the problem and how they contribute to the overall uniformity of the implosions for the 48-beam systems. Section 4 describes the changeable parameters on the 60-beam OMEGA system.

3 Assessment of Direct Drive Uniformity

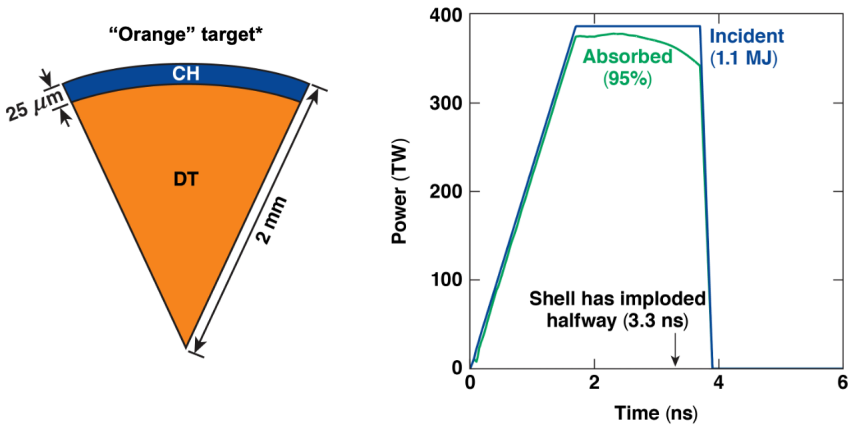

Figure 8: Figure depicting the "Orange" target [9] from NIF shot N190227-001 and the incident and absorbed laser pulses. This target was chosen to compare the NIF and proposed octahedral geometries for direct drive. Figure from [10].

Figure 8 displays a cross-section of the "Orange" target that was shot on the NIF [9] alongside a graph of the beam pulse power and the predicted target absorption. For each shot, there are many parameters that factor in to the uniformity of the implosion. Simulations are helpful in exploring the effects that each parameter has on the uniformity.

The simulations in this paper were run using the 2D hydrodynamics code SAGE [11]. To simulate the configurations, the hydrodynamics was only run in 1D; as the nonuniformities are 3D, there is no advantage to modeling in 2D. However, because the nonuniformity values are low, the simulations in one dimension provide a sufficient approximation of the basic target evolution. Laser deposition is modeled using 3D ray tracing. Laser rays follow curved ray paths along which the ray energy is deposited. The energy is then transported by thermal conduction to the solid density shell, which is accelerated inwards. Deposited energy is stored as a function of θ and ϕ, then integrated over time. Here θ is the angle from the z-axis and ϕ is the azimuthal angle about the z-axis; these angles should not be confused with the angles shown in Fig. 5. The time-integrated 3D deposition patterns are used to characterize the 3D uniformity values, as the root mean square (rms) deviation of this deposited energy σ_{rms} is calculated. As the nonuniformity of the velocity of the imploding shell is $\sim$72% of the deposition nonuniformity [9], the velocity uniformity is better than the deposition uniformity calculated with SAGE. All nonuniformity values reported in this paper are deposition nonuniformity. Many experiments on the NIF have been modeled using SAGE [12] [9].

Section 3.1 describes the parameters that can be controlled using SAGE. Section 3.2 follows, comparing the three 48-beam configurations with center pointing, after which there is a discussion (Section 3.3) on the optimization of the UFL-2M configuration. Then, the optimal parameters for the amended Lan configuration are presented (Section 3.4), followed by a discussion of their sensitivity to changes (Section 3.5). Finally, there is a comparison of the three 48-beam systems for a flat beam setup (Section 3.6).

3.1 Laser Beam Parameters

This section describes problem setups, and defines each of the parameters that were optimized. Results begin in Section 3.2.

3.1.1 Super-gaussian Index

The super-gaussian index is a variable that changes the beam shape. The shapes are governed by the following formula for the beam intensity I as a function of radius r

$$I(r) = I_0 \cdot exp\Big[- \Big(\frac{r}{r_0}\Big)^n \Big], \tag{1}$$

where I_0 is the peak intensity, n is the super-gaussian index, and r_0 is the beam size corresponding to the $\frac{1}{e}$ intensity cutoff. Examples are given in Fig. 9 for $r_0 = 1200$ µm and values of n ranging from 1 to 20.

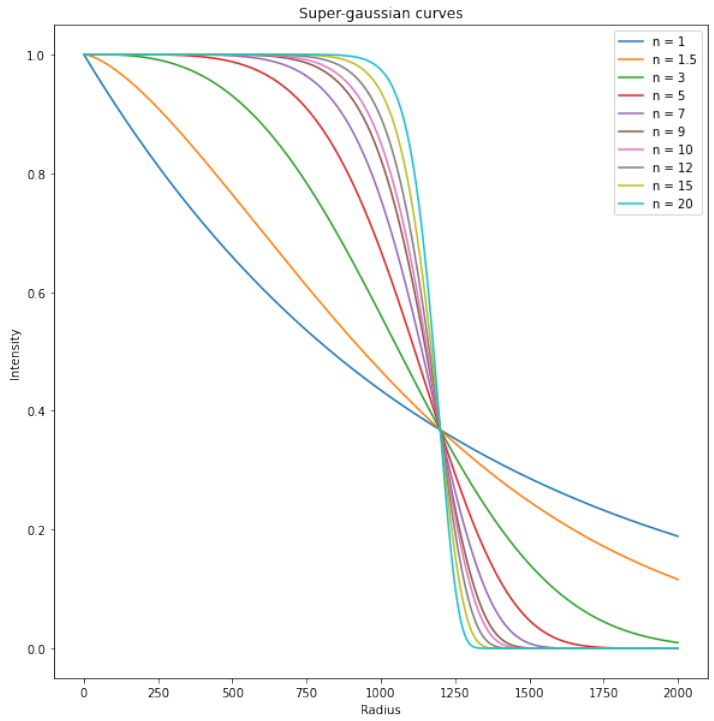

Figure 9: A graph of different super-gaussian beam profiles, with $r_0 = 1200$ µm and a variable n-value.

The variable n controlling the super-gaussian index in SAGE allows the beam spatial profile to be adjusted. With an index of 2, the beam's intensity profile is a simple bell

curve; as the n-value increases, the beam drop-off gets increasingly steep, and the intensity plateaus in the center, essentially creating a flat beam. On current lasers the beam profiles are created using phase plates. The runs presented here assume custom phase plates can be designed for future laser facilities.

3.1.2 Beam Radius

The r_0 value corresponds to the beam's radius. With overall increase of the r_0 of the laser beams for a fixed target radius, the uniformity is expected to improve, which is logical; larger beams will have increasing overlap and distribute their energy over a wider area. However, as the beams become larger than the target, more energy misses the target completely and the overall absorption decreases drastically. High energy absorption is desirable due to the high cost of laser energy. Thus, although runs with r_0 significantly larger than the target radius may have considerably lower nonuniformity values, they are both unrealistic and not feasible.

3.1.3 Ray Resolution in SAGE

Within the SAGE code, the user can select the number of rays with which to run each simulation, or the run's "resolution". There are two directions of deposition for the rays, so there are two resolution parameters: number of rays per time step in the r direction, and number of rays in the θ direction, with r and θ here referring to a circular grid in the cross section of the beam. Originally, all runs occurred with 10x12 resolution in r and θ, respectively, taking about forty-five minutes to an hour for each run. As the run resolution increases, the run takes longer, with the longer runs taking up to 12 hours at 40x48 resolution. However, the higher resolution runs give a much more accurate estimate of the nonuniformity and energy deposition patterns, illustrated by the series of runs shown in Fig. 17 (Section 3.5.3). The precision increase from increasing the number or rays is especially important for runs with σ_{rms} values below 1%, as low resolution in the code can be misleading when finding the nonuniformity for the shot.

3.2 Comparison of the Three Configurations with Center Pointing

To compare the performance of the three 48-beam systems on the same shot metrics, the runs have an r_0 value of 1500 µm, a super-gaussian index of 2.7, and beams with no repointing. The three resulting graphs are shown in Fig. 10.

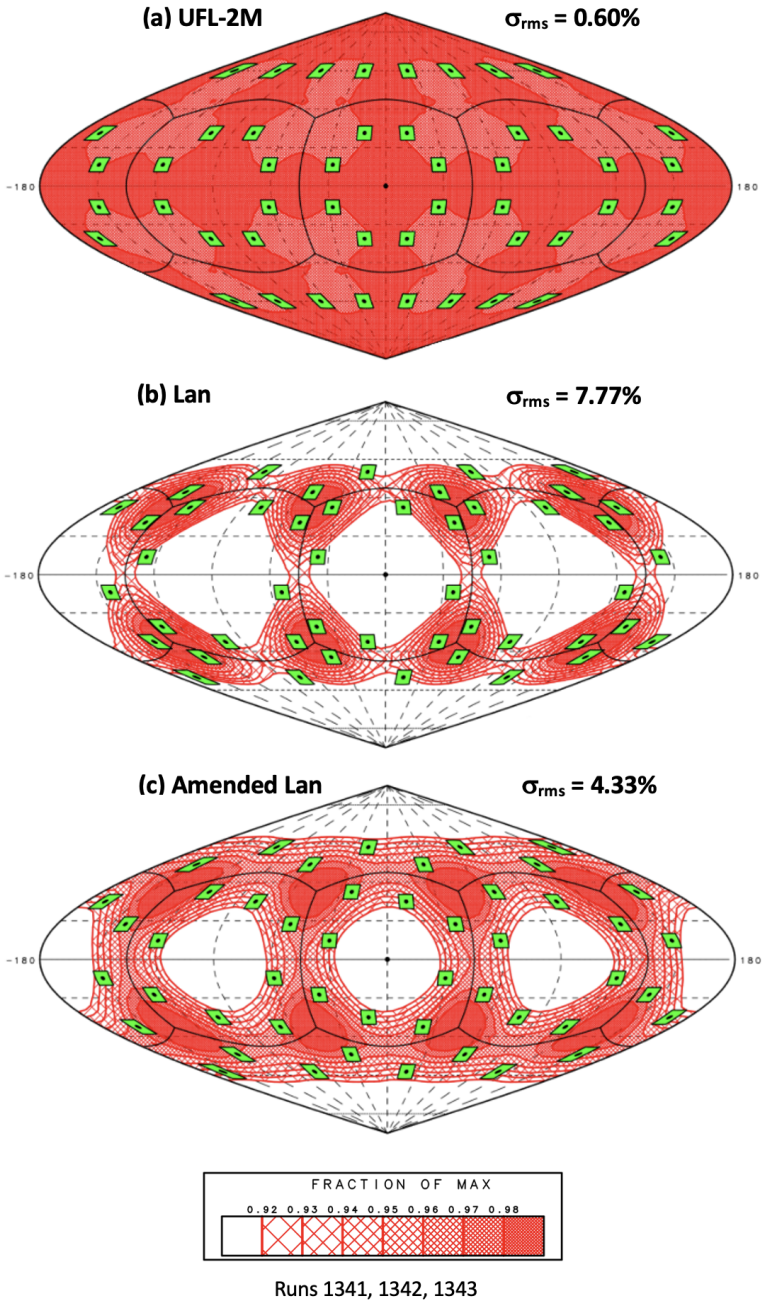

Figure 10: Comparison of contours of time integrated deposited energy for (a) UFL-2M, (b) Lan, and (c) amended Lan configurations with super-gaussian index n of 2.7, beam r_0 of 1500 µm, and center pointings. These plots may be compared with figure 19 (a), (b), and (c), respectively, for n = 15 and r_0 = 2500 µm.

As in Figure 5, these figures are 2D representations of spheres. The θ angle measures from the top (north pole) in the vertical direction, while ϕ measures in the horizontal (azimuthal) direction. As shown in the legend, the red shading on the graphs represents the fraction of the maximum energy deposited at each point, and the contour levels range

from 92% to 98% of the maximum. The green rectangles represent the locations of the ports on the target chamber, while the black dots represent the aim points of the laser beams. In this case, the black dots align with the centers of the ports because the beams are center pointed. The black outline shows the edges of the cube, a 3D version of which is shown in Fig. 3.

The UFL-2M system performed the best with the lowest σ_{rms} (0.60%), while both the proposed and amended Lan configurations have much higher nonuniformity. As mentioned in Section 2.1, the beams are clustered around the corners of the cube when the Lan configuration is used for direct drive, resulting in significantly less energy deposited in the centers of the cube's faces and a σ_{rms} of 7.77%. The amended design was intended to mitigate some of that effect and improves the uniformity by 3%, to σ_{rms} of 4.33%. However, it is clear that the Lan and amended Lan configurations need significant repointing to achieve more uniform implosions, while the UFL-2M configuration has very low nonuniformity with no correction.

3.3 Optimization of the UFL-2M Configuration

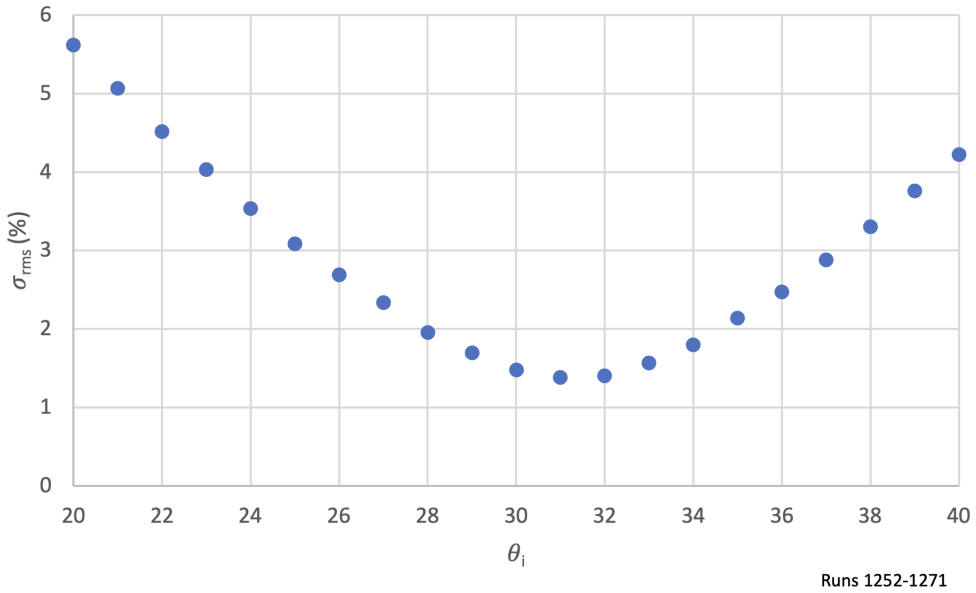

Figure 11: Optimization of the UFL-2M system at center pointings, with super-gaussian index n of 4.7 and r_0 of 1500 µm. θ_i is the angle between the beam direction and the normal to the cube face, and σ_{rms} is the nonuniformity of the time-integrated deposited energy.

To test the UFL-2M system, the θ value of the ports – the angle between the normal and the cube face as described in Section 2.2 – was varied, with no beam repointing. As displayed in Fig. 11, 30° (as found in [7]) is a good port angle to minimize σ_{rms}, but 31° is slightly better. The optimum 30° port angle found in [7] was for a completely different target design and for a shot using green laser light instead of UV. The convergence of optima suggests that the 30° result is more a property of the geometry than of the target design. The geometry of UFL-2M at center pointing achieves very uniform results, meaning no pointing adjustment is necessary.

3.4 Optimization of the Amended Lan Configuration

Given a configuration with the beam port locations on the target chamber fixed, beams can be repointed to improve the uniformity. Similar to the four port angles (θ_1, θ_2, ϕ_1, ϕ_2) introduced in Section 2.1 and shown in Fig. 5b, there are four pointing variables (θ_1', θ_2', ϕ_1', ϕ_2', corresponding to aim points on the initial target surface) in the amended

Lan configuration that can be adjusted in SAGE. One corresponds to the θ value for each set of beams on a 55° ring, one for the θ value for the 60° ring, and one ϕ value for each set of rings. The initial pointings experimented with in this work were those from [4] of $\theta_1' = \theta_1 + 8.5°$, $\theta_2' = \theta_2 + 7.1°$, $\phi_1' = \phi_1 - 0.2°$, and $\phi_2' = \phi_2 - 0.2°$; the run used a super-gaussian index of 3, an r_0 of 1100 μm, and a 10x12 run resolution, which gave a nonuniformity value of $\sigma_{rms} = 1.06\%$. When the angles were changed individually from this set of pointings, none of the changes significantly lowered the nonuniformity. However, combining individual changes that seemed to have slightly opposing effects on the energy distribution patterns created unpredictable and often increasingly nonuniform results. Small changes in the beam spatial profile led to large increases in σ_{rms} (see Fig. 15 below). A different approach to changing the beam pointings was therefore esssential to achieving high uniformity.

Given that the UFL-2M laser configuration had consistently good uniformity values, the beams of the amended configuration were first repointed to the aim points of the UFL-2M configuration. This corresponded to $\theta_1' = \theta_1 + 2.5°$, $\theta_2' = \theta_2 + 7.5°$, $\phi_1' = \phi_1 + 1.25°$, and $\phi_2' = \phi_2 + 10°$. The values of θ_1, θ_2, ϕ_1, and ϕ_2 are given above in Section 2.1.

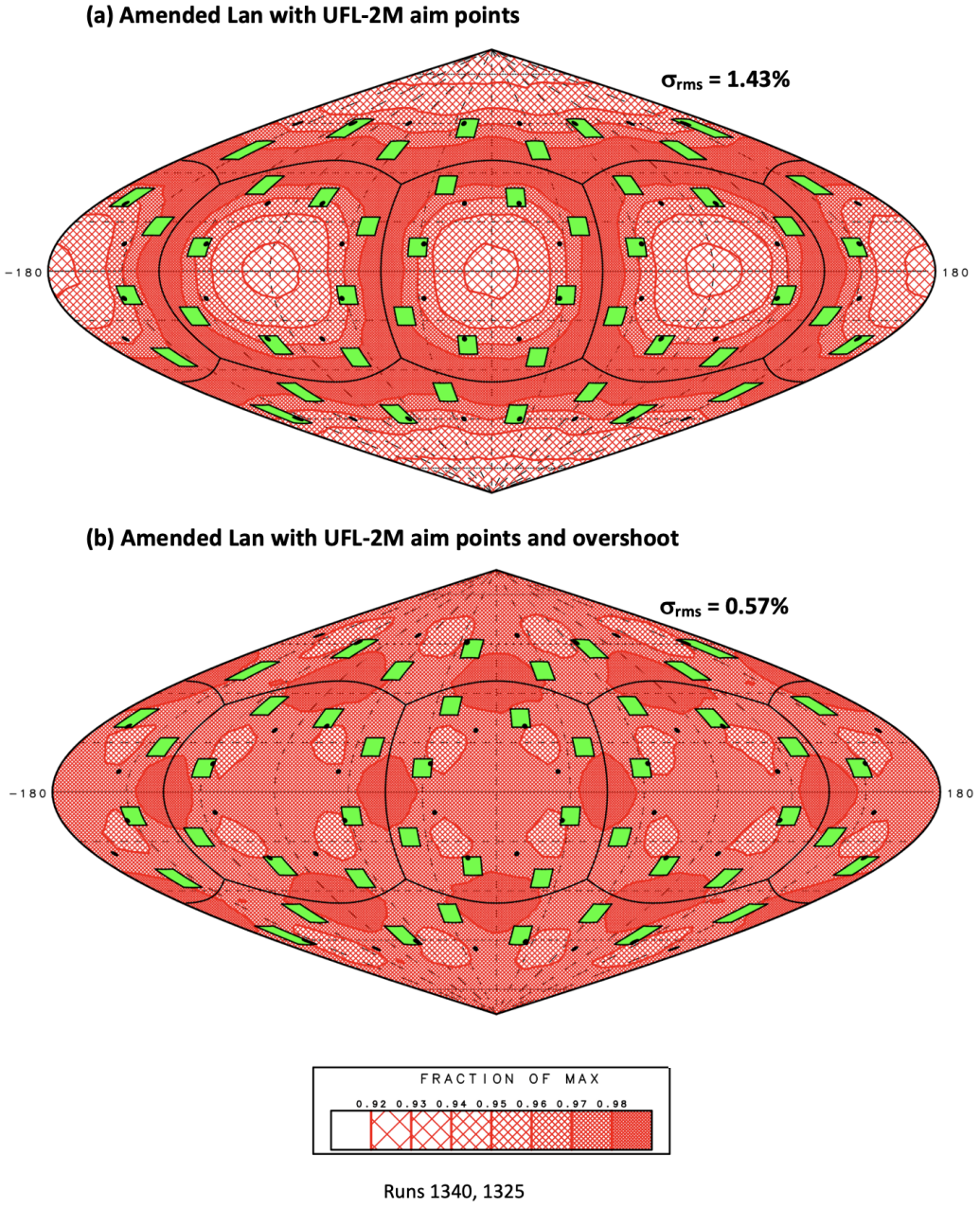

Figure 12: Deposited energy plots for the amended Lan configuration, first repointed exactly to the aim points of the UFL-2M system (a), then with an additional overshoot (b). For both runs, the super-gaussian index n was 2.7 and r_0 was 1500 µm.

The nonuniformity of this simulation, shown in Fig. 12a, was greatly improved at 1.43% (down from 4.33% in Fig. 10c), but remained much higher than the UFL-2M value of 0.60%. The beams of the amended Lan configuration needed further repointing to get the center of the beam energy deposition aligned with the ideal UFL-2M aim point. The optimum configuration, shown in Fig. 12b, was found by increasing the angle shifts

by various fractions of the original shifts. The ideal angle ended up being $\frac{1}{3}$ of the way beyond the UFL-2M aim points, with $\theta_1' = \theta_1 + 3.333°$, $\theta_2' = \theta_2 + 10°$, $\phi_1' = \phi_1 + 1.667°$, and $\phi_2' = \phi_2 + 13.333°$. Thus, the total repointing angle for each odd beam (a combination of the θ and ϕ shifts, measured along a great circle) was 3.64°, and for each even beam was 15.25°. These angles are significantly less than the maximum shift of $\sim 37°$ used for the 4 mm NIF design [9] of Fig. 8.

3.5 Sensitivity of the Amended Lan Configuration to Parameter Variations

3.5.1 Super-Gaussian Index

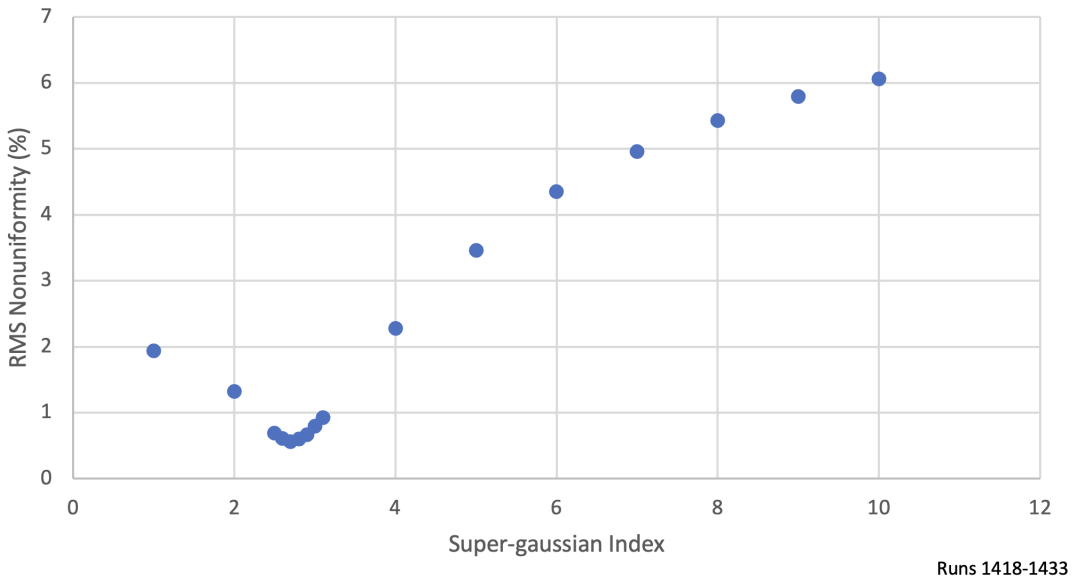

Figure 13: Plot showing changes in RMS nonuniformity due to different super-gaussian indices, with the direct drive pointings used by Wang [4], r_0 of 1100 µm, and resolution of 40x48.

An initial survey of the sensitivity of the amended Lan configuration to the super-gaussian index was carried out using the direct drive pointings and beam radius ($r_0 = 1100$ µm) selected by Wang [4]. The results are shown in Fig. 13, where the radius r_0 and pointings were held constant for all the runs, with a sweep of different index values. The super-gaussian index value of 2.7 yielded the best performance. These results suggest that future

phase plates should shape the beam to a super-gaussian with an n-value of 2.7.

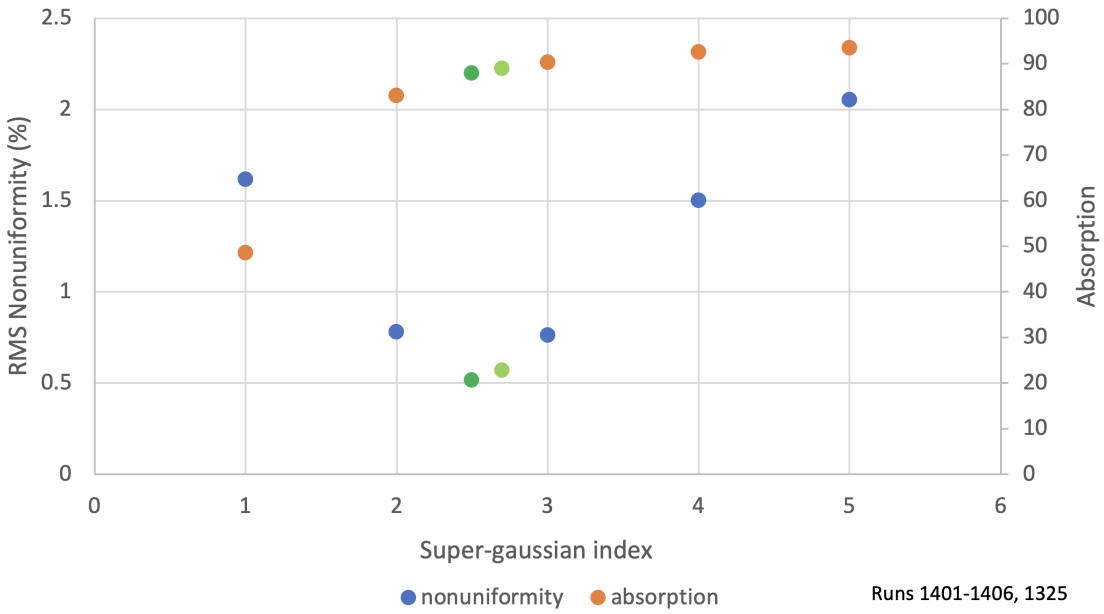

Figure 14: RMS nonuniformity and absorption changes with different super-gaussian indices around the original optimal run from Fig. 12b (n=2.7, shown in light green), with r_0 held constant at 1500 µm. The original optimal run has $\sigma_{rms} = 0.57\%$ and absorption of 88.96%, while the second optimal run (n=2.5, dark green) has $\sigma_{rms} = 0.52\%$ and absorption of 87.91%.

Figure 14 shows a similar plot, but for variations of n around the optimal run of Fig. 12b. The super-gaussian index n on the optimal run was 2.7, and when others were tested in Fig. 14, the RMS nonuniformity value increased, with the notable exception of index $n = 2.5$. Note that in both Fig. 13 and Fig. 14, the optimum super-gaussian index converges around n = 2.7, even with different r_0 values. By varying the values of r_0 and n, optimum values of 1500 µm and 2.7 were chosen. The run in dark green with super-gaussian index $n = 2.5$ has a few tenths of a percentage point better uniformity; however, its absorption drops by a percentage point.

3.5.2 Beam Radius

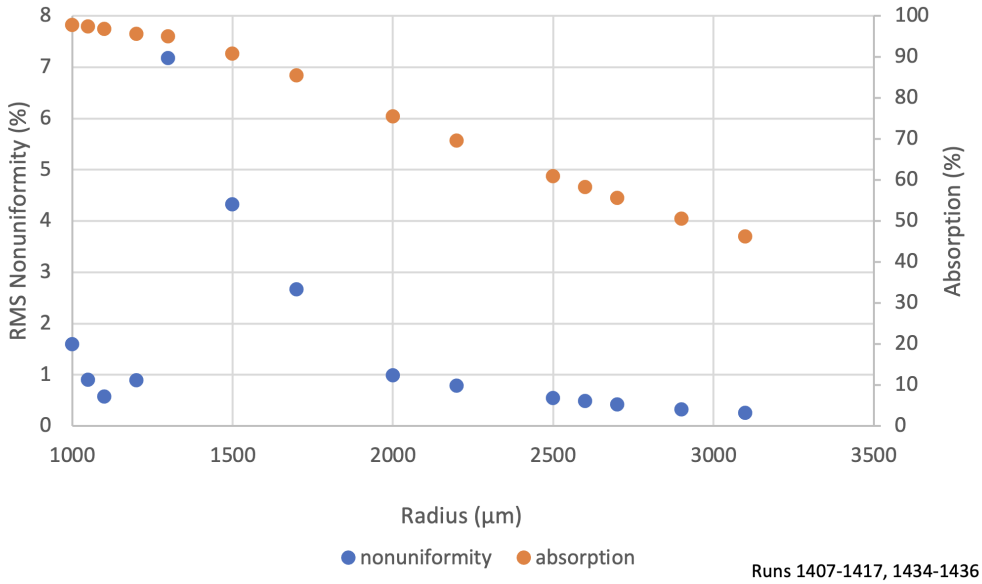

Figure 15: Graph displaying the changes in uniformity with a variable radius r_0, with the direct drive pointings used by Wang [4] and a super-gaussian index of 2.7.

Figure 15 shows the dependence of uniformity on the beam radius r_0, using the pointings selected by Wang [4]. There is a narrow minimum at $r_0 = 1100$ µm with good uniformity, but small changes in radius result in drastic changes in uniformity, so that this value of r_0 should be avoided. There is also a trade-off in absorption with increase in radius, as more energy is refracted around the edges of the target, which influences the choice of optimal r_0.

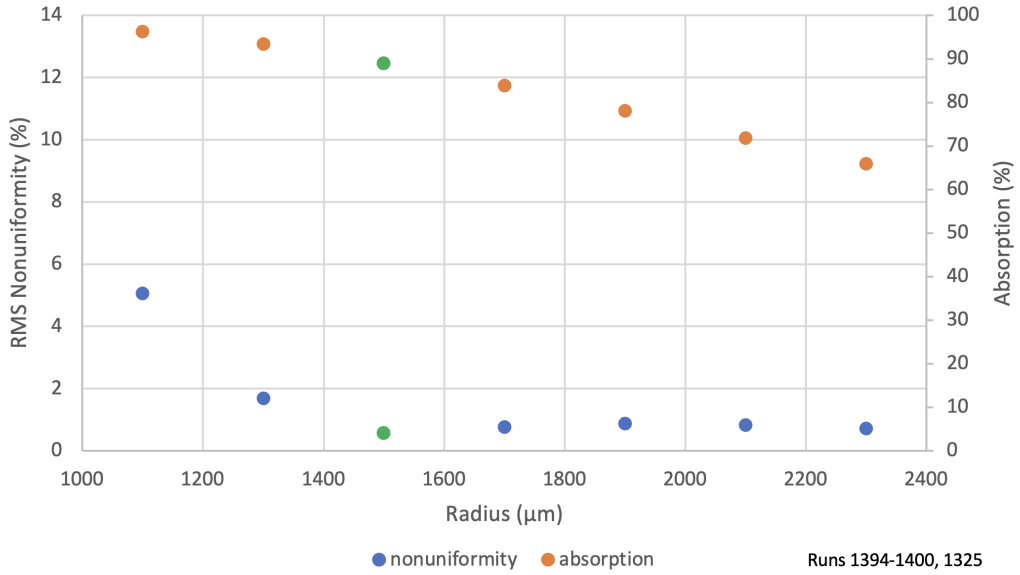

Figure 16: Graph displaying the changes in uniformity and absorption with a variable radius r_0, with the optimal direct drive pointings used for Fig. 12b and a super-gaussian index of 2.7. The optimal run is shown in green, and has an r_0 of 1500 µm.

Figure 16 demonstrates how changes in r_0 around the optimal run affect both the σ_{rms} value and the absorption; the nonuniformity significantly increases with a smaller r_0 value, and there is lower absorption with larger r_0.

3.5.3 SAGE Run Resolution

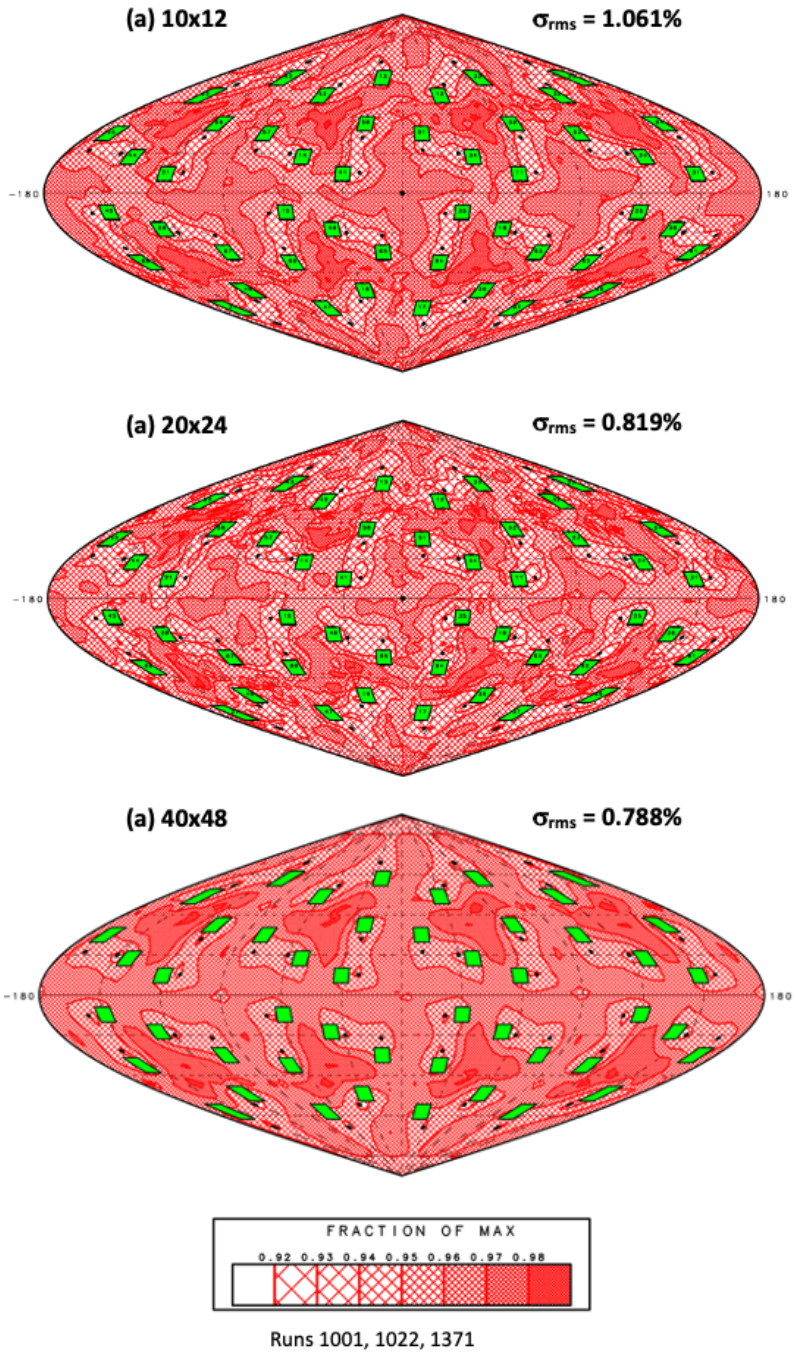

Figure 17: Deposited energy for three runs with identical pointings, super-gaussian index of 3, and r_0 of 1100 µm, but different resolutions.

The runs shown in Fig. 17 are identical aside from the resolution at which they were run. Not only does the nonuniformity drop from the original 1.061% to 0.788%, but the pattern in the highest resolution image is much clearer, which is helpful when trying to improve

uniformity. Outside of this section, all of the runs have 40x48 resolution, meaning 40 radial points and 48 angular points from 0 to 180° on the ray grid. For all beams that are shifted in the azimuthal direction, which is the case for most beams, there are 96 angular points from 0 to 360°.

3.5.4 Pointing Accuracy

The sensitivity to beam pointing errors was investigated. By testing many different angle shifts in the direction of the UFL-2M aim points, the sensitivity of the design to pointing errors in that direction was analyzed. The results are shown in Fig. 18 for the even and odd beams.

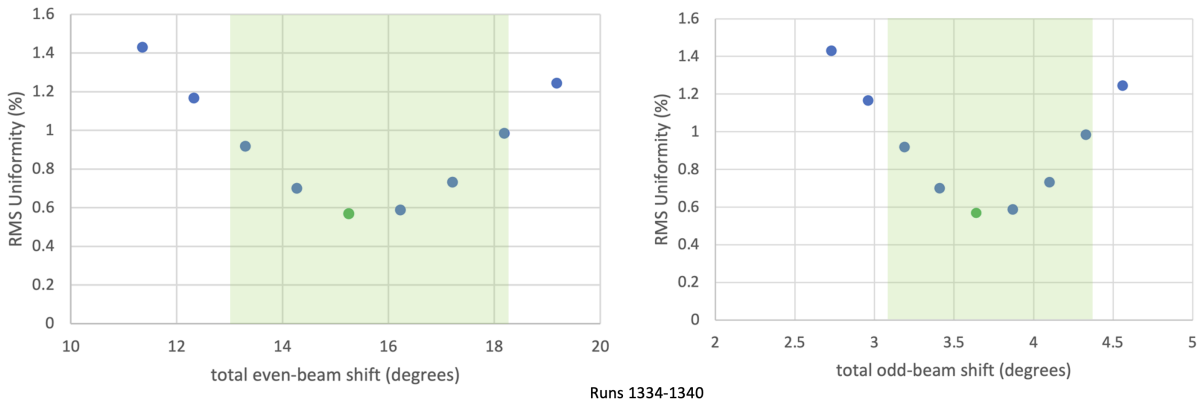

Figure 18: The sensitivity to beam pointing errors for the optimal pointings. The optimum design lies at a relatively robust minimum, with an even-beam shift of 15.25° and an odd-beam shift of 3.64°, displayed as the green point in both graphs.

The design is robust to these changes. As indicated by the green shaded areas, the rms stays below 1% for a range in the total beam shift of 6.5° for even beams and 1.2° for odd beams. It was found that the odd beams require more pointing precision than the even beams. Further runs are required to investigate pointing errors in the orthogonal direction.

3.6 Comparison of the Three Configurations with Flat Beams

Another comparison, though unrealistic, was made between the performance of the three configurations with wide, flat beams, for which the radius was 2500 µm, which is significantly larger than the target radius of 2000 μm. The super-gaussian index was 15. From Fig. 9, the intensity drops off rapidly beyond the radius of the beam, minimizing the loss of target absorption.

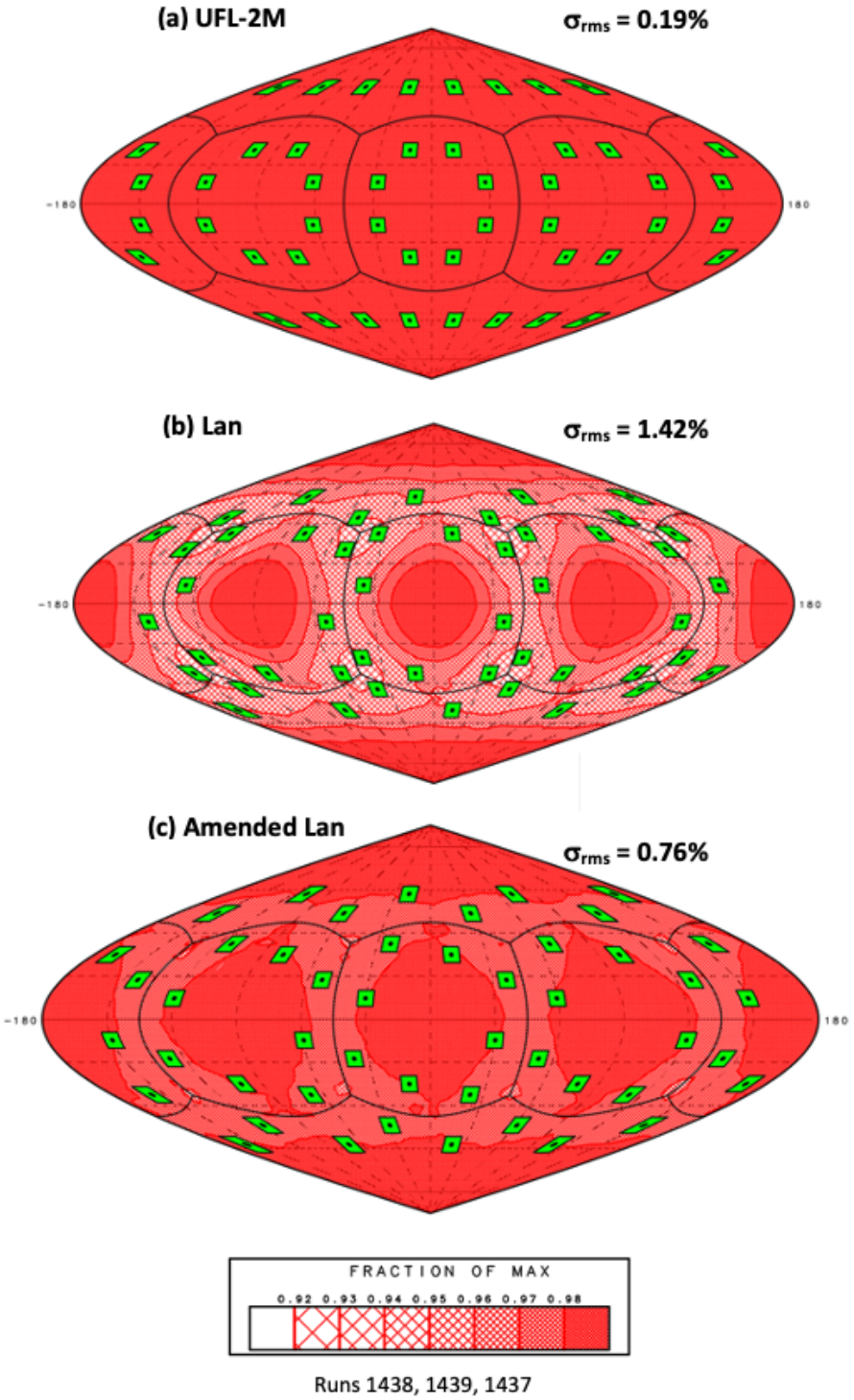

Figure 19: Comparison of the (a) UFL-2M, (b) Lan, and (c) amended Lan configurations with super-gaussian index n of 15, beam r_0 of 2500 µm, and center pointings. The color scale is the same as in Fig. 10 (n = 2.7, r_0 = 1500 µm).

The three plots are all very uniform, with the Lan configuration having the highest nonuniformity of 1.42%, the amended Lan configuration performing slightly better at

0.76%, and the UFL-2M configuration having the lowest nonuniformity of 0.19%. However, as noted in Section 3.1.2, the target absorption decreases significantly with a dramatic increase in radius. Thus, these designs are not viable, because their absorption is only 70%. However, the shots are an interesting exploration of another way to achieve uniformity, and the uniformity comparison confirms that geometrically, the UFL-2M system is the most uniform of the three. In this case, the Lan and amended Lan configurations cannot be compensated by repointing because the beam profiles remain flat.

4 OMEGA Geometry

Simulations with the same target design were also performed for the "stretched soccer ball" geometry used on the Laboratory for Laser Energetics' 60-beam OMEGA laser system. The system's beam ports are arranged on the vertices of a truncated icosahedron, shown in Fig. 20, from [13].

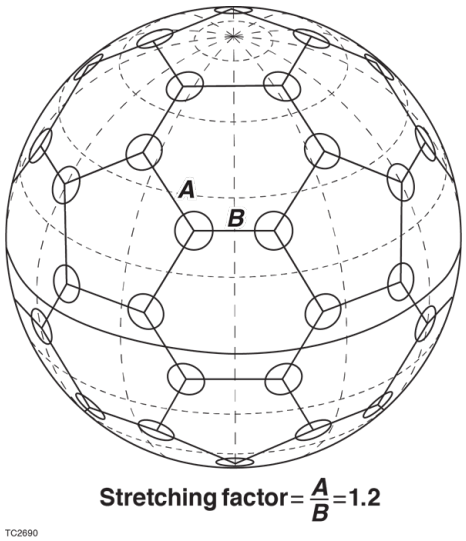

Figure 20: OMEGA laser target chamber geometry. The beam ports are on the vertices of a truncated icosahedron, which has a pattern of pentagons and hexagons.

In an OMEGA-like configuration, there is a stretch factor that goes into the system of ports. This is the ratio of the side lengths of the pentagons and hexagons in the design's geometry, which is $\frac{A}{B}$ in Fig. 20. Normally, the beams in this system are pointed to the center of the target, in which case the aim points on the target also lie on a truncated

icosahedron. In this section, SAGE has been used to model what could have been done if OMEGA had been built unstretched – i.e., specified with a stretching factor of 1.0 – but with the beams repointed to the stretched aim points, which in this work is referred to as a pointing stretch factor. The pointing and port stretch factors for OMEGA are 1.2.

4.1 Comparison Runs with 48–Beam Configuration

The problems used to compare the three 48–beam laser configurations in Sections 3.2 and 3.6 were run for the OMEGA geometry as well, as shown in Fig. 21.

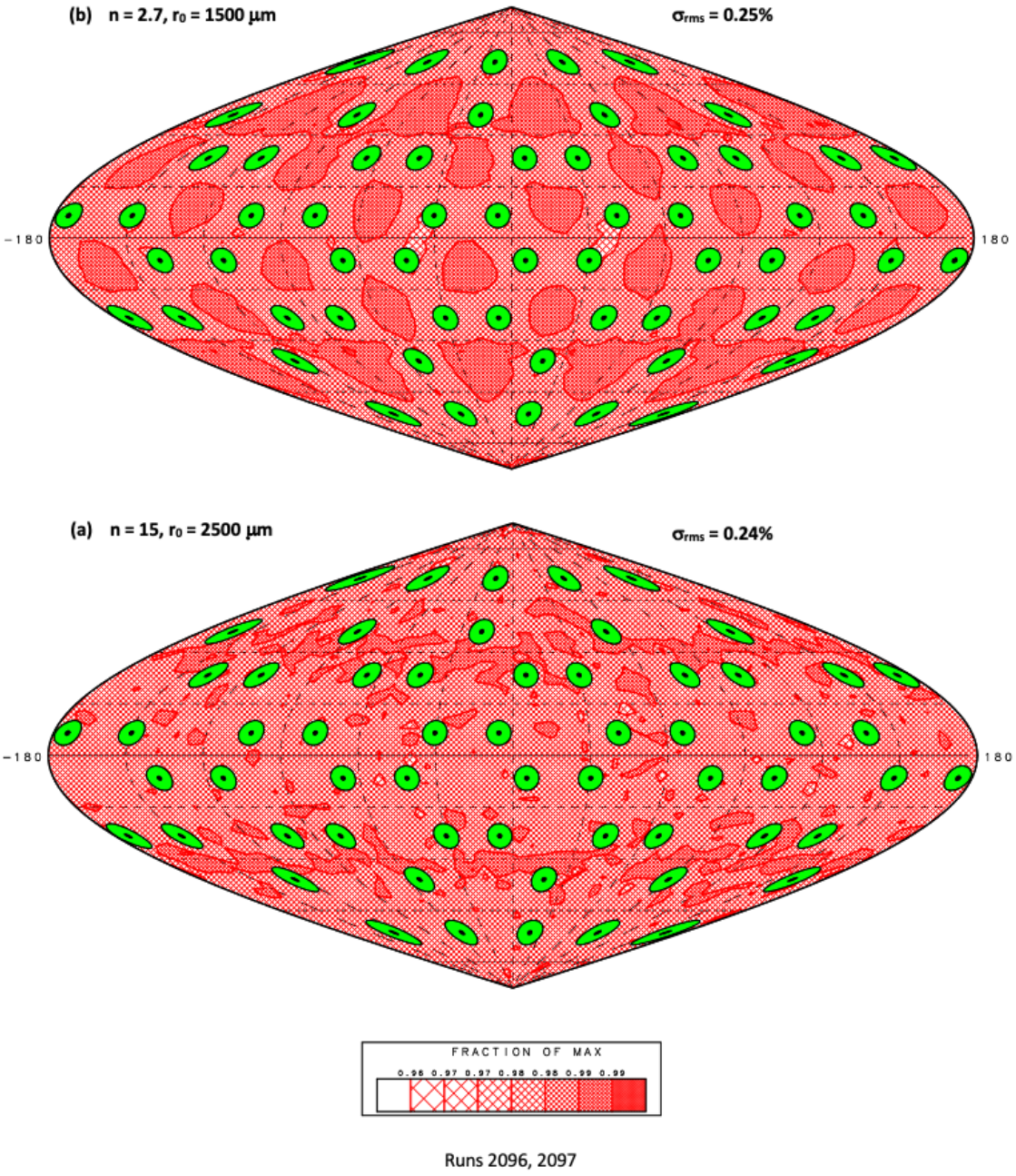

Figure 21: Comparison runs for the OMEGA geometry. (a) is comparable to the runs in Fig. 10 (super-gaussian index $n = 2.7$, $r_0 = 1500$ µm). The OMEGA geometry has the lowest nonuniformity (0.25%, compared with 0.60% for UFL-2M). (b) can be compared to Fig. 19 ($n = 15$, $r_0 = 2500$ µm), with the OMEGA geometry having the second-lowest nonuniformity (0.24%, compared with 0.19% for UFL-2M). Note that identical to the runs in figures 10 and 19, the beams are not repointed.

The OMEGA geometry outperforms all of the 48-beam configurations in the general comparison case (n = 2.7, $r_0 = 1500$ µm), with lower nonuniformity; however, the OMEGA

geometry has a slightly higher nonuniformity than the UFL-2M system in the flat beam simulation. As a 60-beam laser designed for direct drive with its beams evenly distributed around the target chamber, OMEGA does have a distinct advantage for realistic super-gaussian beams, but it is interesting to note that the difference between the systems amounts to only a few tenths of a percentage point of nonuniformity.

4.2 OMEGA Geometry Optimization

The OMEGA laser is normally operated with center pointing, meaning both port and pointing stretch factors are equal. However, SAGE can simulate any combination of stretch factors. This section reexamines the choice of optimum stretching factor for OMEGA by running the 4-mm target design for the OMEGA geometry. First, the port stretch factor was held at a constant value of 1.0 while the pointing stretch factor was varied, shown in Fig. 22.

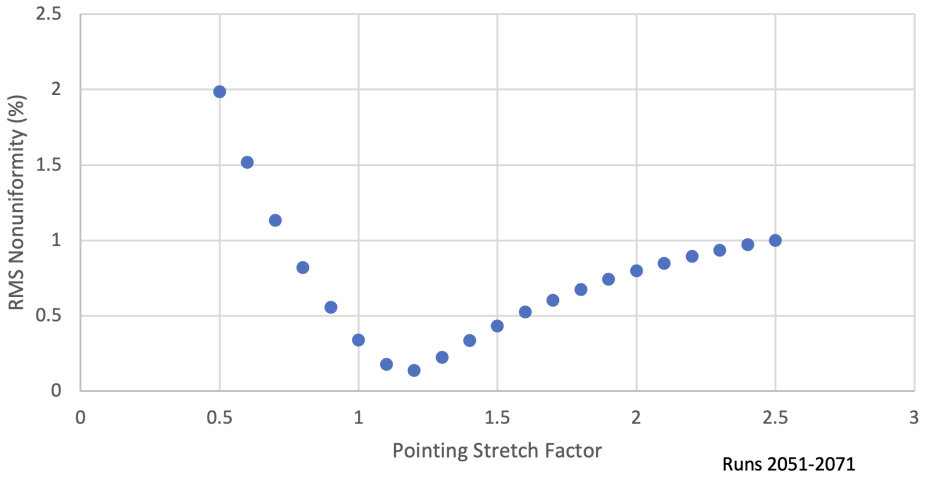

Figure 22: Graph of nonuniformity as a function of pointing stretch factor, with a constant port stretch factor of 1.0, a super-gaussian index of 4.7, and an r_0 of 1700 µm.

The point with the lowest nonuniformity in Fig. 22 is the configuration with the pointing stretch factor of 1.2, with a nonuniformity value of 0.14%. The configuration with port stretch factor of 1.0 and pointing stretch factor of 1.2 would have been optimum if OMEGA had been built with unstretched ports.

Then, the uniformity was tested when both stretch factors were set to the same value,

for a variety of values, as displayed in Fig. 23.

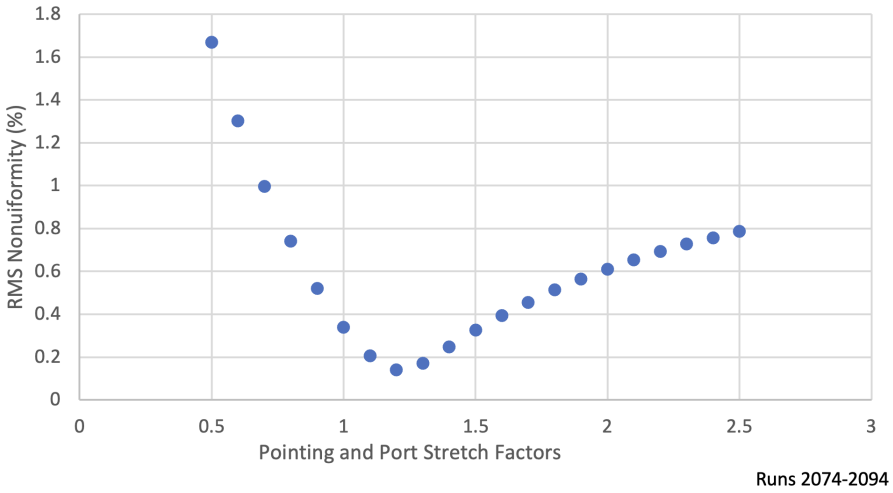

Figure 23: Graph of nonuniformity as a function of simultaneously changing and equal pointing and port stretch factors, with a super-gaussian index of 4.7 and an r_0 of 1700 µm. The minimum σ_{rms} in this graph is 0.17%, which occurs when both stretch factors are 1.2 (i.e., OMEGA as built).

Note that in Fig. 23, the point at stretch factors of 1.2 represents the OMEGA geometry and has the lowest nonuniformity of 0.17%; this value is slightly lower than the value from Fig. 21a (0.25%), for which the super-gaussian index and r_0 were different. These results confirm the rationale behind the choice of OMEGA's geometry; using a completely different target design, the minimum in the σ_{rms} corresponds to the same stretch factor of 1.2. Note that the nonuniformity is lower than for the 48-beam configurations; as mentioned before in Section 4.1, OMEGA was designed for direct drive shots. There is no obvious way the OMEGA geometry can be used for a 60-beam dual direct/indirect drive laser system with favorable angles of incidence to the LEH normals. Although the 48-beam systems have higher nonuniformity for direct drive when compared with the OMEGA geometry, the difference is so small that it may not outweigh the advantages of the 48-beam system.

5 Conclusion

Lan proposed a design for a laser system to be used for indirect drive with an octahedral hohlraum [2], which was then amended by Wang to improve its direct drive capabilities [4]. The 2-D hydrodynamics code SAGE was used to simulate shots on these two laser systems and optimize the pointings and beam spatial profiles. The beams of the amended Lan configuration were repointed to the aim points of the UFL-2M system [5], and then an overshoot was added to optimize. A design was found with a nonuniformity value of 0.57%, comparable to the 0.60% of the UFL-2M system. However, in contrast to UFL-2M, the amended Lan design does not have opposing beams, which may be a design advantage for the system. Pointing scans yielded an approximation of the necessary system pointing accuracy. These results indicate that the amended design will give high caliber spherical direct drive implosions. The OMEGA 60-beam geometry was also investigated, and was found to have only slightly more uniform direct drive results. Thus, if a dual direct drive and indirect drive system is desired, the 48-beam geometry is advocated.

6 Acknowledgements

I would first like to thank Dr. R. Stephen Craxton for directing the high school program and being a patient and insightful advisor. Dr. Craxton was always able to make time to see new results and was an invaluable resource for completing this project. Thank you also to Ms. Truebger for coordinating the finer details. Finally, thank you to the other students for being great company over Zoom.

References

[1] D.E. Hinkel, M.D. Rosen, E.A. Williams, A.B. Langdon, et al. Stimulated Raman scatter analyses of experiments conducted at the National Ignition Facility. *Physics of Plasmas*, 18:056312, 2011.

[2] K. Lan, J. Liu, D. Lai, W. Zheng, and X.-T. He. High flux symmetry of the Spherical Hohlraum with Octahedral 6 LEHs at the hohlraum-to-capsule radius ratio of 5.14. *Physics of Plasmas*, 21(1):010704, 2014.

[3] L. Jing, S. Jiang, L. Kuang, L. Zhang, et al. Preliminary study on a tetrahedral hohlraum with four half-cylindrical cavities for indirectly driven inertial confinement fusion. *Nuclear Fusion*, 57(046020), 2017.

[4] W. Wang. Development of a Beam Configuration for the SG4 Laser to Support both Direct and Indirect Drive. *Laboratory for Laser Energetics*, Summer High School Research Program project report (2019).

[5] V.B. Rozanov, S. Yu. Gus'kov, G.A. Vergunova, N.N. Demchenko, et al. Direct-drive targets for the megajoule facility UFL-2M. *Journal of Physics: Conference Series*, 688:012095, 2016.

[6] N.N. Demchenko, G.V. Dolgoleva, S. Yu. Gus'kov, P.A. Kuchugov, et al. Comparison and analysis of the results of direct-driven targets implosion. *IOP Conference Series: Journal of Phyiscs*, 907:012019, 2017.

[7] N.N. Demchenko, S. Yu. Gus'kov, N.V. Zmitrenko, V.B. Rozanov, and R.V. Stepanov. Uniformity simulation of multiple-beam irradiation of a spherical laser target with the inclusion of radiation absorption and refraction. *Quantum Electronics*, 49:124–132, 2019.

[8] A step closer to thermonuclear synthesis: First module of world's most powerful laser launched in Sarov, Russia, VNIIEF, 2020.

[9] C.B. Yeamans, G.E. Kemp, Z.B. Walters, H.D. Whitley, et al. High yield polar direct drive fusion neutron sources at the National Ignition Facility. *Nuclear Fusion*, 61(046031), 2021.

[10] R. S. Craxton, W. Y. Wang, and E. M. Campbell. A new beam configuration to support both spherical hohlraums and symmetric direct drive. *62nd Annual Meeting of the American Physical Society Division of Plasma Physics*, Nov. 2020.

[11] R. S. Craxton and R. L. McCrory. Hydrodynamics of thermal self-focusing in laser plasmas. *Journal of Applied Physics*, 56(1):108–117, 1984.

[12] A.M. Cok, R.S. Craxton, and P.W. McKenty. Polar-drive designs for optimizing neutron yields on the National Ignition Facility. *Physics of Plasmas*, 15:082705, 2008.

[13] The OMEGA Upgrade - Part II: Preliminary design and target system. *LLE Review*, 39:113–132, 1989.

Development of a Polar-Direct-Drive Design for Large Diameter Beryllium and Plastic Targets on the National Ignition Facility

Tyler Petrillo

Webster Schroeder High School

Advisor: Dr. R. S. Craxton

Laboratory for Laser Energetics

University of Rochester

Rochester, New York

June 2022

1. Abstract

A laser pointing design was developed for future experiments on the National Ignition Facility (NIF). Since the NIF is configured for indirect drive experiments, a method known as polar direct drive repoints the beams away from the center of the target to make direct drive experiments possible. The design was tailored for a beryllium target with a diameter of 4.5 mm, which is slightly larger than the diameter of typical targets imploded on the NIF. The 2D hydrodynamics simulation code SAGE was used to optimize the NIF beam parameters in order to maximize the uniformity of the target's implosion. The pointing design was also found to be optimal for plastic targets of an identical diameter. Additional simulations were carried out for a recent NIF shot in which the plastic target had substantial thickness variations. These simulations indicated that such thickness variations can significantly increase the implosion nonuniformity.

2. Introduction

Nuclear fusion combines two or more atomic nuclei to form a heavier nucleus, releasing a large amount of energy in the process. One method to achieve this reaction uses laser beams to irradiate a small fuel target comprising a shell that is typically filled with deuterium and tritium, two isotopes of hydrogen. The laser beams cause the outside of the shell to ablate outwards and the inside of the shell to compress inwards, bringing the deuterium and tritium to extremely high temperature and pressure. These conditions overcome the Coulomb repulsion forces between the positively charged nuclei, briefly allowing fusion reactions to occur. With ideal conditions, the newly formed helium nucleus would redeposit its energy into the fuel and create a chain of fusion reactions known as ignition. Ignition must occur in order to achieve breakeven, when the energy released by the fusion reactions exceeds the energy input by the laser beams. In order for laser fusion to be considered a viable energy source, however, the energy output must be approximately one hundred times greater than the energy input.

Currently, there are two different approaches to laser fusion: direct drive[1] and indirect drive.[2] In direct drive, as illustrated by Figure 1(a), laser beams are directly aimed at the target and the target is irradiated at normal incidence at all angles. The OMEGA laser system at the University of Rochester's Laboratory for Laser Energetics is configured for direct drive. This approach typically results in less uniform irradiation of the target than indirect drive. In indirect drive, as illustrated by Figure 1(b), the target is placed inside a cylindrical hohlraum, usually made of a metal with a high atomic number, such as gold. The beams enter through openings in the top and bottom of the hohlraum and hit the inner walls, which emit x rays that spread over a large part of the target's surface, uniformly irradiating the target. Despite the better uniformity of implosion offered by indirect drive, the target only absorbs about 20% of the laser energy.

Roughly 80% of the laser's energy is absorbed by the walls of the hohlraum or lost through the openings in the hohlraum. However, the increased uniformity of implosion and the large energy available at the National Ignition Facility (NIF) have enabled indirect drive to outperform direct drive to date. The NIF is currently configured for indirect drive.

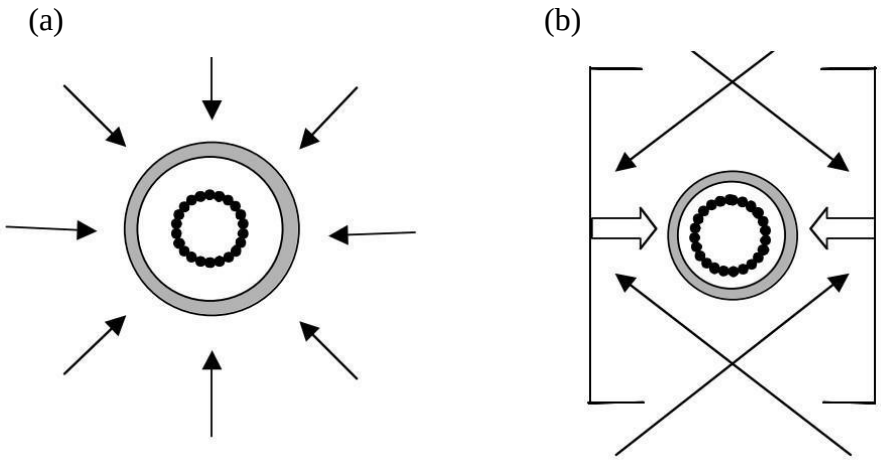

Figure 1. The two main approaches to inertial confinement fusion. (a) In direct drive, the laser beams directly hit the target and irradiate it. (b) In indirect drive, the beams enter a hohlraum, which emits x rays (represented by the clear arrows) that irradiate the target. [From Ref. 3]

The NIF's current configuration is not ideal for direct drive experiments. The NIF consists of 192 beams, divided amongst 48 quads of 4 beams each, located in 4 rings in each hemisphere at angles of 23.5°, 30.0°, 44.5°, and 50.0° from the vertical. If the NIF's beams were aimed at the center of the target, the energy deposited would not be evenly distributed over the target's surface. As shown in Figure 2(a), the poles compress much more than the equator. Therefore, in order to achieve a more uniform implosion, the drive on the equator must be increased to match the poles. A method called polar direct drive repoints the beams toward the equator, resulting in an increase in uniformity [Figure 2(b)].

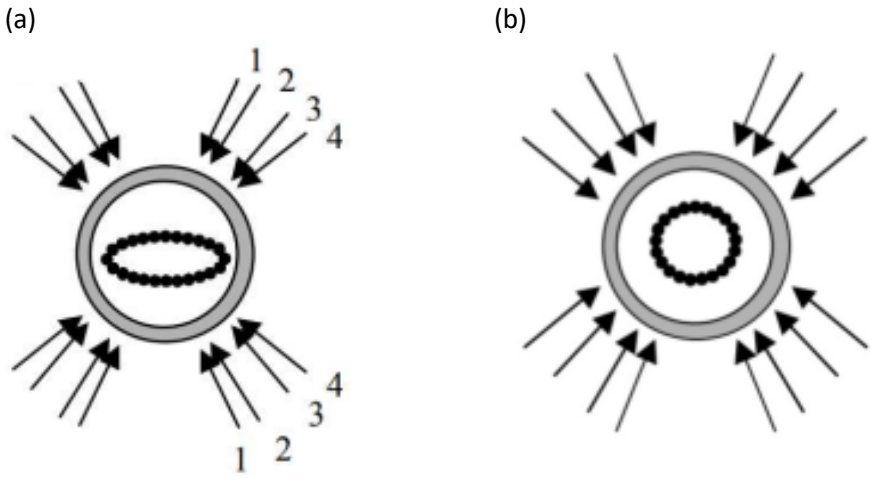

Figure 2. Two ways in which the NIF can be used to carry out direct drive experiments. (a) If the beams are fired towards the center of the target, the target's equator is undercompressed relative to its poles. Rings 1-4 are indicated. (b) Using polar direct drive, the target implodes much more uniformly. [From Ref. 3]

Depending on the size of the target being imploded, the NIF's beam parameters need to be adjusted in order to optimize the uniformity of the target's implosion. For a proposed beryllium target, which is 4.5 mm in diameter, using the optimized pointings designed for a smaller target would result in undercompression at the equator, leading to less overall uniformity. Developing a pointing design specific to this size target is essential for maximizing its uniformity as it implodes. This work assumes the use of the NIF's current set of phase plates, optics which spread the energy of the laser beam to produce a more uniform beam after focusing, and optimizes other key NIF beam parameters. One of such parameters is the defocus on each ring of beams. By moving the focus lens toward the target (defocusing the beam), the size of the beam spot created on the target increases while the intensity of the spot decreases. Each ring of beams can also be shifted away from the center of the target in both the θ and ϕ directions. The polar angle, θ, increases from 0° at the chamber top to 180° at its bottom. The azimuthal angle, ϕ, ranges from 0 to 360° anticlockwise, when viewed from the chamber top. Each beam can be

shifted to a specific angle in the θ direction, while each of the beams in a ring can be spread out horizontally in the ϕ direction.

The primary goal of this work was to create a set of pointings which maximized the implosion uniformity of the proposed 4.5 mm beryllium target (Section 3). This design was also found to be suitable for plastic targets of similar size (Section 4). The report also explores how thickness variations in a target's surface, modeled by Legendre polynomials, can significantly impact uniformity as the target implodes (Section 5).

3. Optimized Design

The optimized design was intended to maximize the uniformity of the target's implosion right before fusion reactions occur. The target is a shell of 15 μm of beryllium (Be) with a diameter of 4.46 mm. The laser pulse used on this target is shown in Figure 3. The laser pulse delivers 1.6 MJ with a linear rise to 427 TW at 1.7 ns and a linear fall from 4.5 ns to 4.7 ns. The optimized design was largely based on a previous design (Orange[4]) that was optimized for targets of 4 mm in diameter.

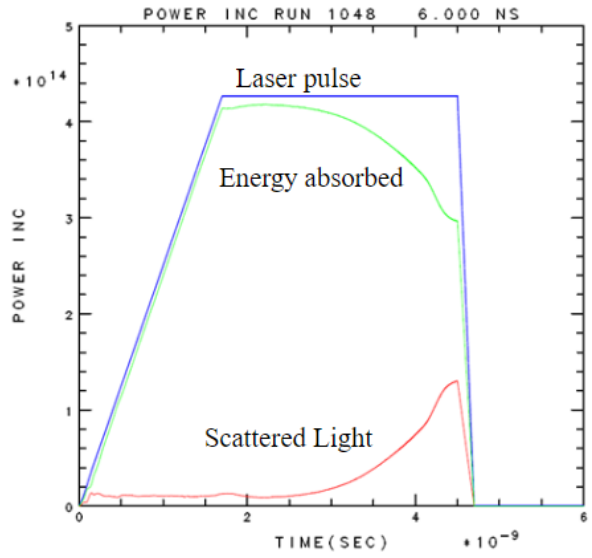

Figure 3. Power vs. time graph of the optimized design showing the incident laser pulse, energy absorbed, and transmitted power in W.

The implosion of the shell and the incoming rays from a Ring 4 beam are shown in Figure 4. The figure shows a raytrace plot of the optimized design at 3 ns. The heavy outer semicircle at a radius of 2.23 mm represents the target's initial position before it was hit by the laser pulse, while the inner heavy semicircle illustrates how far the shell has moved through 3 ns. The rays near normal incidence have had their energy almost completely absorbed by the target.

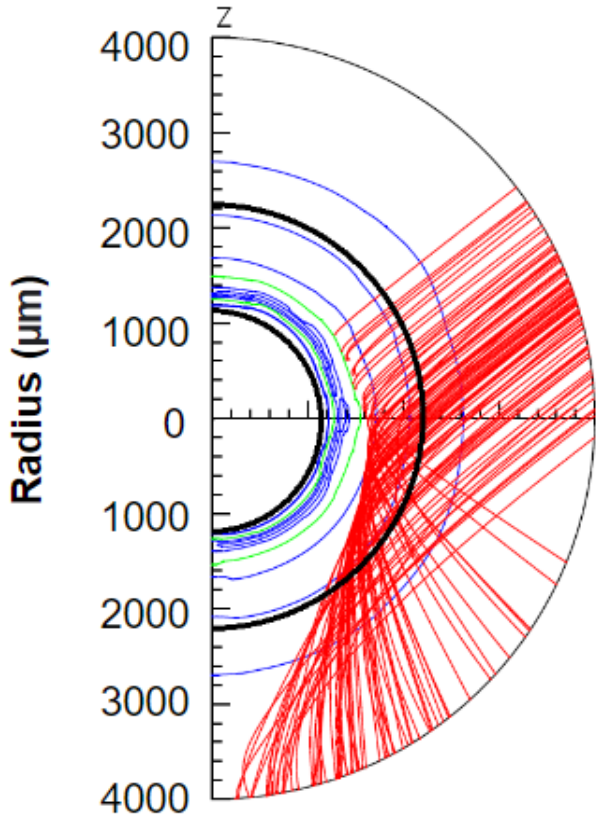

Figure 4. Raytrace of the bottom-right beam of Ring 4 at 3 ns of the optimized design. Electron density contours are shown by the blue circular lines, which show increasing density as the blue semicircles decrease in radius. The green lines represent the critical density, the density beyond which laser light cannot propagate. The vertical axis measures distances in μm. [Run 1048]

The imploding shell in Figure 4 appears very uniform. To examine this more closely, the center of mass radius of the imploding shell is plotted as a function of angle θ from the z axis in Figure 5. The figure shows the optimized design and the Orange target design on the 4.46 mm Be target at 3 ns. Like Figure 4, the figure comes from a 2D calculation and therefore represents averages over the azimuthal angle ϕ. At 3 ns, the target is around 1450 μm away from its center. The overall velocity nonuniformity of the optimized design in the θ direction improved over the Orange design by nearly two fold (see Sec. 3.2).

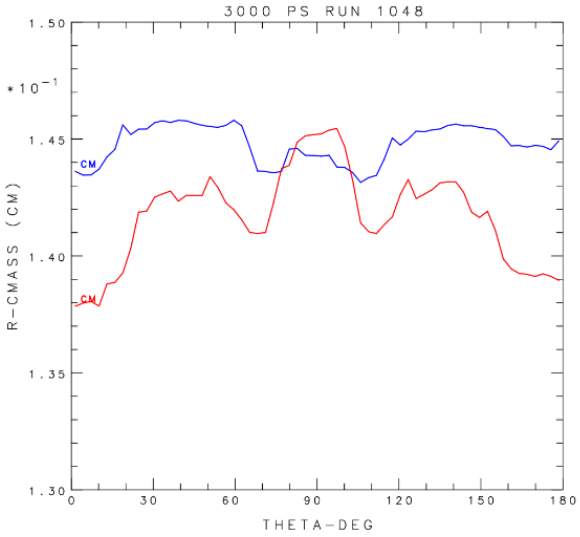

Figure 5. Center-of-mass radius (cm) vs. θ (degrees) at 3.0 ns of the optimized design (in blue) and the Orange target design (in red) for a 4.5 mm diameter target. [Runs 1002, 1048]

Figure 6 shows the 3D center-of-mass contour plot at 3 ns using the optimized design. It comes from taking the azimuthal average from Figure 5, and adding the azimuthal variations using the 3D deposition pattern of laser energy [following Ref. 4]. The overall velocity nonuniformity (see Sec 3.2) is just 1.65%.

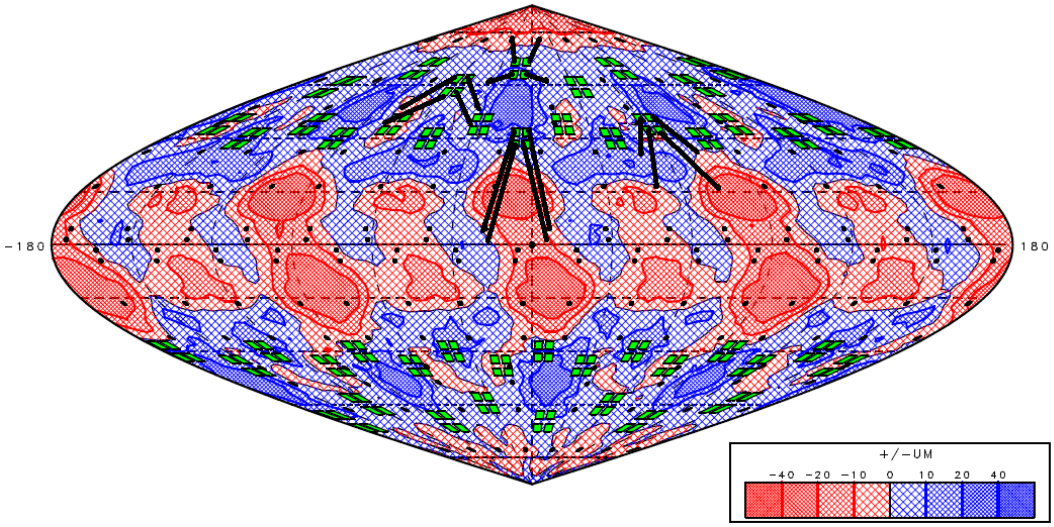

Figure 6. The 3D center-of-mass plot of the optimized design at 3 ns with contours indicating deviations from the average radius of the beryllium shell in μm. Red regions represent overcompression and blue regions indicate undercompression. The green squares represent the four beams in each quad and the black dots represent where each beam has been repointed to. The black lines show how the laser beams in four representative quads are repointed to maximize uniformity. [Run 1048]

3.1 Pointings and Defocusing

The pointings in the θ and ϕ directions and defocus distances for the previous (Orange) and optimized designs are shown in Table 1. The optimized pointings in both the θ direction and the ϕ direction have been adjusted in order to maximize uniformity. The left beams of each quad are moved Δϕ to the left and the right beams are moved Δϕ to the right relative to the center of each quad. There are no pointings in any of the 4 rings on the NIF that were shifted more than 5° compared to the previous design.

	Orange Design θ	Orange Design Δϕ	Orange Defocus (cm)	Optimized Design θ	Optimized Design Δϕ	Optimized Defocus (cm)
Ring 1 top beams	13˚	22.5	2.5	13˚	22.5	3.25
Ring 1 bottom beams	24˚	22.5	2.5	28˚	22.5	3.25
Ring 2 top beams	38˚	22.5	2.0	38˚	22.5	3.00
Ring 2 bottom beams	46˚	22.5	2.0	44˚	22.5	3.00
Ring 3 top beams	53˚	11.25	2.0	55˚	12.5	3.00
Ring 3 bottom beams	71˚	11.25	2.0	68˚	12.5	3.00
Ring 4 top beams	79˚	11.25	2.0	84˚	12.0	3.00
Ring 4 bottom beams	88˚	15.0	2.0	88˚	11.0	3.00

Table 1: Beam parameter specifications for all 4 Rings of the Orange and optimized designs. All the optimized pointings changed very little from the previous design. The most significant changes were shifting the Ring 4 top beams in order to increase drive on the equator and increasing the defocus to reduce azimuthal nonuniformity for the larger target.

The Orange design resulted in undercompression at the equator on the larger 4.46 mm Be target (see Fig. 5). To increase the drive on the equator, the ring 4 top beams were shifted from 79˚ to 84˚. Consequently, the drive away from the equator ($\theta \approx 60^\circ$) was reduced. To compensate for this change, the ring 3 bottom beams were shifted from 71˚ to 68˚. The changes made to the other beams in the θ direction slightly improved azimuthal uniformity. Changes made in the ϕ direction were less significant than in the θ direction. Only the pointings of Rings 3 and 4 were shifted to increase uniformity. The Orange design set ring 3 and the top of ring 4 beams to 11.25˚ in order to maintain uniformly distributed energy in the ϕ direction. However, the optimized design set ring 3 beams to 12.5˚ and the top of ring 4 beams to 12˚, which resulted in a slightly higher uniformity in the ϕ direction. Overall, any changes made in the ϕ direction had a minimal impact on the overall uniformity of the target's implosion. The optimized design also set the Δϕ of the ring 4 bottom beams to 11˚.

Defocusing is used to change the size of each beam spot of the laser. This is done by moving the focus lens toward the target. Since the proposed 4.46 mm Be target is slightly larger than the 4 mm targets that the Orange pointings were tailored for, the defocus of each beam had to be increased in order to reduce nonuniformity in the azimuthal direction. The defocus for rings 2, 3, and 4 was set to 3 cm, while the defocus for ring 1 beams was set to 3.25 cm. This is a significant increase over the Orange design, which had a maximum defocus of 2.5 cm for any given ring. The maximum allowed defocus using the NIF's current phase plates is roughly 3.5 cm, which makes it difficult to optimize larger targets than 4.5 mm in diameter.

3.2 Improved Uniformity

The optimized design maintained a high absorption of beam energy across the target's surface. Although a large portion of the rays are deflected in Figure 4, they still deposit a large amount of their energy into the target. Averaged over the entire laser pulse, the target has an overall energy absorption of 91.3%, which is slightly less than the 94.1% energy absorption when using the Orange target design.

The optimized design, as shown in Figures 4 and 5, produced a high degree of uniformity in the θ direction, allowing the equator to compress uniformly at the same rate as the poles. The optimized design produced a root-mean-square (rms) variation in center of mass radius, relative to the average radius, of 0.58% through 3 ns. Another useful quantity for evaluating the uniformity of a target's implosion is the rms nonuniformity of the average velocity (Δv-rms), which is calculated by dividing the rms of deviations in the center of mass radius by the distance that the target has traveled. At 3 ns, the target has moved an average of 776 μm and the rms deviation in the distance moved is just 8.4 μm, leading to a Δv-rms of 1.08% (Figure 5) in the θ direction. The optimized design has shown substantial improvement over the Orange target design (Δv-rms = 2.06%) by reducing overall nonuniformity on the proposed target by nearly a factor of two. The changes made to the pointing and defocusing (Section 3.1) significantly strengthened the equator, as evident by the red regions between θ=70˚ and θ=110˚ in Figure 6. Additionally, there are no places on the target that deviate from the average radius of the beryllium shell by more than ±40 μm.

The relationship between the components of velocity nonuniformity in the θ and ϕ directions is given by the equation

$$(\Delta v - rms)^2 = (\Delta v - rms(\theta))^2 + (\Delta v - rms(\phi))^2 \quad (1)$$

where Δv-rms is the total nonuniformity, Δv-rms(θ) is the nonuniformity in the θ direction, and Δv-rms(ϕ) is the nonuniformity in the ϕ direction. The optimized design has an overall Δv-rms of 1.65% at 3 ns. Knowing the Δv-rms(θ), Equation 1 can be used to calculate the Δv-rms(ϕ). The optimized design has a Δv-rms(ϕ) of 1.25%, which is slightly higher than the 1.08% Δv-rms(θ) nonuniformity. The overall Δv-rms is nearly a two-fold improvement over the Orange target design for which the Δv-rms is 3.06%.

3.3 Ideal Laser Pulse and Thickness

The optimized design was intended for a laser pulse that delivered 1.6 MJ of energy. The proposed Be target was observed to have imploded before the end of the laser pulse, wasting energy in the process. The duration of the laser pulse can be shortened in order to save energy. Alternatively, the extra energy can be used to implode a slightly thicker target, which would also increase the total amount of energy absorbed by the target.

Figure 7 illustrates the implementation of a shorter laser pulse on the proposed target. The laser pulse depicted in Figure 7 is identical to the original 1.6 MJ laser pulse (Figure 3), except that the laser experiences an earlier linear fall from 4.0 to 4.2 ns. Using the shortened laser pulse in Figure 7, the target now has a higher energy absorption of 94.9%. Since the bang time, the time at which fusion reactions occur, is estimated to occur at roughly 4.0 ns, this change in the duration of the laser pulse is unlikely to have any effect on the neutron (energy) yield.

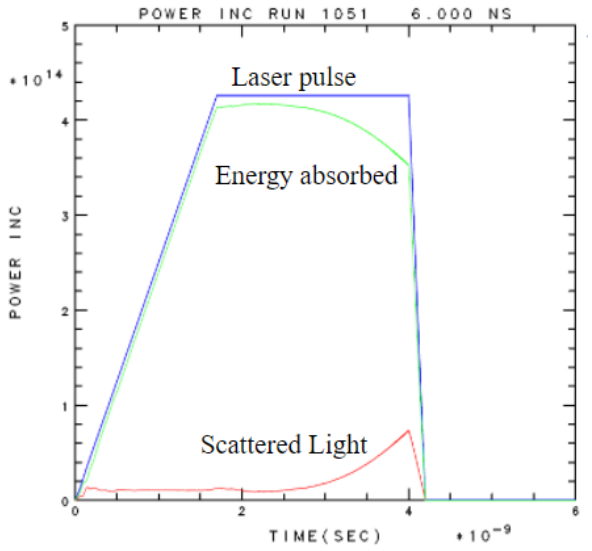

Figure 7. Power vs. time graph for the optimized design using the modified 1.3 MJ laser pulse, which experiences an earlier linear fall from 4.0 to 4.2 ns. The shorter laser pulse increased the percentage of energy absorbed by the target from 91.3% (Figure 3) to 94.9%.

A target with a thicker shell can be used to slow the rate at which the target implodes. Figure 8 depicts the power vs. time graph of a 20 μm beryllium target, which is 5 μm thicker than the proposed beryllium target used in Figure 3. The additional beryllium causes the target to implode slower than the proposed target. The bang time can be approximated to between 4.5 and 5 ns, which is at roughly the same time that the laser powers off. The overall energy absorption is 95.8%. Increasing the thickness of the shell enables higher energy absorption without the need to reduce the duration of the laser pulse. Although this simulation used the Orange design, the same result would be expected for the optimized design.

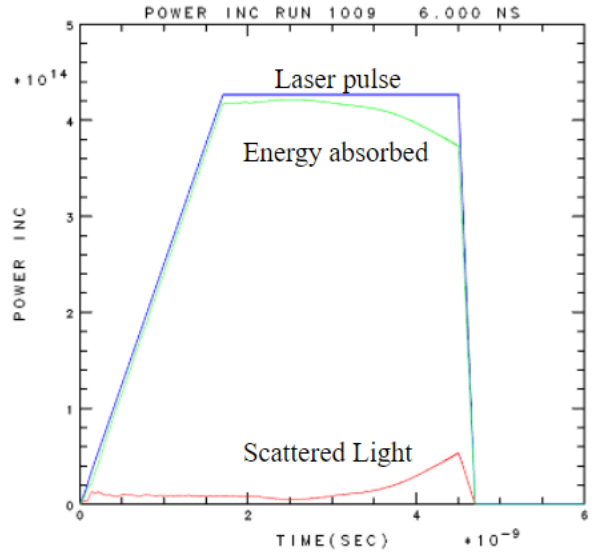

Figure 8. Power vs. time graph for a 20 µm Be target using the Orange design and a 1.6 MJ laser pulse. The overall energy absorption is 95.8%.

4. Optimized Design for Plastic Targets

Targets designed for inertial confinement fusion are made out of a variety of materials. A common material for these targets is plastic (CH), which has a density of 1.044 g/cm^3. CH has a noticeably lower density than beryllium (Be), which has a density of 1.85 g/cm^3 and is also the material that the optimized design was created for. A plastic target will compress faster than a beryllium target of the same thickness.

Figure 9 compares the uniformity of the proposed Be target (15 µm in thickness) to two CH targets of differing thicknesses. Through 3.0 ns, the 21 µm CH target (blue line) has a Δv-rms of 1.08% in the θ direction, which is identical to that of the 15 µm Be target that the pointings were optimized for. Similarly, the 27 µm CH target, which has not moved as far as the other 2 targets through 3.0 ns, produced a Δv-rms of 1.51% in the θ direction. The similar uniformity performance for both CH thicknesses suggests that the optimized design suits CH as well as Be.

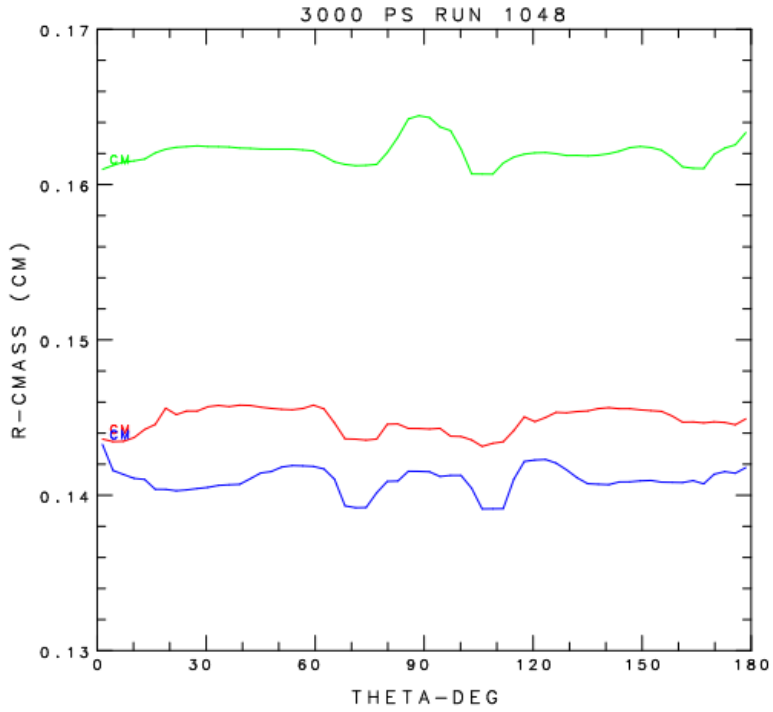

Figure 9. Center-of-mass radius (cm) vs. θ (degrees) at 3.0 ns for three targets of diameter 4.5 mm using the optimized pointing design. The red line is identical to the blue line from Figure 5, allowing for the different scale on the y-axis. The green and blue lines represent CH targets with thicknesses of 27 µm and 21 µm, respectively [Runs 1048, 1055, 1061]

The equivalent mass for 15 µm of Be is 23.7 µm of CH. However, the 15 µm Be target and 21 µm CH target have moved approximately the same distance through 3.0 ns, and are currently both 0.14 cm from their centers. This would suggest that a mass equivalent CH target (23.7 µm) would move slower than the Be target, and that CH compresses slower than Be.

For a plastic target to make use of the entire 1.6 MJ laser pulse, an ideal thickness must be found. The power vs. time graph in Figure 10 illustrates the 1.6 MJ laser pulse on a CH target that is 30 µm thick. The target absorbed 94.8% of the total laser energy and had an estimated bang time between 4.5 ns and 5.0 ns. Laser energy that is used after fusion reactions occur does not contribute to the energy (neutron) yield, and also has the potential to damage laser optics. By selecting a CH thickness of 30 µm, the laser will turn off roughly at the time of the bang, thus minimizing energy loss.

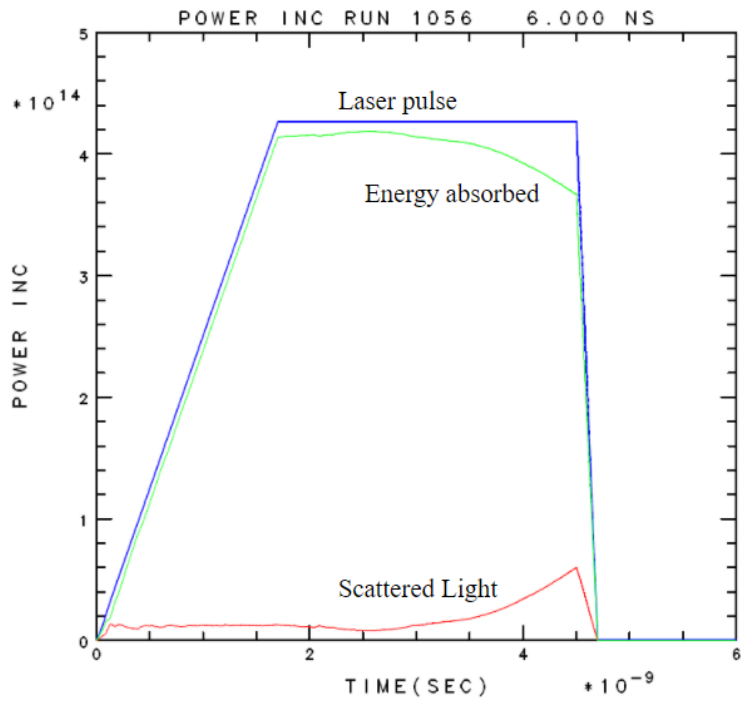

Figure 10. Power vs. time graph for a 30 µm thick CH target using the optimized pointing design. The laser pulse contains a total of 1.6 MJ of energy and has a duration of 4.7 ns. The laser pulse peaks at roughly 430 TW of power. [Run 1056]

5. Thickness Variations

In a recent polar direct drive experiment on the NIF (N210627-001), a plastic (CH) target with a radius of 4.3 mm was observed to have a thickness that varied between 19.8 µm and 28.1 µm, which amounts to an 8.3 µm difference in thickness. Errors in target thickness are certainly decreasing the target's uniformity as it implodes, but the degree to which this particular target's uniformity was affected remains unknown.

5.1 Modeling Thickness Errors

One way that thickness variations can be modeled is through the use of Legendre polynomials, which are a system of complete and orthogonal polynomials. The first five Legendre polynomials, which have been reparametrized in terms of angles, are shown in Figure 11. Each polynomial is graphed from 0 to 180˚ to represent the θ direction across a target's surface.

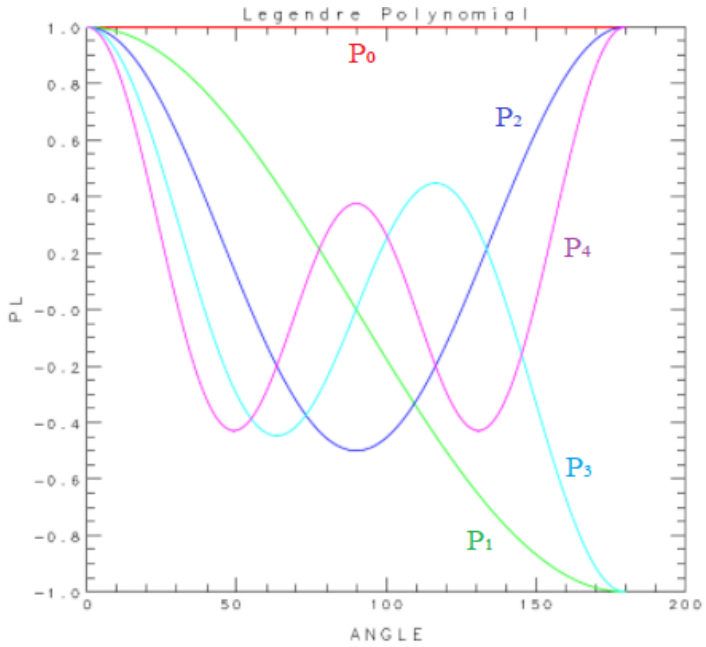

Figure 11. The first five Legendre polynomials P_n (up to n = 4) from 0 to 180 degrees are labeled on the left. Each polynomial ranges from -1 to 1 along the vertical axis, which has dimensionless units. Each graph illustrates how a thickness variation can be distributed across a target's surface.

5.2 Analyzing Thickness Variations

Several 2-D hydrodynamic simulations were run using the code SAGE that applied Legendre polynomial variations to a plastic target. Each simulation used a target with a diameter of 4.3 mm (the same as shot N210627-001) and an average thickness of 25 μm, creating plots with 2 μm (25 ± 1 μm) and 8 μm (25 ± 4 μm) thickness differences.

In the simulations of the 4.3 mm plastic target that contained Legendre polynomial variations, an increase in nonuniformity was evident. After applying P_3 Legendre polynomial variations to the plastic target, Figure 12 (a) indicates that a 2 μm difference produces noticeable nonuniformities. At 0˚ in the θ direction, the innermost density contour is roughly 800 μm away from the target center. At the opposite pole (θ = 180˚), the contour is only 600 μm away from the center.

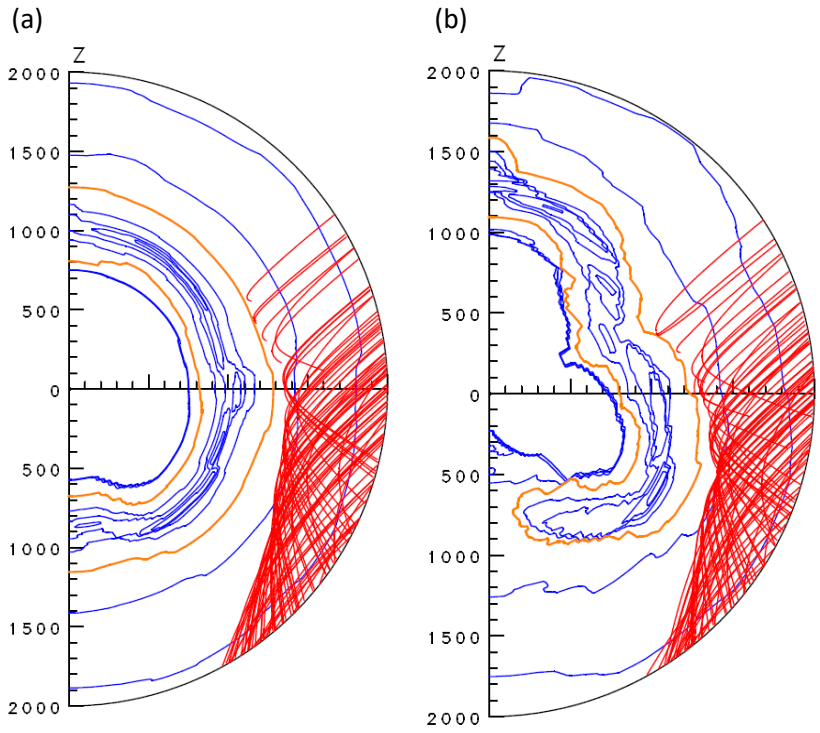

Figure 12. Raytrace plots of P_3 Legendre polynomial variations applied to a 2 µm difference (a) and an 8 µm difference (b) at 3.5 ns. The density contours in (a) reveal some nonuniformity, while the nonuniformities in (b) are more pronounced. [Runs 1043, 1037]

As expected, the target with an 8 µm variation in its thickness was significantly less uniform than its 2 µm variation counterpart. In Figure 12 (b), the target has compressed more unevenly, as evident by its behavior at the poles. At 0˚, the innermost contour is 1000 µm away from the center. Conversely, the opposite pole is close to 200 µm away from the center. Other regions of the target are also significantly nonuniform. The target is significantly overcompressed around 60˚ from the vertical, but undercompressed at roughly 120˚ from the vertical. Such distortion can be expected to significantly lower the neutron yield.

Simulations that applied other Legendre polynomial modes yielded similar results. After applying P_2 Legendre polynomial variations to the plastic target, Figure 13 shows a plot of the center-of-mass radius vs. θ that compares a target with no thickness variations to two targets that contained 2 µm and 8 µm thickness variations. Through 3.0 ns, the plastic target with no thickness variations has a Δv-rms of 1.59% in the θ direction, while the 2 µm target has a Δv-rms

of 2.37%. The 8 µm difference target has an exceptionally high Δv-rms of 11.11% in the θ direction.

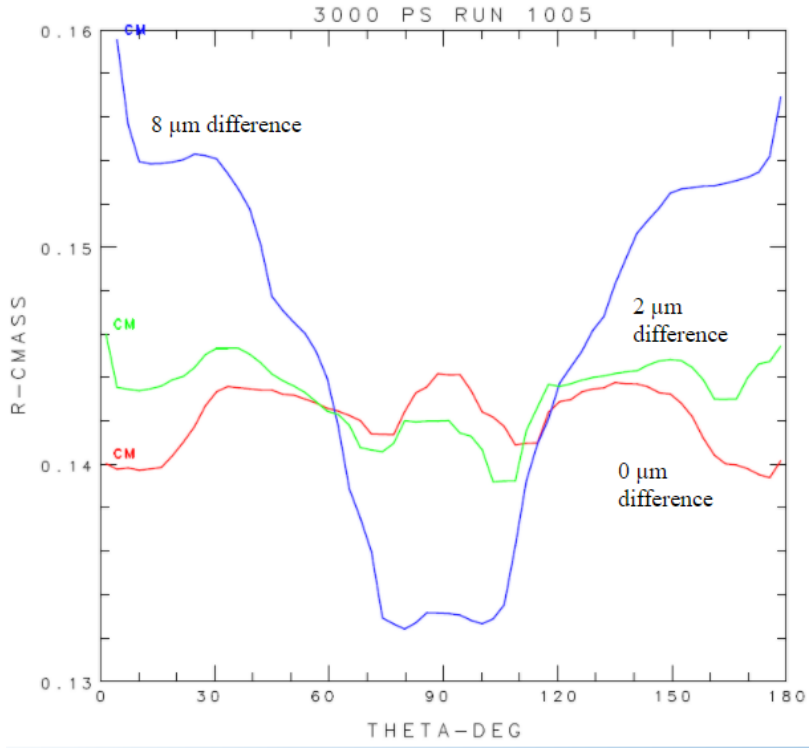

Figure 13. Center-of-mass radius (cm) vs. θ (degrees) at 3.0 ns for three different thickness variations with applied P_2 Legendre polynomials. The 0 µm, 2 µm, and 8 µm differences are represented by the red, green, and blue lines, respectively. [Runs 1005, 1023, 1042]

The target with a 2 µm difference saw less than a 1% increase in its Δv-rms nonuniformity compared with the target with no thickness variations, suggesting that small variations in thickness do not have a significant impact on the overall uniformity. However, the target with an 8 µm difference experienced a 9.52% increase in its nonuniformity, which resulted in significant distortion of the target's surface. Due to the nature of the Legendre polynomial used, the target's surface resembles a parabola, as shown by the blue line in Figure 13. The behavior of the 8 µm difference target shows how easily thickness variations can be amplified as the target implodes. Therefore, in order to maintain a high level of uniformity, a target's variations in thickness need to be as minimal as possible.

6. Conclusion

An optimized design was developed to maximize uniformity for a Be target that is 4.5 mm in diameter. By increasing the defocus of each beam and making slight changes to the pointings in both the θ and ϕ directions, the overall uniformity improved by nearly two-fold over a previous design. The optimized design produced similar improvements on CH targets, making the design suitable for targets of both materials. An ideal shell thickness and laser pulse duration were found to maintain low nonuniformity and improve energy absorption. Variations greater than 2 μm in a target shell's thickness had a significant impact on uniformity, posing a need to limit these variations.

7. Acknowledgements

I would like to thank my family for their unwavering support throughout the program. I'd also like to thank my high school math and science teachers for encouraging me to continue my pursuit of knowledge. Lastly, I'd like to thank my advisor Dr. R.S. Craxton for his help and flexibility, and for providing me this amazing opportunity.

8. References

1. J. Nuckolls, et al., "Laser Compression of Matter to Super-High Densities: Thermonuclear (CTR) Applications," Nature **239**, 139 (1972).

2. J.D. Lindl, "Development of the Indirect-Drive Approach to Inertial Confinement Fusion and the Target Physics Basis for Ignition and Gain," Phys. Plasmas **2**, 3933 (1995).

3. A. M. Cok, "Development of Polar Direct Drive Designs for Initial NIF Targets," Laboratory for Laser Energetics High School Research Program (2006).

4. C.B. Yeamans, et al., "High yield polar direct drive fusion neutron sources at the National Ignition Facility," Nucl. Fusion **61** 046031 (2021).

Data Services to Improve Access to Scientific Image Data

Leo Sciortino
School of the Arts
Rochester, New York

Advisor: Richard Kidder

University of Rochester Laboratory for Laser Energetics

December 2023

1. Abstract

An investigation of methods to access image data stored from experimental campaigns was conducted. The study found that there are several image data formats that have been historically used by LLE. Images are currently stored on LLE file servers, with files indexed through LLE's relational Oracle database. This investigation explored technologies to provide easy and secure access to image data, minimizing the need for direct database and file system interactions by the user. The project focused on image parsing, storage, and retrieval mechanisms for multiple formats including HDF4, HDF5, TIFF, and JSON (JavaScript Object Notation). Services to provide data processing (e.g., background subtraction) were also investigated. Project software was tested using Python, NodeJS, PL/SQL, and an Oracle database. Overall, the research found that using Python and its associated libraries in conjunction with web services is a viable option for presenting and processing image data.

2. Introduction

HDF **(**Hierarchical Data Format) file format is a type of file that is typically used to store scientific data. At the Laboratory for Laser Energetics (LLE) an HDF file will typically store an image and its corresponding attributes. Currently most HDF files at LLE are stored in HDF4[1] format, which is outdated for most applications compared to its successor HDF5.[2]

This investigation looked to improve the current pipeline that principal investigators (PIs) use to retrieve image data from experiments on the OMEGA and OMEGA EP laser systems. It was found that there are two methods that PIs use to access image data from OMEGA archives,

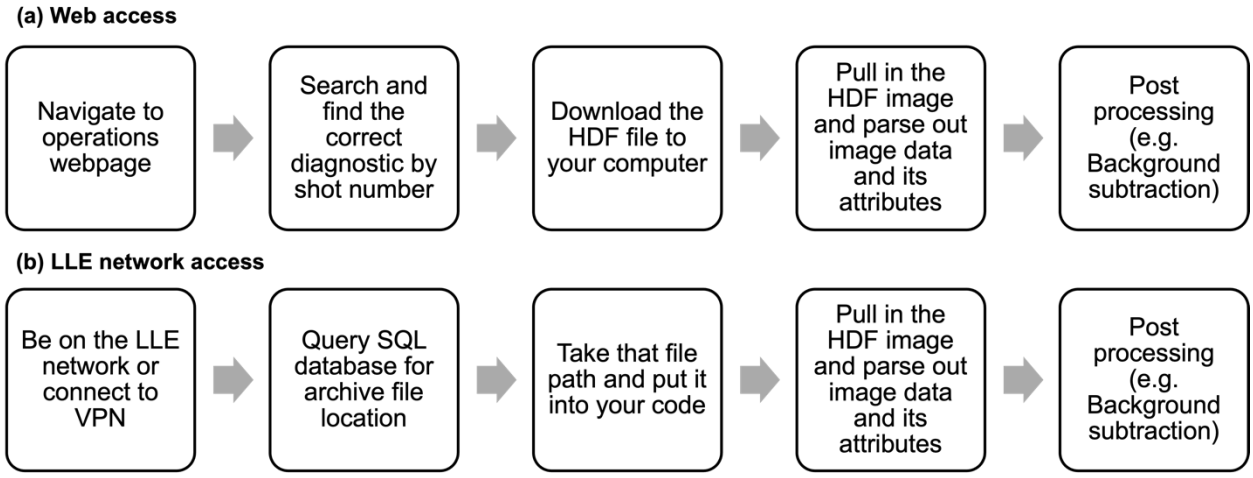

Fig. 1 Two ways PIs can retrieve images and their corresponding data. Both are slow and cumbersome.

both of which were reviewed for process improvement (Fig. 1). The first method (Fig. 1(a)) uses web access, which doesn't require PIs to be on the LLE network but uses traditional early 2000s web access technology through the OMEGA Shot Images and Reports page (Fig. 2). These pages require user interaction to locate and download data, making data retrieval slow and cumbersome.

These webpages are also difficult for LLE to maintain. They use outdated programming practices such as inline SQL (structured query language) database calls, and inline called shell scripts. This can easily introduce data security problems through SQL injection where a user can add to the end of a SQL query compromising the security of the database. Additionally, these webpages are written in PERL, which has become less popular for modern web development. Poor documentation of this code also hinders its further development. For a developer to modify these scripts one must spend hours searching through dozens of files.

The process to access data was found to be problematic as the user must navigate to the correct shot number and then find the diagnostic and download the image onto their computer. PIs also have an option to download the data package that contains all or part of the relevant image data for that shot. Since multiple users work on these campaigns it is likely that these images are copied an unnecessary number of times. After the PI obtains the image data they can open the data for processing.

OMEGA Shot Images and Reports

Query Page
Omega Home Page

Multiple Query:

For Shot_Number 104486 **to** 104486 **go to** General_Summary Query Advanced Search

General Shot Summary
for Shots 104477 - 104486

Color Legend

System Shot	Trigger Tests	System Aborts

Previous 20 Shots -->

Shot	Date	Shot Type	RID	Campaign	Target ID(s)	EEAF	# of PCUs	
104486	06-Jun-2022 09:33:47	A-Splitter					2	Download Images
104485	06-Jun-2022 09:18:41	Non-Prop					0	Download Images
104484	06-Jun-2022 09:13:13	A-Splitter					2	Download Images
104483	06-Jun-2022 08:42:43	A-Splitter					2	Download Images
104482	06-Jun-2022 08:30:36	Driver					1	Download Images
104481	02-Jun-2022 20:01:27	Target Low Yield	87691	NLUF	NLUF-1Q22-02-0302 TDY-3Q22-PT17	1.0	131	Download Images
104480	02-Jun-2022 19:55:12	Target Low Yield	87691	NLUF	NLUF-1Q22-02-0302 TDY-3Q22-PT17		131	

Fig. 2 OMEGA Shot Images and Reports Webpage. Data can be slow and hard to find

PIs with LLE network access can directly access the database and file systems (Fig. 1(b)) instead of going through the web interface. This isn't available to external PIs. This process requires the user to have an account in the database or use a common database account. Both processes introduce security concerns. For a common database account, the password is shared among users, so it isn't known who is retrieving what data. This process is also cumbersome for the user as the PI must learn to write SQL scripts for their analysis. A PI with network access must use the SQL queries to first locate the files, and then must directly access the file on the file server. If desired, the PI can directly implement post processing into their analysis code.

It is also clear that many LLE PIs do similar post processing to images to get them ready for analysis. It seems unnecessary to have this post processing done on local machines a redundant number of times. It seems that that some post processing could be done on LLE servers prior to PI access. Specifically, many PIs subtract the background from images before their scripts perform more post processing.

3. Image Storage and Retrieval

Development was first focused on the best way to store and retrieve images and image data. One idea that was explored was storing HDF Images in an Oracle[3] database. Three ways were considered. The first way was storing them as BLOBs (binary large object files). In short, a BLOB just stores the binary in the database as it would be in a file system, but the file address can essentially be indexed relationally. Unfortunately, this doesn't allow for easy post processing within the database.

B-Files are another common way to store files in a database. These are essentially just links to files that are stored on a file server (the data for the file isn't stored in the table space). Although these can be indexed very fast, it was concluded that this file type wasn't the right fit

for the project since our goal was to do some post processing on images. A very similar ARCHIVE_FILES table space also already exists, which helps map shot numbers to file system locations. In the future these tables could be converted to use B-Files instead of just storing the file path as VARCHARs (variable-length character strings).

We also explored storing image data directly in the database. This involved storing image pixels in rows and columns in the database. We tested basic post processing of images stored in table space with SQL. Specifically, we tried background subtraction, which was easily achieved. This could also have been very easily added to a script through PL/SQL[3], which is built into the SQL developer software. The one downside of this method is that it wasn't fast compared to other methods. This is because data base tables are built on a key value relationship that is based on hash functions. A hash function[4] is a one-way and collision resistant function that makes accessing a value from a key fast. A hash function isn't needed when it is desired to access most of the table, which is what we want to do when accessing an image. So, overall, it is inefficient to use database tables to store and process images.

In all three of the above methods used to store and process images within a SQL database, a Python[5] data handler is still required. If fully implemented, a Python data handler script would be used to insert images into the database. When a user requests image data, the Python data handler then pulls data from the database. To originally populate this database, all the file paths of images would have to be pulled off the ARCHIVE_FILES table mentioned above, and all that data would have to be copied into the database using the specified method through the Python script. Similar scripts could also be written in JavaScript.

4. Image Postprocessing

Since the data handler script was written in Python it was an ideal place to also do post processing in Python. Whether a PI is interested in high level or low-level processing, Python is well supported in the scientific community. We started by converting images into Python arrays. It was found that this was slow since Python does a lot of type checking. We then discovered the NumPy[7] library. While Python is a high-level and interpreted language, NumPy bridges the gap between high-level programming and low-level performance, making it a powerful tool for numerical computations and array manipulations. NumPy is implemented in C, which is a fast low-level language. Images were converted to NumPy arrays for post processing. NumPy's fast array manipulation capability is ideal for image processing or transformation. For our basic background subtraction postprocessing we found NumPy to be four times faster than the SQL table processing that was mentioned in section 3.

We wanted to add the ability for PIs to pull image data in any format. After post processing was done, we implemented an on-the-fly image type converter in Python. The Python library Pillow[8] was used to allow data to be exported in various formats including PNG, JPEG, and TIFF. The h5py[9] Python library was used so that the image could also be returned in HDF5, the new version of the HDF file format.

5. Proposed Solution

Figure 3 provides an overview of the proposed process whereby users can access images from the data base and specify postprocessing that is to be performed before the image is returned to the user.

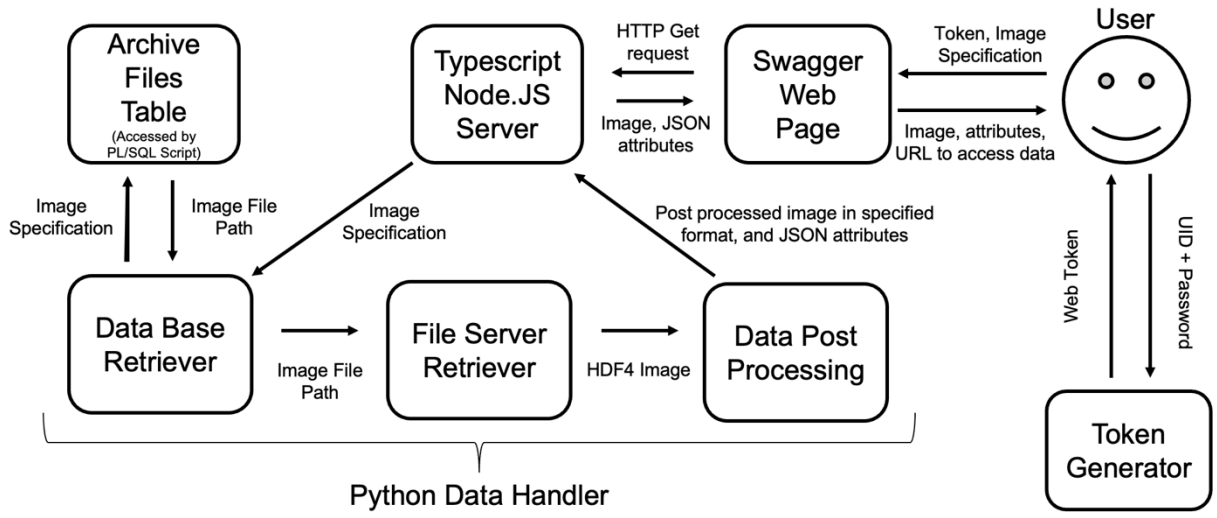

Fig. 3 The new proposed process for PIs to access and process image data. Note that Image Specification includes the diagnostic, shot number, post processing, and desired image format. Authentication is done with the web token within the Node.JS server.

.

LLE's RESTful (Representational State Transfer) API (application programming interface), which pre-existed to return operations data to PIs, was leveraged, to provide new routes for processed data. A RESTful API is an API that has numerous properties, the most important being that it is stateless, and has a uniform interface[10]. Stateless means that each request to a server is independent of other requests. This means that any request sent must contain all information needed for the server to return the required data. The user cannot count on the server saving information from past requests. Uniform interface means that meta data is sent and requested in a common format. This means that a RESTful API should have a unique URI (uniform resource identifier) for each resource. Generally, the client tells the server which resource it would like to identify through a URL (Uniform Resource Locator). To identify what the server needs to do with this resource, RESTful APIs typically implement HTTP (Hypertext Transfer Protocol). Common HTTP requests are GET, PUT, POST, and DELETE.

Node.JS[11] is an open-source, server-side JavaScript runtime environment that allows developers to run JavaScript code outside of a web browser. It enables the execution of JavaScript on the server, providing a powerful platform for building scalable, high-performance web applications and network services. We used Node.js with the Express[12] web application framework to build these routes. To test and browse the API we used the Swagger[13] API client. This gives users an efficient way to test and graphically view API endpoints.

When implementing new API routes we break the code down into two parts: the route and the controller. The same controller can be used multiple times if the same type of data is being used for multiple routes. In this case the controller would call the Python script from Typescript (Typescript is just a type enforced version of JavaScript which can be used with Node.JS), which would then go and retrieve the data, do whatever post processing was specified by the user, and then return the image for the user to view through Swagger. Swagger also provides a URL that PIs can embed into their code. The corresponding HDF attributes can be returned in JSON[14] (JavaScript Object Notation). This is a very easy format to work with as many programming languages easily support its manipulation. All the PI must do first is get an authenticated web token. This doesn't require them to be behind the LLE firewall. Fig. 3 shows how the user interacts with the Swagger page and how Swagger works with each part of the system.

There are many other opportunities for built-in image processing. Instead of one PI having to go to another to get their data or code, this processing could be implemented directly in Python. Scientists could get the image and data already processed through an API call by specifying what type of processing they would want done directly as a query.

It was realized that a pre-existing REST API used to return operations data could be leveraged to return processed data. We created HTTP GET routes for the processed data. A GET route is an API call that can return stateless information. This could greatly reduce the amount of processing that PIs do when they receive an image. Figure 4 shows how a user could access a sample diagnostic from a specific shot number. It can be also seen in the Request URL that users can specify the type of post processing; in this example background subtraction is shown with the route /api/image/get/subtracted.

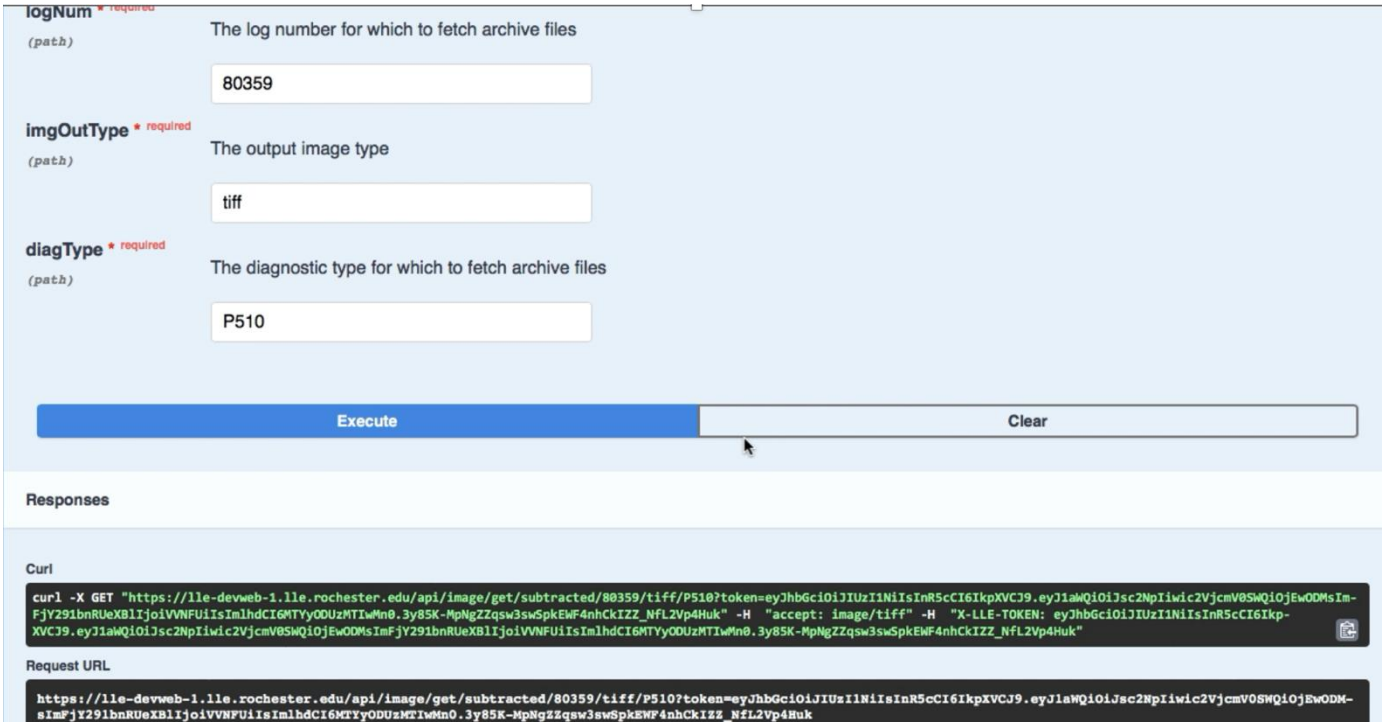

Fig 4. View of Swagger API client showing the interface for accessing P510 HDF images

6. Conclusion

This work focused on finding new ways to store, manipulate, and return image data for PIs. It was found that processing image data directly in a database is not an ideal option. The proposed solution of using a Python data handler that is called by a Typescript Node.js server seems to be the best option for user experience, ease of processing, and speed.

7. Acknowledgments

I would like to start off by thanking Dr. Craxton for organizing this amazing summer program. It has been an incredible opportunity for my academic growth. I would like to thank Ms. Trubeger for doing the behind-the-scenes administrative work and organizing all of our Zoom meetings. I would like to thank my advisor Mr. Kidder for the countless hours he spent on Zoom with me helping figure bugs out and helping guide me through the project. I also wouldn't have been able to do this without the help from the tremendous web and database team: Andy Zeller, Russ Edwards, Riley Adams, Barb Tate, and Tyler Coppenbarger. It was also great to compare with the other students in the program about what we have done.

8. References

1. https://supprt.hdfgroup.org/products/hdf4
2. https://supprt.hdfgroup.org/products/hdf5
3. https://docs.oracle.com/cd/B19306_01/server.102/b14220/intro.htm
4. https://www.oracle.com/database/technologies/appdev/plsql.html
5. https://csrc.nist.gov/glossary/term/hash_function
6. https://python.org
7. https://numpy.org

8. https://pillow.readthedocs.io/en/stable/

9. https://www.h5py.org

10. https://aws.amazon.com/what-is/restful-api

11. https://nodejs.org

12. https://expressjs.com

13. https://swagger.io

14. https://json.org

Exploration of Conduction and Stopping Power Models for Hybrid Fluid-Kinetic Simulations

LLE Summer High School Program

Aditya Srinivasan

Summer 2021

Advisors: Professor Adam Sefkow and Mike Lavell

Abstract

Radiation fluid-dynamic simulations use material models to describe the physical properties of a plasma for applications such as inertial confinement fusion. In contrast, a kinetic model can treat a wider variety of plasmas and does not need material models as long as particle collisions are treated correctly. The hybrid fluid-kinetic code TriForce uses both fluid and kinetic particles simultaneously and has collision algorithms in development to treat their interaction. The kinetic part of TriForce was used to calculate first-principles material properties such as electrical conductivity and stopping power. These calculations were used to verify the code against previous predictions by Perez et al. [Phys. Plasmas 19, 0831904 (2012)]. To calculate the conductivity of copper, an electric field was applied externally and caused the electrons to drift and conduct current. A Python code was written to calculate the conductivity based on the evolution of the electron velocity in the simulation. To calculate the stopping power, a mono-energetic beam of charged particles was launched onto a plasma at the desired density and temperature. The stopping power was then determined from the change in kinetic energy over time. Results presented in this work compare very well with analytic calculations for electrical conductivity and stopping power. This work demonstrates that the improved Monte Carlo collision algorithms in TriForce model elastic collisions well. Therefore, calculations like those presented here can be reliable inputs to TriForce (or any other fluid code) in the fluid regime. Alternately, electrical conductivity and stopping power can be calculated in-line when TriForce is used in the kinetic regime.

1 Introduction

Inertial Confinement Fusion (ICF) is a potential source of clean and unlimited energy. Since fusion involves materials with lower atomic numbers than nuclear fission, both the input fuel and the waste products are not (or much less) radioactive. This is a key difference from nuclear fission and makes fusion a very attractive source for energy.

Fusion energy requires very high temperatures and a typical simulation and experiment involves a range of densities, from a fraction of solid density to many times solid density. At these high temperatures the fusion fuel exists as a plasma, which is super heated matter existing as a combination of electrons, ions, and neutral atoms. Properties of these plasmas are important to model in order to predict conditions under which ICF can be an energy source.

Several attempts at proof-of-principle experiments are ongoing on large-scale facilities around the world such as the National Ignition Facility (NIF) [1] at the Lawrence Livermore National Laboratory and the OMEGA [2] laser at the University of Rochester. In ICF, a pellet containing a fuel made of isotopes of hydrogen – deuterium and tritium – is imploded using either lasers [3], [4], [5] or magnetic fields [6]. Shown below in Figure 1 is the example of laser direct drive [3], [5]. The pellet material, also known as the ablator, is typically made of polystyrene (a carbon and hydrogen plastic – shown in the pie chart on the bottom left of Figure 1). The laser irradiates the polystyrene (Figure 1 – top left), imploding the fuel (Figure 1 – middle), which compresses to high densities (Figure 1 - bottom right). The fuel is said to have ignited when the energy in the fusion reactions of the deuterium-tritium is greater than the laser energy used to irradiate the capsule. In indirect drive, being pursued on the NIF, the capsule is driven instead by x-rays that are emitted from a hohlraum (a cylindrical cavity) that is irradiated by the laser. The x-rays drive the capsule. Indirect drive [4] has achieved near-ignition in August of 2021 and experiments are ongoing to get closer to ignition. Direct-drive ignition has been predicted to be possible at the NIF but several uncertainties remain in these predictions and to date direct-drive ignition experiments have not been attempted.

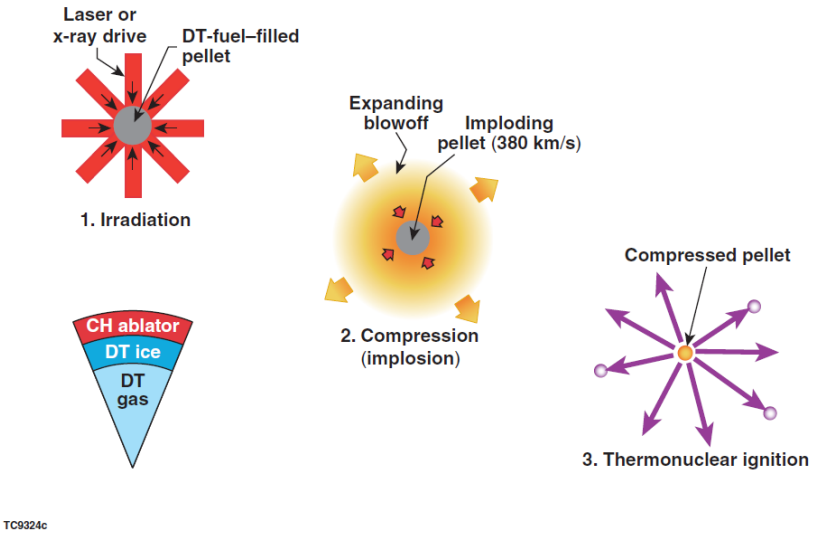

Figure 1: Schematic of laser direct drive. Step 1: A pellet made of polystyrene (CH) containing deuterium-tritium (DT) is irradiated by a laser. Step 2: The imploding pellet creates conditions suitable for fusion reactions of deuterium and tritium. Step 3: The hot, compressed core produces energy from fusion reactions. The process is similar for indirect drive, where the pellet is driven by x-rays rather than laser beams.

In this work the kinetic part of the TriForce [7] code (named TFLink) is used to calculate two transport properties of charged particles - electrical conductivity and stopping power. TriForce is a hybrid fluid-kinetic code that uses particle-based methods to calculate Coulomb collisions. Usually the plasma is approximated as a fluid and electrical properties are ignored in order to make implosion calculations more tractable. However, it is unclear as to whether this is a good approximation as such fluid codes do not reproduce experiments in all their details. In this paper, calculations are compared to previous numerical and analytic calculations from [8], with the primary goal of verifying the collision models in TriForce against this previous work.

The paper is organized as follows: in Section 2, the procedure for calculating the electrical conductivity and stopping power is described. Results are also described in the same section. Conclusions are presented in Section 3. Future work is described in Section 4.

2 Method and Results

2.1 Electrical Conductivity

The first part of this work involved determining the electrical conductivity of a copper plasma at a particular chosen density for a range of temperatures. Copper was chosen as calculations have been presented for this material in previous work [8]. The electrical conductivity was determined at one particular temperature using the steps as laid out in the flow chart in Figure 2. The same process was then employed to calculate the conductivity at other temperatures.

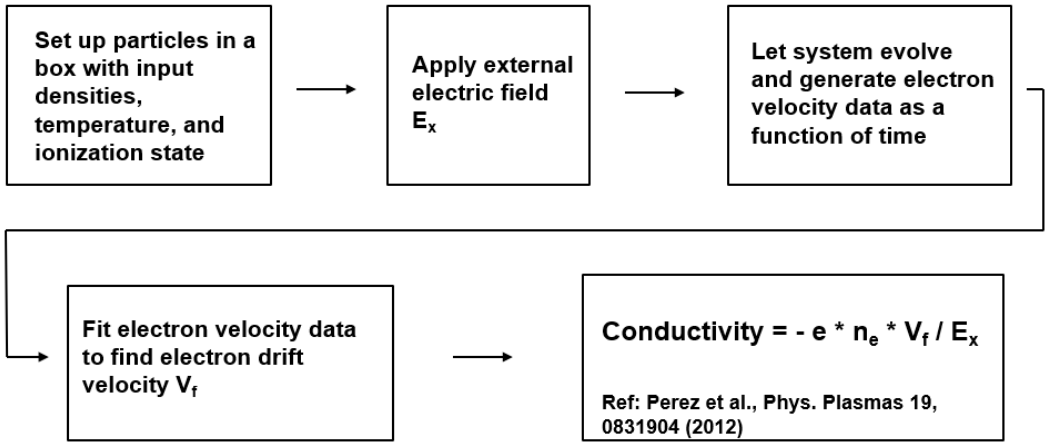

Figure 2: Process to determine the electrical conductivity using TriForce and known equations. e is the magnitude of the electron charge and n_e is the number of electrons per unit volume.

First, using the kinetic part of the TriForce code, a box of copper ions of size 1 cm $\times$ 1 cm $\times$ 1 cm with 40,000 particles was created at a particular temperature and density. This number of 40,000 was chosen to enable comparison with the calculations presented in [8], where the same number was chosen. Periodic boundary conditions were used for the box, meaning that if electrons exit one face of the box, they re-enter through the opposite face. A time step of $\Delta t = 2.5 \times 10^{-18} s$ is chosen for the problem. A self-consistent effective charge $< Z >$, calculated using an atomic model based on the Thomas-Fermi method, was also used [9]. The values used for the range of densities and temperatures are shown in Table 1 below.

n_i (1/cm^3)	kT (eV)	< Z >	n_e (1/cm^3)
8.49 x 10^{22}	1	4.6	3.90E+23
8.49 x 10^{22}	2	4.6	3.90E+23
8.49 x 10^{22}	5	4.6	3.90E+23
8.49 x 10^{22}	10	4.7	3.99E+23
8.49 x 10^{22}	20	5.2	4.42E+23
8.49 x 10^{22}	50	7.2	6.11E+23
8.49 x 10^{22}	100	9.8	8.32E+23
8.49 x 10^{22}	200	13.5	1.15E+24
8.49 x 10^{22}	500	19.8	1.68E+24
8.49 x 10^{22}	1000	24.1	2.05E+24

Table 1: Table showing the chosen ion density, n_i, the plasma temperature T (k is Boltzmann's constant), the calculated effective-charge values for a copper plasma $< Z >$, and the electron density defined by $n_e =< Z > n_i$.

Next, after setting up the particles in the box, an external electric field E_X of 3×10^{10} V/m was applied. (The value of this field is used in [8].) Third, this system was allowed to evolve naturally including the effect of electron-electron and electron-ion collisions. The electrons initially accelerate. Then collisions alter the evolution of the electron velocities until an equilibrium value is reached. The average electron velocity was recorded as a function of time. Figure 3 shows the average velocity versus time for 50 eV, 200 eV, and 500 eV initial temperatures. The electron velocities show the expected behavior of particles not in equilibrium, with an initial acceleration followed by a saturation due to the balance of Coulomb scattering and acceleration. Using these curves, it is possible to determine the final drift velocity, which is equal to the asymptotic average electron velocity at equilibrium.

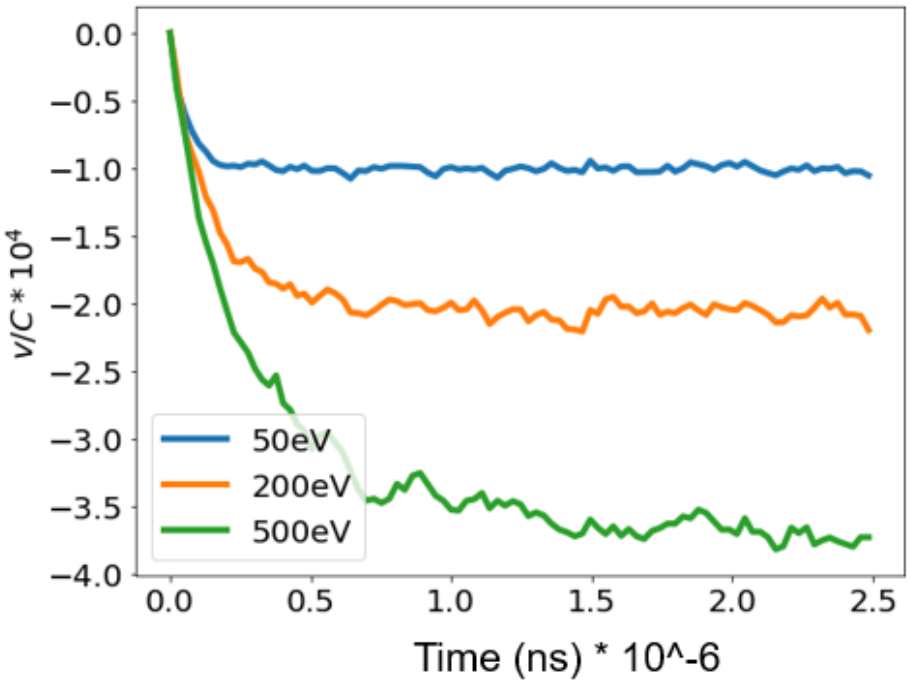

Figure 3: The ratio of the electron drift velocity, v to the speed of light, c, for 50 eV, 200 eV, and 500 eV plasmas when an electric field of 3×10^{10} V/m is applied.

To quantify the electron drift velocity, the average velocity evolution is fit to a previously identified (equation 24 in Ref. [8]) functional form for each temperature and is given by,

$$V(t) = At + V_f(1 - e^{(-t/\tau)}) \tag{1}$$

where A, V_f, and τ are fitting parameters and t is the simulation time, and V_f is the final (asymptotic) electron drift velocity. Note that this equation is valid only within the simulation time up to 2.5×10^{-15} s. Extrapolating this function to $t \to \infty$ does not have any physical meaning as it diverges.

As an example of the fitting, this functional form compared with the calculations is shown for a 200 eV temperature in Figure 4. In this figure the dimensionless ratio of the electron velocity to the light speed is shown as a function of the dimensionless time $t/\Delta t$, where Δt, the time-step is previously defined as $2.5 \times 10^{-18} s$. An excellent

fit is obtained with this functional form ($R^2 = 0.979$). Note that an asymptotic value of $v_f \sim 2 \times 10^{-4} c$ is obtained for this temperature.

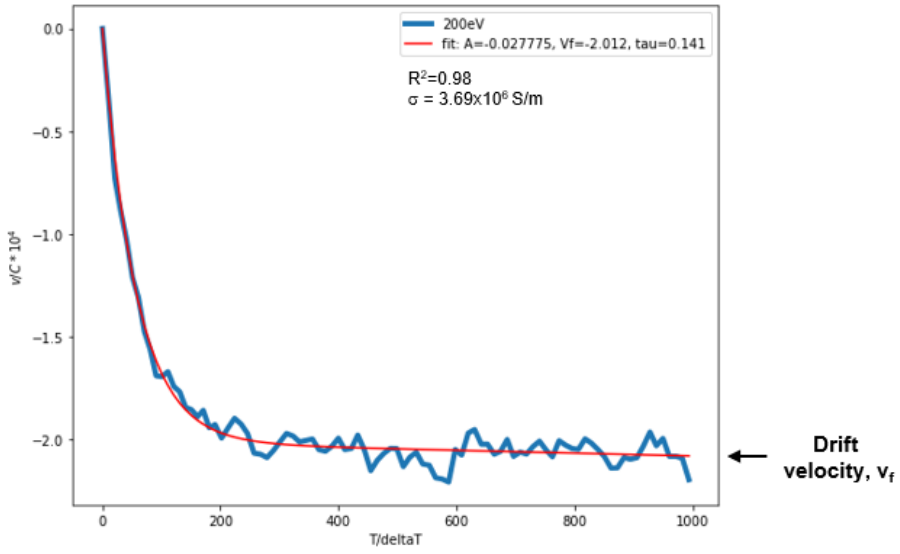

Figure 4: Ratio of the drift velocity to the speed of light for 200 eV compared to the fitting functional form given by Equation 1. The x-axis is plotted in terms of the dimensionless time, the ratio of the simulation time to the time-step in the calculation.

With this value of the drift velocity, the electrical conductivity for each temperature is given by:

$$\sigma = -e * n_e * V_f / E_x \tag{2}$$

where e represents the charge of an electron and n_e represents the number density of electrons given in Table 1.

These calculations are repeated for a range of temperatures: 1, 2, 5, 10, 20, 50, 100, 200, 500, and 1000 eV. The calculated electrical conductivity is shown in Figure 5. The blue curve shows the calculations using TriForce. In orange are the calculations using the analytic expression given by Equation 26 from Ref.[8], which is shown below:

$$\sigma = \frac{8\pi\epsilon_0 c}{r_e}\left[\frac{2 < Z >}{3\pi\bar{l}^2\sqrt{\overline{T_e}}}[1-(1+a)e^{-a}] + \frac{\overline{T}_e^{3/2}}{< Z > ln\Lambda}(1+a+\frac{a^2}{2}+\frac{a^3}{6})e^{-a}\right] \tag{3}$$

where r_e is the classical electron radius defined as $r_e = e^2/4\pi\epsilon_0 m_e c^2$, ϵ_0 is the vacuum permittivity, m_e is the electron mass, $\overline{T}_e = 2kT_e/(\pi m_e c^2)$ is the normalized temperature, $\bar{l} = (n_i r_e^3 \sqrt{3/4\pi})^{-1/3}$ is the dimensionless interatomic distance or the interatomic distance in units of r_e, $< Z >$ is the calculated effective charge, and a is the dimensionless parameter given by $a = 2 < Z > (ln\Lambda/\pi)^{1/2}/(\bar{l}\overline{T}_e)$. The Coulomb logarithm $ln\Lambda$ is given by Eq. 22 and Eq. 23 in Perez et al.

A comparison of Equation 3 and Figure 5 shows that with increasing temperatures, the conductivity is dominated by the second term in Equation 3 (the Spitzer term), which scales as $\overline{T}_e^{3/2}$. At lower temperatures, the first term, which scales as $1/\sqrt{\overline{T}_e}$, dominates the electrical conductivity.

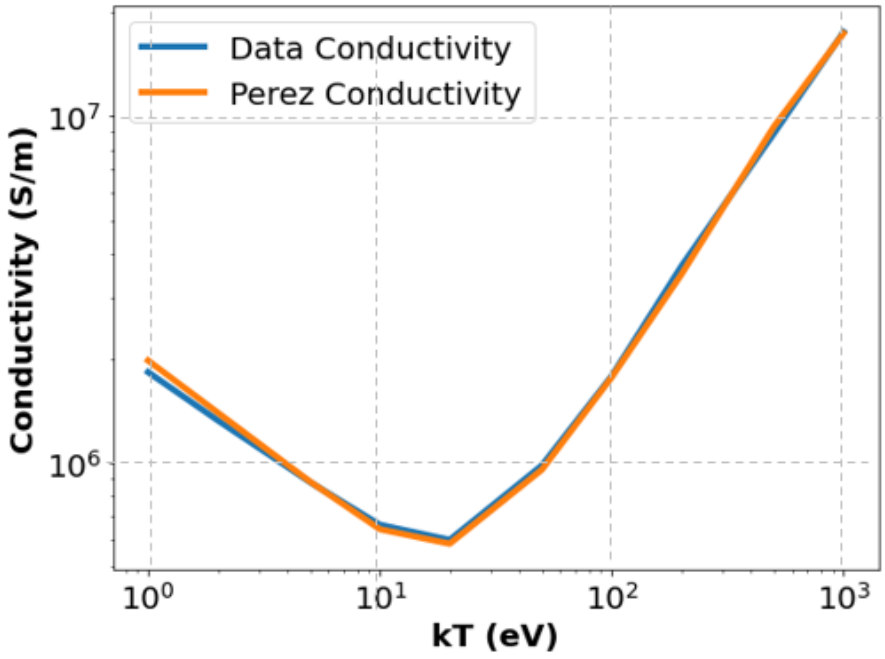

Figure 5: The calculated conductivity using TriForce (Equation 3) compared with calculations using Equation 26 in Perez et al. [8]. The similar nature of the curves indicates that TriForce's conductivity predictions are accurate.

The excellent comparison indicates that TriForce accurately calculates Coulomb collisions. These conductivity calculations can now be extended to any material under any conditions. Furthermore, it also shows that TriForce can be accurately used to

model fluid-like conditions where electrical conductivity can be an input parameter calculated from previous kinetic calculations.

2.2 Stopping power

The stopping power of a particle, defined by the change in energy of a particle per unit length, is another important transport property of charged particles in a plasma. The initial setup of the stopping power calculation was similar to the setup for the conductivity measurement. The flowchart in Figure 6 describes the steps used to calculate the stopping power.

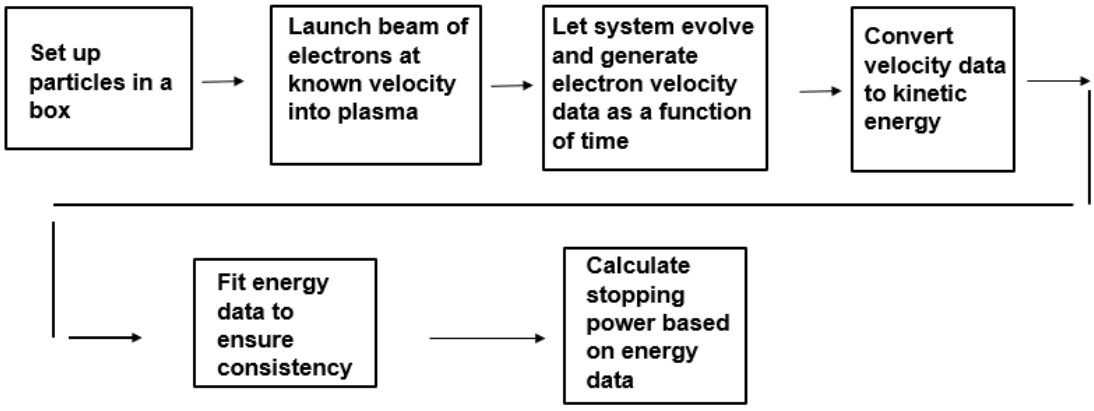

Figure 6: Process to determine the stopping power using TriForce.

Mono-energetic probe electron beams between 100 keV and 1 MeV were launched into a cold singly-ionized solid density hydrogen plasma. The cold ion plasma temperature was chosen to be 1 Kelvin so that the electron beam energies were significantly larger than the thermal plasma energy. The plasma was selected to be composed of artificially light ions (with ion mass $m_i = 5m_e$) for comparison with the plasma simulations in [8] and for easier computation.

From here, the system was allowed to evolve from its non-equilibrium state through collisions and the average beam electron velocity was recorded at each time step. Next, the velocity data was converted to kinetic energy data. Note that the standard kinetic energy velocity relationship cannot be used here since the electron beam particles move

at relativistic speeds. The relativistic momentum, p is obtained from the velocity as

$$p = \frac{m_e v}{\sqrt{1 - \frac{v^2}{c^2}}} \tag{4}$$

which is then converted to the relativistic kinetic energy as

$$E_{KE} = \sqrt{m_e^2 c^4 + p^2 c^2} - m_e c^2 \tag{5}$$

Kinetic energy curves as a function of the dimensionless ratio t/τ, where $\tau = \frac{4\pi\epsilon_0^2 m_e m_i c^3}{q_e^2 q_i^2 n_i ln\Lambda}$, are shown in Figures 7 and 8 for 1 MeV and 100 keV, respectively. q_i is the charge of the ion and q_e is the charge of the electron. Each orange line is the calculated kinetic energy as a function of time.

The analytic evolution of the beam momentum is given by Equation 27 in Perez and is given below:

$$\arctan(p') - p' - \arctan(p'_0) + p'_0 = \frac{t}{\tau} \tag{6}$$

where p' is the dimensionless mean beam momentum given by $p/m_e c = v/c\sqrt{1 - \frac{v^2}{c^2}}$ with mass = 1, p_0 is the dimensionless initial momentum, and $\tau = \frac{4\pi\epsilon_0^2 m_e m_i c^3}{q_e^2 q_i^2 n_i ln\Lambda}$. Equation 5 is used to convert the momentum to kinetic energy. These analytic curves are also shown in Figures 7 and 8.

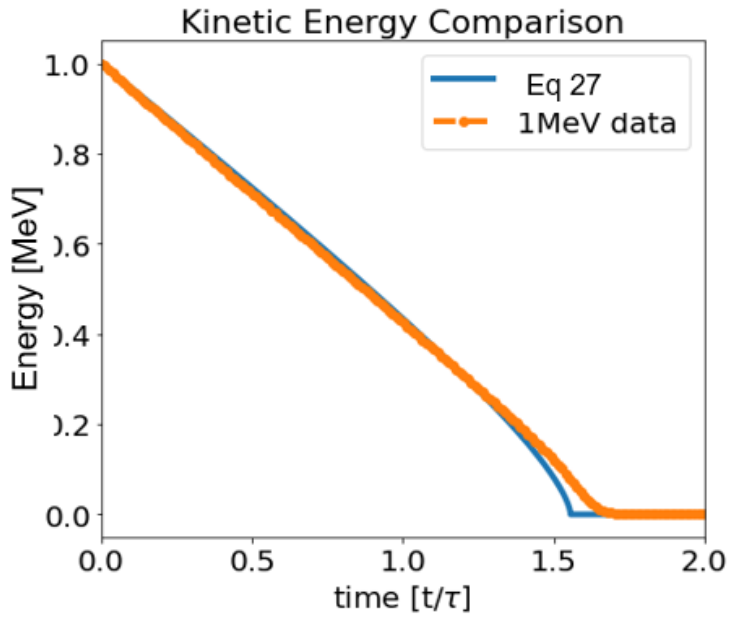

Figure 7: Calculated kinetic energy (Equation 6) from a 1 MeV beam (orange line) compared to Equation 27 in Perez (blue line) for a plasma with artificially light ions. The good comparison shows that TriForce can accurately calculate kinetic energy data.

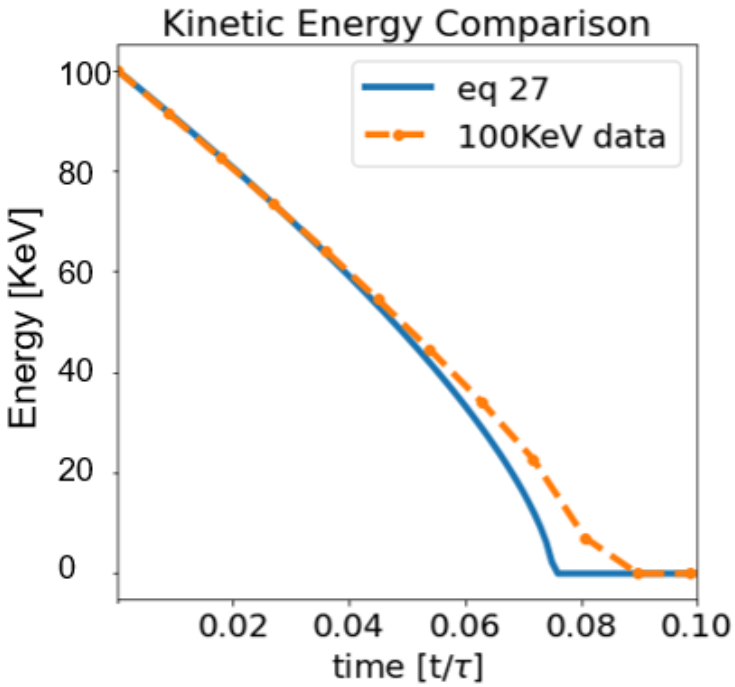

Figure 8: Calculated kinetic energy from a 100 keV beam (orange-dash line) compared to Equation 27 in Perez (blue line) for a plasma with artificially light ions. The good comparison again shows that TriForce can accurately calculate kinetic energy data.

Each blue line in the figures above is given by the conversion of the analytic equation in Equation 6 to kinetic energy using Equation 5. The similarities between the analytic and calculated kinetic energy evolution curves shows that TriForce's kinetic energy calculations reproduce the analytic formula in Equation 6, validating the electron-ion collision scheme in the code. The theory and numerical solutions diverge when the beam energy is nearly depleted because the theory solution assumes immobile ions.

Next, a more realistic and self-consistent aluminium plasma is initialized in TriForce. Probe electron beams of energies varying from 10 keV to 4 MeV are launched into this plasma in a series of calculations. Similar kinetic energy evolution (as the calculations outlined previously) is calculated as a function of time. The results for the kinetic energy evolution are summarized in Figure 9.

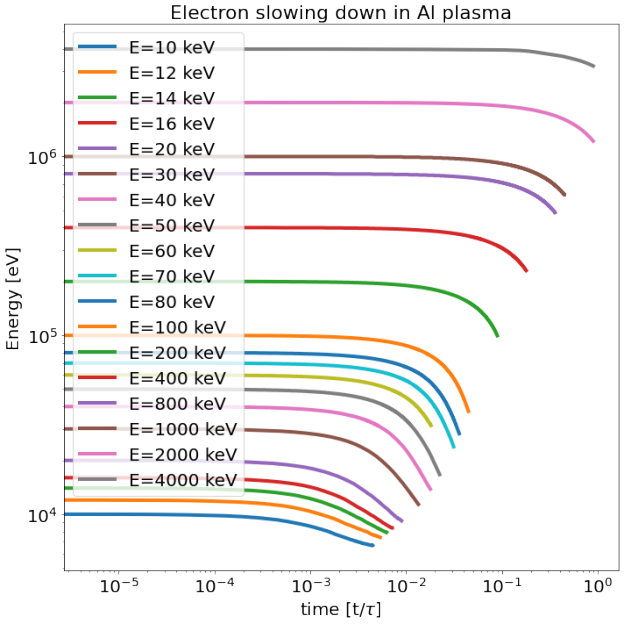

Figure 9: Kinetic energy evolution for a cold aluminum plasma for various beam energies. Note that the labels for each of the curves are listed in the opposite order, i.e., the 10 keV curve is labeled at the top but is the lowest curve in the figure.

From each of these kinetic energy curves, the stopping power (Q) can be obtained from:

$$Q = \frac{1}{v_0}\left(\frac{dE}{dt}\right)_{t=0} \tag{7}$$

where v_0 is the initial beam velocity and $(\frac{dE}{dt})_{|t=0}$ is the initial slope of the kinetic energy curve. Shown in Figure 10 is the stopping power normalized to the product of mass density in the plasma and the Coulomb logarithm (defined in Equation 23 in [8]) versus the electron energy.

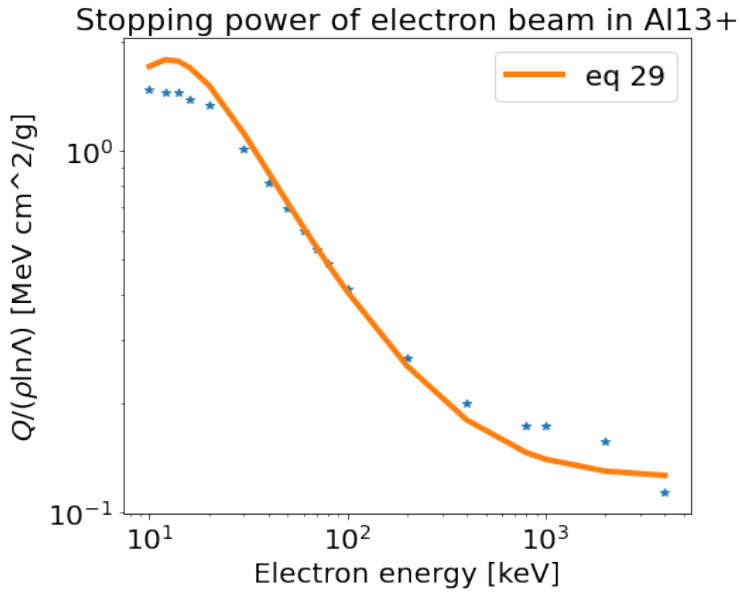

Figure 10: Stopping power calculated in TriForce (blue asterisk) compared to Equation 29 in Perez [8].

Again, there is a good agreement with the analytic expression in Perez et al., validating the collision model used in TriForce for electron-ion collisions. The differences between the analytic model and the calculations are likely due to errors in taking the numerical derivative, $(\frac{dE}{dt})_{|t=0}$ from the data in Figure 9.

3 Conclusions

Electrical conductivity and electron stopping power are important properties of laser generated plasmas and are critical for modeling current and heat flow. The kinetic part of the hybrid fluid-kinetic code TriForce has been used to simulate these properties from first principles. Electrical conductivity in copper has been calculated and

compared with previous analytic work for a range of plasma conditions. The calculated conductivity values compare very well against analytic calculations. Electron stopping power has been tested for electron-ion collisions and it compares favorably with previous calculations. These proof-of-principle calculations indicate that TriForce can be used to predict these microscopic properties for any material, whether in or out of equilibrium. The stopping power was then calculated for an electron beam in aluminum. The calculations using TriForce compare very well with the previously known analytic formula, again indicating that TriForce can be used to model kinetic properties of plasmas very well.

4 Future Work

Future work involves the calculation of conductivity and stopping power for materials of relevance to inertial confinement fusion such as plastic, deuterium, and tritium. These calculations can also be used as inputs for fluid simulations of plasmas. Since this work also indicates that non-equilibrium, non-fluid regimes can be treated accurately with a kinetic model, the particle-in-cell part of TriForce can be used to study kinetic effects in inertial confinement fusion plasmas.

5 Acknowledgements

Thank you to my advisors Mike Lavell and Prof. Sefkow for offering me this project and the huge learning opportunity, not to mention the marathon zoom sessions to help me out as we went along. A huge thank you to Dr. John Shaw for all the help with the code development. Thanks to Dr. Craxton for organizing the program and giving us the opportunity to experience research despite the challenges posed by COVID. Thank you also to Ms. Truebger for coordinating all of our meetings and the Friday Seminars. A huge thank you to all those that made the remote program happen in IT, HPC, and Administration. Lastly, thanks to the other students in the 2021 LLE HS program;

interacting and getting to know them made the program especially enjoyable.

References

[1] E. M. Campbell and W. J. Hogan, "The National Ignition Facility - applications for inertial fusion energy and high-energy-density science", Plasma Phys. Control. Fusion 41, B39 (1999).

[2] T. R. Boehly et al., "Initial performance results of the OMEGA laser system", Opt. Commun. 133, 495 (1997).

[3] J. Nuckolls, L. Wood, A. Thiessen, and G. Zimmerman, "Laser compression of matter to super-high densities: Thermonuclear (CTR) applications," Nature 239, 139 (1972).

[4] J. D. Lindl, "Development of the indirect-drive approachto inertial confinement fusion and the target physics basis for ignition and gain," Phys. Plasmas 2, 3933 (1995).

[5] R. S. Craxton et al., "Direct-drive inertial confinement fusion: A review", Physics of Plasmas 22, 110501 (2015).

[6] S. A. Slutz et al., "Pulsed-power-driven cylindrical liner implosions of laser preheated fuel magnetized with an axial field", Physics of Plasmas 17, 056303 (2010).

[7] A. Sefkow et al., "Introduction to TriForce: A Multiphysics Code for Hybrid Fluid Kinetic Simulations," Bull. Am. Phys. Soc. 64 (2019).

[8] F. Perez et al., "Improved modeling of relativistic collisions and collisional ionization in particle-in-cell codes", Phys. Plasmas 19, 0831904 (2012).

[9] Private communication with S. X. Hu

Computational Modeling of the Polarizability of Liquid Crystals

Andrew Wu

Pittsford Mendon High School

Project Advisor: Mr. Kenneth Marshall

Laboratory for Laser Energetics
University of Rochester

June 2023

Abstract

Using the molecular modeling packages *Maestro and NWChem,* several liquid crystals (LCs) commonly used in laser systems were modeled using Density Functional Theory (DFT) to determine their dielectric anisotropy (Δε) values computationally. The difference in polarizability (Δα) between the parallel and perpendicular axes of an LC molecule was calculated by DFT and used as input to calculate Δε for each compound. The calculated Δε values were compared to existing experimental data for two materials to determine the validity of the model. The calculated values from the Maier-Meier equation and the experimental values from the literature for the LC materials PCH5 and 5CB agreed to 8% and 29%, respectively, with the best agreement between calculated and experimental values obtained for the material with smaller molecular polarizability. This model can be used for future design efforts to develop LC materials with large Δε, fast response, and high laser damage resistance for current and future applications in OMEGA, OMEGA EP and other laser systems.

1. Introduction

A liquid crystal (LC) is a substance that exhibits properties of both solid crystals and liquids. The molecules in a LC are more organized than those in liquids but are not rigidly ordered like those in solids. LCs are characterized by the order parameter (S), which measures the degree of organization between molecules. The value of S ranges from 0 for an isotropic liquid to 1 for a solid crystal and generally decreases as the temperature increases (Fig. 1). Most LC molecules have a long, parallel axis and a short, perpendicular axis. The general direction that the long axes of the LC molecules follow is called the director (*n*). The greater the deviation of individual LC molecules from the director, the smaller the value of S will be.

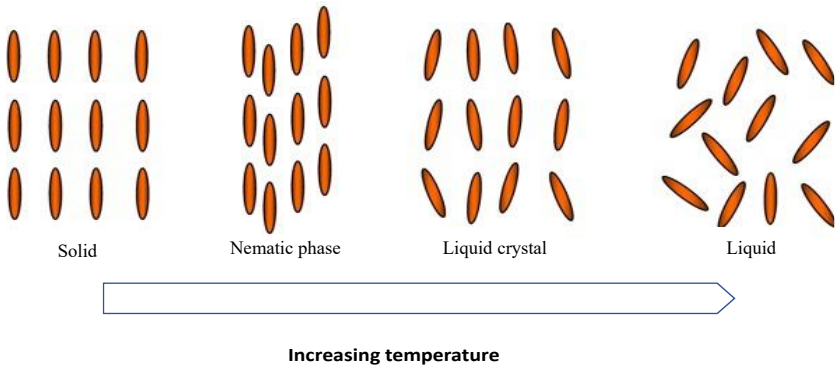

Fig 1: Comparison of the ordering in liquid crystals as a function of temperature.

LC's also exhibit various phases, each with their own molecular packing and orientation variations that affect their physical properties. For the nematic phase, the value of S ranges typically between 0.5 and 0.8. Nematic phase LC molecules are arranged in relatively random positions with their long molecular axes facing a similar direction. This unique behavior allows nematic LCs to exhibit anisotropy in their physical and optical properties. Optical anisotropy, or birefringence (Δn) is defined as the difference between the refractive index when the electric field is parallel (n_e) and perpendicular (n_o) to the molecular axis (Equation 1) while dielectric anisotropy ($\Delta\varepsilon$) is defined as the difference in electric field permittivity (how much the electron distribution is affected when an electric field is applied) when the electric field is either parallel ($\varepsilon_\parallel$) or perpendicular ($\varepsilon_\perp$) to the long molecular axis (Equation 2).

$$\Delta n = n_e - n_o \qquad (1)$$

$$\Delta\varepsilon = \varepsilon_\parallel - \varepsilon_\perp \qquad (2)$$

Birefringence and dielectric anisotropy are both related to the degree of electron density delocalization and polarizability (how easily the electrons of a material are affected by an electric field) of the LC molecular structure. In general, the larger the degree of electron delocalization

and polarizability, the larger the values of both Δn and Δε will be. *Unsaturated* LC materials [containing carbon ring structures with alternating single (σ) and double (π) bonds, shown in Fig. 2(a)], will be highly polarizable due to their high degree of electron delocalization, and as a result will exhibit both high Δn and Δε. Ideally, this class of LC material would be preferred for both passive and electrically driven applications in high power lasers due to the smaller path length requirements and faster response times, but the large electron delocalization due to the overlapping π-bonds also results in significantly reduced laser damage thresholds [1].

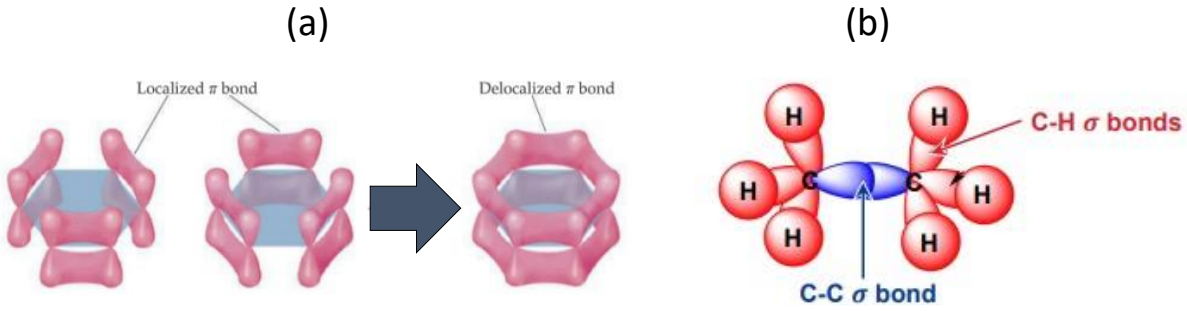

Fig. 2: (a) Delocalized electron distribution in an unsaturated material; (b) saturated materials are composed primarily or exclusively of σ-bonded atoms.

Saturated LC materials [those that are composed primarily of σ–bonded atoms, as diagrammed in Fig. 2(b)] show significantly higher laser damage thresholds, but both the resultant Δn and Δε values will be smaller, as both are intrinsically linked to the degree of molecular electron delocalization and polarizability. Consequently, thicker path lengths and higher drive voltages will be required for existing LC devices to meet present and future requirements for passive or electrically driven applications in high power laser systems. Using computational chemistry design tools, an analysis of the effect of molecular structure on the polarizability of unsaturated or fully saturated LC materials was undertaken as the first step in designing materials that combine fast electro-optical switching potential with high laser damage resistance for high power laser applications.

2. Materials and Computational Methods

Modeling of the Δε of LC materials was accomplished using two computational chemistry modeling packages to generate the physical properties of the materials based on molecular structure. Two-dimensional molecular structures were drawn using *Maestro*, a software module of Schrodinger's *Material Science Suite* [2,3], using its 2D ligand interaction function.

Maestro's molecular mechanics energy optimization routine was then applied to the structure to ensure that each atom was in its lowest energy conformation. The energy-minimized structures were then exported into the open source molecular modeling program *NWChem* [4] for computation of polarizability, dipole offset (displacement of the separation between charges in a molecule away from the center of the molecule), and density using Density Functional Theory (DFT). For these computations the basis set 6-311++G** was used, as it was determined to be the best fit to these types of calculations based on the existing literature. One-hundred iterations were used for each simulation, with a total runtime for each calculation of ~1 hour on a Linux based supercomputing cluster with a total computational capacity of 7000 Xeon x86 CPUs and 200 TB of memory.

Figure 3 shows the molecular structures of the two LC molecules modeled in this study [4–cyano– 4'–pentylbiphenyl (5CB) and 4–*trans*–4–pentylcyclohexylbenzonitrile (PCH5)]. Both molecules are structurally similar in that they contain the same terminal functional groups (cyano and n-pentyl alkyl) and the molecular core is composed of two connected six-membered carbon rings, but for 5CB both rings are unsaturated (contain electron-rich π-bonds that are highly polarizable), whereas in PCH5 only one of the six-membered rings is fully saturated (contains only σ-bonds). The molecular polarizability is related to both the Δε and the

birefringence (Δn), and thus the large polarizatility should also lead to a larger value of Δε for 5CB. Concomitantly, the higher polarizability of 5CB reduces its resistance to laser damage [1].

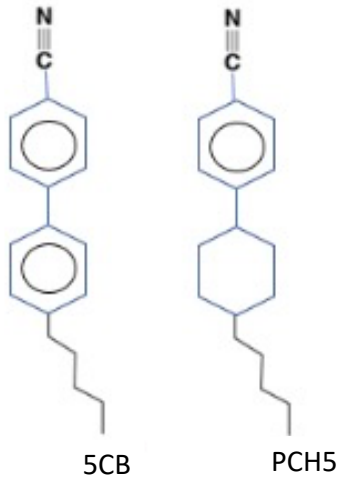

Fig. 3: Molecular structures of unsaturated (5CB) and partially saturated (PCH5) LC materials modeled in this study.

The molecular polarizability output from NWChem calculated using DFT was used as input to the Maier-Meier equation (Equation 3) [5,6] to calculate the Δε for each LC material:

$$\Delta\varepsilon = \frac{NFh}{\varepsilon_0}\left[\Delta\alpha - F\frac{\mu^2}{2kT}\left(1 - 3\cos^2\beta\right)\right]S \qquad (3)$$

where Δε is the dielectric anisotropy, N is the number of molecules per unit of density, h and F are the internal cavity field and reaction field factors for aspherical polarization, respectively, ε_o is the permittivity of free space, Δα is the difference in polarizability between the long and short axes of the molecule (i.e., the polarization anisotropy), μ is the magnitude of the dipole moment, k is the Boltzmann constant, T is the temperature in degrees Kelvin, β is the angle between the dipole moment and the director (n), and S is the order parameter. For this series of calculations, the temperature was set to 293° K, S was 0.8 (a typical value for a nematic LC at room

temperature), and μ was 5.95 Debye [7]**.** All calculations were conducted on a single molecule in the gas phase for simplicity to avoid the complexities and computational intensity required to take into account associative effects from neighboring molecules that occur in the condensed phase.

3. Results

Figure 4 compares the values of Δε for 5CB and PCH5 calculated from the Maier-Meier equation with experimental data for these two materials from the literature [8]. The agreement between calculated and experimental values of Δε was within 8% (PCH5) and 29% (5CB). The better agreement was for the material with smaller molecular polarizability (PCH5).

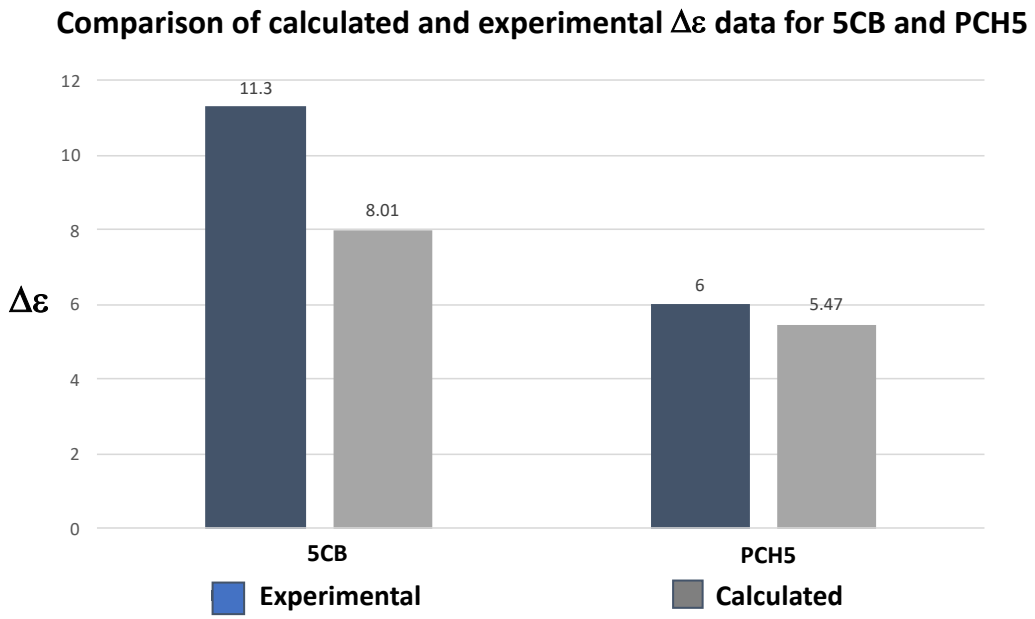

Fig. 4: Calculated and experimental values for Δε for the LC materials 5CB and PCH5. Better agreement between calculated and experimental values was observed for PCH5.

Maier-Meier calculations of this nature are susceptible to a range of errors that can be as large as 200% [9]. There are a number of factors that are responsible for these large deviations from experimental values. Because these calculations were performed on the basis of a single isolated molecule in the gas phase for simplicity, physical interactions between LC molecules in

the condensed phase (e.g., Van der Waal's forces and other electrostatic forces) that could have an effect on the molecular polarizability and Δε were neglected. Complex molecular dynamics calculations would have been required to account for these interactions, which was clearly beyond the scope and time frame of this project. The parameter assumptions for the values of S and T and the particular DFT basis set employed in the calculations (6-311++G**) all have an impact on the calculated value of Δε**.** Future efforts should incorporate more accurate values for assumed parameters, other DFT basis sets, and molecular dynamics simulations to improve accuracy.

4. Conclusions

Overall, the calculated Δε for the LC materials 5CB and PCH5 are in relatively good agreement with previous experimentally determined values, which implies that DFT modeling using *NWChem* and the Maier-Meier equation is valid for qualitative estimation of the molecular polarizability of LC molecules whose molecular structures are similar and differ only by the number and distribution of π-bonds throughout the molecule. Although the model at this point is qualitative, incorporation of more advanced computational methods such as molecular dynamics simulations will allow more accurate prediction of Δε and other physical properties of LCs important for device applications in high-peak-power laser systems.

5. Acknowledgements

I thank the Laboratory for Laser Energetics and the United States Department of Energy for providing the funding and opportunity for me to conduct this research. I also thank my advisor, Mr. Kenneth L. Marshall for introducing me to and guiding me through this project, as well as Dr. William Scullin, and UR undergraduate students Baris Eser Ugur and Faraan Hamad for

assisting me throughout this project. Finally, I recognize Dr. R. Stephen Craxton and Ms. Kimberly Truebger for setting up and administering the program, respectively.

6. References

1. T.Z. Kosc *et al.*. *Sci. Rep. 9*, 16435 (2019).

2. Schrodinger, Inc, 1540 Broadway, 24th Floor, New York, NY 10036

3. M. Valiev *et al*., *Comput. Phys. Commun*. 181, 1477 (2010)

4. A. D. Bochevarov *et al*., *Int. J. Quantum Chem*. 113, 2110 (2013).

5. W. Maier and G. Meier, *Z. Naturforsch*. 16a, 262, 470 (1961).

6. J Xu, *et al, Jpn. J. Appl. Phys.* Vol. 40, (2001), pp. 1375-1376

7. D. Sharma, G. Tiwari, and S. N. Tiwari, Pramana – *J. Phys*. 95, 71 (2021)

8. *Optics of Liquid Crystal Displays,* Second Edition, by Pochi Yeh and Claire Gu (Page 23) Copyright 2010 John Wiley & Sons, Inc.

9. A. Di Matteo and A. Ferrarini, *J. Chem. Phys* 117 (5), 2397-2414 (2002)